Imperial College London
Department of Earth Science and Engineering

Advanced Numerical Methods for Mantle Convection Models

Stephanus Cornelis Kramer

Supervised by:
Prof. Matthew D. Piggott
Prof. D. Rhodri Davies

Submitted for the degree of Doctor of Philosophy (PhD)

March 2023

Statement of Originality

I declare that this thesis is my own work except where otherwise stated and referenced.

Stephanus Cornelis Kramer

1 March 2023

Copyright Statement

The copyright of this thesis rests with the author. Unless otherwise indicated, its contents are licensed under a Creative Commons Attribution-Non Commercial 4.0 International Licence (CC BY-NC). Under this licence, you may copy and redistribute the material in any medium or format. You may also create and distribute modified versions of the work. This is on the condition that: you credit the author and do not use it, or any derivative works, for a commercial purpose. When reusing or sharing this work, ensure you make the licence terms clear to others by naming the licence and linking to the licence text. Where a work has been adapted, you should indicate that the work has been changed and describe those changes. Please seek permission from the copyright holder for uses of this work that are not included in this licence or permitted under UK Copyright Law.

The text in sections 2.1 to 2.5 in chapter two is adapted from S. C. Kramer et al. (2012). "An implicit free-surface algorithm for geodynamical simulations". In: *Phys. Earth Planet. Int.* 194, pp. 25–37. DOI: 10.1016/j.pepi.2012.01.001 which is under copyright Elsevier 2012, as are all figures in chapter two. Permission for reproduction in this thesis is based on Elsevier's author rights [1] which allow inclusion in a thesis or dissertation provided this is not published commercially.

The text and figures of chapter three are based on S. C. Kramer et al. (2021). "Analytical solutions for mantle flow in cylindrical and spherical shells". In: *Geoscientific Model Development* 14.4, pp. 1899–1919. DOI: 10.5194/gmd-14-1899-2021, copyright the authors 2021, which has been distributed under the Creative Commons Attribution 4.0 License.

[1] https://www.elsevier.com/about/policies/copyright

Figure 4.1 has previously appeared as Figure 1 in D. R. Davies et al. (2011). "Fluidity: a fully unstructured anisotropic adaptive mesh computational modeling framework for geodynamics". In: *Geochem. Geophys. Geosys.* 120, Q06001. DOI: 10.1029/2011GC003551, Copyright 2011 by the American Geophysical Union. Permission has been obtained for reproduction in this thesis.

Dedication:

Dedicated to my Dad, Cees Kramer (1944-2019),
who I know would have loved to see the end result.

Acknowledgements

First of all, I would like to express my deepest gratitude to Rhodri Davies and Cian Wilson, without whom I would have never started this endeavour into the realm of mantle convection modelling. As "Team Stokes", they have guided me at every step on this journey, and have made it, despite the inevitable frustations, a fun and rewarding experience. In particular, they have both been essential in almost every aspect of the research presented in this thesis. Rhodri's clear vision on how advances in numerical methods can help to answer relevant scientific questions, and his natural ability to bring out the best in people he works with, have been instrumental in developing my carreer in this area. Cian's disposition to try to gain a deep understanding of a problem, his patience and meticulousness have been a source of aspiration, and a yardstick for me for what is good and sound research. I would also like to thank Matthew Piggott who has encouraged and provided me the opportunity to write this thesis whilst being employed as a researcher at Imperial. More generally, he has been immensily supportive throughout my wider academic career, and has always known how to play to my strengths and succesfully engage me in his research programme, as well as helping me to develop my own. Someone who has also been crucial at a number of key points in my academic carreer is David Ham. From introducing me to the fundamentals of scientific programming, recommending me to various people in the field, to encouraging me to finally get this bloody thesis done. I believe his work, leading the development of the Firedrake finite element framework, will be transformational for my further research and many others. I would also like to express my appreciation to my examiners, professor Huw Davies and professor Saskia Goes for the stimulating conversation during my viva, and their thorough reading of this thesis. I would further like to mention a number of other people that I have worked with in the context of the development of Fluidity that have inspired me and that I have learnt a lot from: Patrick Farrell, Colin Cotter, Jemma Shipton and Adam Candy. I'm very grateful for the Department of Earth Science and Engineering for sponsoring me as a PhD Student alongside my normal job. I'm also very thankful for the many brilliant PhD students I have worked with within the department over the years. For the social aspect, keeping me sane, and trying but failing to get me interested in cricket or Star

Wars, I thank Gareth Collins, Rhodri Nelson, James Percival, Francois van Schalkwyk, and Tom Davison. On the topic of leisure and well being, I would also like to give a big shout-out to all the lovely people from Imperial College choir. Finally, I am very grateful for the love and support from my Mum, and my brother and his family.

Abstract

Numerical modelling of Earth's mantle is a complex, and computationally demanding task due to, amongst others, the broad spectrum of temporal and spatial scales playing a role in mantle flow, large uncertainties in the physical properties of mantle material, with large and localised transitions in viscosity and density. This thesis introduces and analyses a number of numerical techniques that may bring a significant contribution in meeting some of these challenges. Firstly, we introduce a novel time integration scheme for free surface movement in mantle convection models that is more accurate and stable for large time steps. Secondly, we extend the capabilities of anisotropic mesh optimisation, which allows efficient focussing of mesh resolution, to handle cylindrical and spherical shell domains and demonstrate that a significant reduction in the required number of degrees of freedom is possible while maintaing accuracy. Finally, to verify correctness, and evaluate and compare properties of various numerical schemes, we derive an extensive suite of analytical solutions to the Stokes equations governing mantle flow in cylindrical and spherical shell domains, with physically relevant boundary conditions. As a numerical benchmark they also serve to facilitate comparisons of different geodynamical models, and the further development of numerical techniques to improve these.

Contents

1 Introduction **17**

1.1 Fundamental Equations 18

1.1.1 Thermodynamics 20

1.2 Non-dimensionalisation and Approximations 22

1.2.1 Time and Length Scales 22

1.2.2 Reference State 23

1.2.3 Dimensionless Numbers 26

1.2.4 Non-dimensional equations 27

1.3 Fluidity 30

1.4 Fluidity for Geodynamical Modelling 32

1.5 Outline and Scope of Thesis 34

2 An Implicit Free Surface Algorithm for Geodynamical Simulations **38**

2.1 Introduction 38

2.2 Methodology 41

2.2.1 Equations 41

2.2.2 Discrete method 44

2.3 Analytical solutions 50

2.4 Test cases 55

2.4.1 Analytical comparison 55

2.4.2 Rayleigh-Taylor instability: 'drunken sailor' 66

2.5 Preliminary Conclusions 71

2.6 Further Developments 72

2.6.1 Stabilisation Method of Kaus 73

2.6.2 Eliminating the Free Surface Degrees of Freedom 76

2.6.3 Nonlinear approach 78

2.6.4 Stability Analysis and Exponential Time Integration 79

2.7 Final Conclusions 84

3 Analytical solutions for mantle flow in cylindrical and spherical shells 86

3.1 Introduction 87

3.2 Analytical Solutions 90

3.2.1 Equations 90

3.2.2 Cylindrical 90

3.2.3 Spherical 97

3.3 Numerical Discretisation in Fluidity 103

3.3.1 Discretisation 103

3.3.2 Isoparametric representation of the domain 104

3.3.3 Forcing term 105

3.3.4 Solving the linear system and dealing with nullspaces 105

3.4 Convergence Results . . . 106

3.5 Discussion . . . 111

3.5.1 Existing analytical benchmarks in shell domains . . . 111

3.5.2 Reduced order of convergence with discontinuous pressures . . . 112

3.6 Conclusions . . . 116

3.7 Equations in polar coordinates . . . 117

4 Mesh Adaptivity for Mantle Convection in Spherical Shell Domains 120

4.1 Introduction . . . 120

4.2 Metric-based Anisotropic Mesh Adaptivity . . . 123

4.2.1 The Metric . . . 123

4.2.2 Mesh Adaptivity Process . . . 126

4.2.3 Curved Surfaces and Geometry Preservation . . . 127

4.3 Mesh Adaptivity in Spherical Shell Domains . . . 129

4.3.1 Adapting the Geometry . . . 129

4.3.2 Base Geometry . . . 131

4.3.3 Coordinate Transformation . . . 132

4.3.4 Gnomonic Projection . . . 133

4.3.5 Avoiding Element Inversion . . . 136

4.3.6 Metric Transformation . . . 138

4.4 Test Cases . . . 138

4.4.1 Steady State . . . 138

4.4.2 Rising Plume in Spherical Domain . . . 141

4.5 Conclusions 147

5 Summary of Conclusions and Achievements **149**

5.1 Free Surface Methods 149

5.2 Analytical Solutions in Cylindrical and Spherical Shell Domains 151

5.3 Mesh Adaptivity in Spherical Shell Domains 151

5.4 Future directions 153

Bibliography **156**

Publications by Stephan Kramer on Geodynamical Modelling **172**

Other Publications by Stephan Kramer **175**

List of Symbols

c_p	Specific heat capacity at constant pressure
c_v	Specific heat capacity at constant volume
D	Depth of mantle
E	Specific total energy
e	Specific Internal energy
f	Forcing term: generic right-hand side term of the momentum equation
$\underline{f}$	Discretized forcing term (discrete vector)
g	Gravitational acceleration
g	Specific Gibbs free energy
G	Matrix representing discretised pressure gradient term. Its transpose represents (minus) the discretised divergence term in the continuity equation
$\boldsymbol{g} = -g\hat{\boldsymbol{r}}$	Downward gravitational vector
H	Specific heat production
H	Matrix representing discretized hydrostatic pressure boundary integral. Its transpose is used in the kinematic boundary condition.
$\underline{h} = \mathrm{H}\underline{\tilde{\eta}}$	Discretized hydrostatic pressure boundary integral in momentum equation.
$\overline{\overline{I}}$	Identity matrix (as tensor in physical space)
K	Matrix representing discretised viscosity term in Stokes system
k	Thermal conductivity
k	In chapter 3: polynomial order of forcing term for smooth cases.
l	In chapter 3: spherical harmonic degree
M	Pressure trial function / test function for continuity equation
m	In chapter 3: spherical harmonic order
$\boldsymbol{N}$	Velocity trial function / test function for momentum equation

n	In chapter 3: cylindrical wave number
$\boldsymbol{n}$	Normal vector (to the boundary)
p	Pressure
$\bar{p}(z)$	Reference pressure profile. After chapter one, we simplify $\bar{p} = \rho_0 g(z_0 - z)$
$p' = p - \bar{p}$	Pressure with (hydrostatic) reference pressure removed
$\underline{p'}$	Discretized pressure solution (discrete vector)
$\mathcal{P}$	Poloidal part in Mie decomposition
Q	Free surface test or trial function
R_-, R_+	Radius of Core-Mantle Boundary, and mantle outer radius
r	Radial coordinate
$\hat{\boldsymbol{r}}$	Upward (radial) unit vector
s	Specific entropy
t	Time
$\boldsymbol{t}$	Tangential vector (to the boundary)
T	Temperature
$\mathcal{T}$	Toroidal part in Mie decomposition
$\boldsymbol{u}$	Velocity
$\underline{u}$	Discretised velocity solution (discrete vector)
$v = 1/\rho$	Specifc volume
V	Discrete function space for velocity
W	Discrete function space for pressure
w	Vertical velocity component
$\boldsymbol{x} = (x, y, z)$	Physical coordinates
(r, φ, θ)	Spherical coordinates: radius, longitude, and co-latitude.
α	Thermal expansivity
$\gamma = \alpha/(\rho c_p \chi_a)$	Grüneisen parameter
Γ	Domain boundary
ϵ	In chapter 4: user selected target error bound
$\epsilon = \frac{\Delta\rho_0}{\rho_0}$	Ratio of perturbation to full density
η	Free surface elevation
$\tilde{\eta} = \Delta\rho g \eta$	Rescaled free surface (equivalent hydrostatic pressure)
$\underline{\tilde{\eta}}$	Discretised free surface solution (discrete vector)

θ	In chapter 3: co-latitude
θ	In chapter 2: coefficient in θ-scheme for time integration
$\kappa = k/(c_p\rho)$	Thermal diffusivity
μ	Dynamic viscosity
ν	Kinematic viscosity
ξ	In chapter 3 and 4: Local coordinates in reference element
$\overline{\overline{\sigma}} = \overline{\overline{\tau}} - p\overline{\overline{I}}$	Stress tensor, split in deviatoric and isotropic (pressure) parts
$\overline{\overline{\sigma}}' = \overline{\overline{\tau}} - p'\overline{\overline{I}}$	Stress tensor with hydrostatic pressure removed
$\overline{\overline{\tau}}$	Deviatoric stress tensor
φ	Longitude in spherical coordinates, or angle with x-axis in cylindrical coordinates
$\chi_a = \rho^{-1}\left(\frac{\partial\rho}{\partial p}\right)_s$	Adiabatic compressibility
$\chi_T = \rho^{-1}\left(\frac{\partial\rho}{\partial p}\right)_T$	Isothermal compressibility
Φ	Viscous dissipation
ψ	Streamfunction
Ω	Domain
$\mathbf{Ra}, \mathbf{Ra_H}$, $\mathbf{Pr}, \mathbf{M^2}, \mathbf{Di}$	Dimensionless numbers: Rayleigh (convection and internal heating), Prandtl, Mach (squared) and dissipation number. See table 1.1

Chapter 1

Introduction

Earth's mantle is the 2900 kilometre deep layer between the crust and core, which consists mostly of silicate rock. The temperature difference between the core at the Core Mantle Boundary (CMB) and Earth's surface drives a solid-state creep flow which causes the convection of material throughout the mantle with hot, buoyant material rising upwards and cooler and heavier material sinking downwards. This convective process is the driving mechanism behind many processes at the surface, such as plate tectonics, the formation and drift of continents, volcanism, earthquakes and mountain formation (e.g. Schubert et al., 2001). It also plays an important role in the structure of Earth's gravitational and magnetic fields.

Observations of the mantle structure and its convective processes are all indirect. By studying the response of seismic waves travelling through different parts of the mantle, one can infer differences in wave speed which can be related back to properties of the material they travel through, such as anisotropy, temperature and density. Phase transitions can be observed through reflections of these waves. These inferences rely on a good understanding of the chemical composition and physical properties, in particular at high pressure, of material at different depths in the mantle. This understanding is improved through laboratory experiments, and our knowledge of composition is enhanced by observations at the surface of material brought upwards through the mantle. However, the exact geochemistry and physical properties of material throughout the mantle remains a hotly debated topic. Another limitation of these observations

is their limited resolution, where some of the processes that are thought to play a key role in mantle dynamics, such as plumes, can not be adequately resolved.

Finally, and most importantly, seismic inversion only gives an insight into the present-day state of the mantle, whereas mantle convection is a process with timescales that play out over millions of years. Some temporal information can be obtained from remnants at the surface combined with our understanding of how these are related to processes, such as volcanism and plate kinematics that have taken place over geological timescales.

In the debate about the structure and dynamics of the mantle a key role is played by numerical models that simulate the process of mantle convection. Such geodynamical models are typically based on a numerical discretisation of the Stokes equations coupled with discretised equations for temperature (energy) and/or composition. A large number of such models have been developed in the scientific community(Baumgardner, 1985; Moresi et al., 1995; Tackley, 1996; Stadler et al., 2010; Kronbichler et al., 2012), with various approaches to the numerical discretisation, and a range of different physical capabilities such as the implementation of various rheologies, (pseudo)-compressibility and multi-phase properties.

1.1 Fundamental Equations

Under the approximation of the mantle as a viscous fluid, which neglects elastic properties of, in particular, the lithosphere (Patočka et al., 2019), the equations governing mantle convection can be related to the following three fundamental conservation laws (see e.g. Schubert et al., 2001; Davies, 2001):

Conservation of Mass:
$$\frac{\partial \rho}{\partial t} + \nabla \cdot \rho \boldsymbol{u} = 0, \tag{1.1}$$

Conservation of Momentum:
$$\frac{\partial \rho \boldsymbol{u}}{\partial t} + \nabla \cdot (\rho \boldsymbol{u}\boldsymbol{u}) + \nabla p - \nabla \cdot \overline{\overline{\tau}} = \rho \boldsymbol{g}, \tag{1.2}$$

Conservation of Energy:
$$\frac{\partial \rho E}{\partial t} + \nabla \cdot (\rho \boldsymbol{u} E) - \nabla \cdot (k \nabla T) + \nabla \cdot (p \boldsymbol{u}) - \nabla \cdot \left(\boldsymbol{u} \cdot \overline{\overline{\tau}}\right) = \rho \boldsymbol{g} \cdot \boldsymbol{u} + \rho H, \tag{1.3}$$

where $\rho, \boldsymbol{u}$, and p are the density, velocity and pressure of the material. The deviatoric stress tensor $\overline{\overline{\tau}}$ is given by

$$\overline{\overline{\tau}} = \mu \left(\nabla \boldsymbol{u} + (\nabla \boldsymbol{u})^T \right) \tag{1.4}$$

with dynamic viscosity μ. The source term on the right-hand side of the momentum balance represents gravity where $\boldsymbol{g} = -g\hat{\boldsymbol{r}}$ with gravitational acceleration g and $\hat{\boldsymbol{r}}$ the upward unit vector.

In the energy equation, the total energy per unit mass E can be broken down into the internal energy e and kinetic energy of the material:

$$E = e + \tfrac{1}{2}\boldsymbol{u} \cdot \boldsymbol{u}. \tag{1.5}$$

The thermal conduction term contains a thermal conductivity k and the right-hand side of the energy balance an internal heat production (per unit mass) H.

Applying the product rule to the first two terms of (1.2) and (1.3) and substitution of (1.1) in (1.2) and (1.3), and substitution of (1.2) in (1.3), the three balance equations can be simplified to

$$\text{Conservation of Mass:} \qquad \frac{\mathrm{D}\rho}{\mathrm{D}t} + \rho \nabla \cdot \boldsymbol{u} = 0, \tag{1.6}$$

$$\text{Conservation of Momentum:} \qquad \rho \frac{\mathrm{D}\boldsymbol{u}}{\mathrm{D}t} + \nabla p - \nabla \overline{\overline{\tau}} = \rho \boldsymbol{g}, \tag{1.7}$$

$$\text{Conservation of Energy:} \qquad \rho \frac{\mathrm{D}e}{\mathrm{D}t} + p \nabla \cdot \boldsymbol{u} = \nabla \cdot (k \nabla T) + \Phi + \rho H, \tag{1.8}$$

where we use the standard definition of total derivative

$$\frac{\mathrm{D}X}{\mathrm{D}t} = \frac{\partial X}{\partial t} + \boldsymbol{u} \cdot \nabla X, \tag{1.9}$$

and the shorthand Φ for the viscous dissipation term

$$\Phi = \overline{\overline{\tau}} : \nabla \boldsymbol{u}. \tag{1.10}$$

1.1.1 Thermodynamics

Through the first law of thermodynamics we may recognise that the left-hand side of (1.8), i.e. the sum of change in internal energy and work done through compression, for a parcel of material, must equal the amount of heat exchanged with its surroundings. When this heat exchange is carried out through some reversible process, then by the second law of thermodynamics this heat equals the temperature times the change in entropy

$$\rho\frac{\mathrm{D}e}{\mathrm{D}t} + p\nabla\cdot\boldsymbol{u} = \rho T\frac{\mathrm{D}s}{\mathrm{D}t}, \tag{1.11}$$

where s is the specific (i.e. per unit mass) entropy of the material. Defining $v = 1/\rho$, through (1.6) we have

$$\nabla\cdot\boldsymbol{u} = -v\frac{\mathrm{D}\rho}{\mathrm{D}t} = \rho\frac{\mathrm{D}v}{\mathrm{D}t}, \tag{1.12}$$

and thus

$$\frac{\mathrm{D}e}{\mathrm{D}t} + p\frac{\mathrm{D}v}{\mathrm{D}t} - T\frac{\mathrm{D}s}{\mathrm{D}t} = 0. \tag{1.13}$$

This motivates the definition of specific Gibbs free energy

$$g = e + pv - Ts. \tag{1.14}$$

Treating it as a function $g(x,t)$ of space and time for given state variables e, p, ρ, T and s as functions of space and time, we can derive

$$\frac{\mathrm{D}g}{\mathrm{D}t} = \frac{\mathrm{D}e}{\mathrm{D}t} + \frac{\mathrm{D}p}{\mathrm{D}t}v + p\frac{\mathrm{D}v}{\mathrm{D}t} - \frac{\mathrm{D}T}{\mathrm{D}t}s - T\frac{\mathrm{D}s}{\mathrm{D}t} \tag{1.15}$$

$$= v\frac{\mathrm{D}p}{\mathrm{D}t} - s\frac{\mathrm{D}T}{\mathrm{D}t}. \tag{1.16}$$

For a given material in an equilibrium thermodynamic state, we are able to pick any two of the state variables and compute the others from them (Schubert et al., 2001, section 6.8). It is then convenient to think of the specific Gibbs free energy as a function $g(p,T)$ of p and T, and

likewise for the other state variables $e(p,T)$, $v(p,T)$, and $s(p,T)$ so that we equivalently write

$$\frac{\mathrm{D}g}{\mathrm{D}t} = \frac{\partial g(p,T)}{\partial p}\frac{\mathrm{D}p}{\mathrm{D}t} - \frac{\partial g(p,T)}{\partial T}\frac{\mathrm{D}T}{\mathrm{D}t}, \tag{1.17}$$

which implies

$$\frac{\partial g(p,T)}{\partial p} = v, \quad \frac{\partial g(p,T)}{\partial T} = -s, \tag{1.18}$$

and

$$\frac{\partial^2 g(p,T)}{\partial p \partial T} = \frac{\partial v(p,T)}{\partial T} = \frac{\partial^2 g(p,T)}{\partial T \partial p} = -\frac{\partial s(p,T)}{\partial p}. \tag{1.19}$$

This relates the *thermal expansivity*, the change in volume of a material due to a change in temperature at constant pressure

$$\alpha = \rho(p,T)\frac{\partial v(p,T)}{\partial T} = -v(p,T)\frac{\partial \rho(p,T)}{\partial T}, \tag{1.20}$$

to a change in specific entropy due to a change in pressure at constant temperature. Similarly we define the change in volume of a material due to a change in pressure at constant temperature as its *isothermal compressibility*

$$\chi_T = -v(p,T)\frac{\partial v(p,T)}{\partial p} = v(p,T)\frac{\partial \rho(p,T)}{\partial p}. \tag{1.21}$$

We can also split the heat exchange expressed in (1.11) into contributions due to changes in temperature and pressure

$$\rho T\frac{\mathrm{D}s}{\mathrm{D}t} = \rho T\frac{\partial s(T,p)}{\partial T}\frac{\mathrm{D}T}{\mathrm{D}t} + \rho T\frac{\partial s(T,p)}{\partial p}\frac{\mathrm{D}p}{\mathrm{D}t}, \tag{1.22}$$

and define *specific heat capacity at constant pressure* as

$$c_p = T\frac{\partial s(T,p)}{\partial T}. \tag{1.23}$$

With definitions (1.20) and (1.23), and using (1.19) we can then finally rewrite the energy

equation as

$$\rho c_p \frac{\mathrm{D}T}{\mathrm{D}t} - \alpha T \frac{\mathrm{D}p}{\mathrm{D}t} = \nabla \cdot (k \nabla T) + \Phi + \rho H. \tag{1.24}$$

1.2 Non-dimensionalisation and Approximations

1.2.1 Time and Length Scales

To get a better handle on the relative importance of the different terms in these equations, for each (dimensional) physical quantity X we choose a representative value X_0 and introduce non-dimensionalised variable $\hat{X}$ such that $X = \hat{X} X_0$.

First we focus on the first terms on either side of (1.24)

$$\frac{\rho_0 c_{p0} T_0}{t_0} \hat{\rho} \hat{c_p} \frac{\partial \hat{T}}{\partial \hat{t}} + \cdots = \frac{k_0 T_0}{{x_0}^2} \hat{\nabla} \cdot \left(\hat{k} \hat{\nabla} \hat{T} \right) + \ldots, \tag{1.25}$$

where x_0 is the representative length scale such that in non-dimensionalised coordinates $\hat{x}$ we have $\nabla = \frac{1}{x_0} \hat{\nabla}$. We may identify this as a diffusion equation with a diffusion $\kappa = k/(c_p \rho)$ and thus $\kappa_0 = k_0/(c_{p0} \rho_0)$ and $\hat{\kappa} = \hat{k}/(\hat{c_p} \hat{\rho})$. Thus we can identify a time scale of diffusion of temperature over the entire mantle depth D

$$t_0 = \frac{D^2}{\kappa_0} = \frac{c_{p0} \rho_0 D^2}{k_0}, \tag{1.26}$$

choosing $x_0 = D$. A convenient choice for the scaling of velocity then is $u_0 = x_0/t_0 = \kappa_0/D$ which ensures that

$$\frac{\mathrm{D}}{\mathrm{D}t} = \frac{\partial}{\partial t} + \boldsymbol{u} \cdot \nabla = \frac{1}{t_0} \frac{\partial}{\partial \hat{t}} + \frac{u_0}{x_0} \hat{\boldsymbol{u}} \cdot \hat{\nabla} = \frac{1}{t_0} \frac{\mathrm{D}}{\mathrm{D}\hat{t}}, \tag{1.27}$$

and similarly a convenient scaling for pressure p is obtained by comparing the pressure gradient and viscosity terms in (1.7)

$$\nabla p + \nabla \cdot \tau = \frac{p_0}{x_0} \hat{\nabla} \hat{p} + \frac{\mu_0 u_0}{{x_0}^2} \hat{\nabla} \cdot \hat{\mu} \left(\hat{\nabla} \hat{\boldsymbol{u}} + \left(\hat{\nabla} \hat{\boldsymbol{u}} \right)^T \right), \tag{1.28}$$

which suggests a value of

$$p_0 = \frac{\mu_0 u_0}{x_0} = \frac{\mu_0 \kappa_0}{D^2}. \tag{1.29}$$

1.2.2 Reference State

In the mantle the pressure is close to hydrostatic equilibrium which means that the pressure is mostly determined by the weight of the column of rock above it. We therefore split the pressure into hydrostatic and deviatoric (dynamic) components

$$p = \bar{p} + p', \tag{1.30}$$

where the gradient of $\bar{p}$ balances the gravity term

$$\nabla \bar{p} = \bar{\rho} \boldsymbol{g}. \tag{1.31}$$

For a given density profile $\bar{\rho}$ as a function of depth, we can work out the hydrostatic pressure by integrating downwards, starting from a chosen reference level at the surface. The same could be done to compute the hydrostatic pressure of a more general, laterally varying density distribution ρ, but in this case only the vertical component of (1.31) would be balanced, but the lateral variations would also induce horizontal components of the pressure gradient, and thus its effect cannot be decoupled from the dynamics in the momentum equation.

We therefore assume a reference state $\bar{\rho}$ with an equation of state $\bar{\rho}(\bar{p}, \bar{T})$ where both $\bar{p}$ and $\bar{T}$ are only depth-dependent and constant in time, and similarly split

$$\rho = \bar{\rho} + \rho', \quad T = \bar{T} + T', \quad \boldsymbol{g} = -\left(\bar{g} + g'\right) \hat{\boldsymbol{r}}, \tag{1.32}$$

where $\frac{\partial \bar{p}}{\partial z} = \bar{\rho}\bar{g}$, and for simplicity we will assume $g' = 0$. By construction, this means we can subtract the reference state from the pressure gradient and gravity terms in (1.7), leaving respectively a gradient of the pressure deviation $\nabla p'$, and a *buoyancy* term $-\rho' \bar{g} \hat{\boldsymbol{r}}$.

In addition we assume that we can linearize the equation of state around the reference state

(Schubert et al., 2001):

$$\rho(T,p) = \rho(\bar{T},\bar{p}) + \rho' \tag{1.33}$$

$$\approx \rho(\bar{T},\bar{p}) + \left.\frac{\partial\rho(T,\bar{p})}{\partial T}\right|_{T=\bar{T}} T' + \left.\frac{\partial\rho(\bar{T},p)}{\partial p}\right|_{p=\bar{p}} p' \tag{1.34}$$

$$= \rho(\bar{T},\bar{p}) - \rho(\bar{T},\bar{p})\alpha(\bar{T},\bar{p})T' + \rho(\bar{T},\bar{p})\chi_T(\bar{T},\bar{p})p'. \tag{1.35}$$

We use overbarred $\bar{\rho}, \bar{\alpha}$, and $\bar{\chi_T}$ for the reference variables ρ, α, and χ_T evaluated at $T = \bar{T}, p = \bar{p}$ which can therefore be considered as a constant-in-time function of depth z only:

$$\rho = \bar{\rho} + \rho' = \bar{\rho}\left(1 - \bar{\alpha}T' + \bar{\chi_T}p'\right). \tag{1.36}$$

It should be noted that in general we cannot simply assume a given density profile $\bar{\rho}(z)$ and subsequently compute the pressure $\bar{p}$, as the density itself will, through the equation of state, depend on pressure. In fact, the bulk of the mantle's density variation is related to compression through increased pressure at depth. If we assume a reference density $\bar{\rho}$ that is adiabatic, i.e. we assume no heat transfer, then its variation due to reversible processes

$$\frac{\partial\bar{\rho}}{\partial z} = \frac{\partial\bar{\rho}(\bar{p},\bar{s})}{\partial\bar{p}}\frac{\partial\bar{p}}{\partial z} = \bar{\rho}\bar{\chi_a}\frac{\partial\bar{p}}{\partial z}, \tag{1.37}$$

in other words we assume it is determined by isentropic pressure variations, and exclude any isobaric contributions $\partial\bar{\rho}/\partial\bar{s}$. In combination with (1.31), we can solve an ODE for $\bar{\rho}(z)$, and we can define a characteristic length scale

$$\bar{h_d} = \left(\frac{1}{\bar{\rho}}\frac{\partial\bar{\rho}}{\partial z}\right)^{-1} = \frac{1}{\bar{\rho}\bar{\chi_a}\bar{g}} \tag{1.38}$$

over which density varies. By choosing a purely adiabatic reference state, we aim to separate the density, pressure and temperature variations due to compression, from the non-adiabatic variations which are associated with internal heating and heating through the CMB, and drive the mantle convection process. In particular this means that the variation in T' is not necessarily small, with an significant increase with depth across the mantle on top of the adiabatic

temperature profile $\bar{T}$.

As we split temperature and pressure into a reference and deviation, we also have to substitute this split in the total derivatives on the left-hand side of (1.24). The total derivatives of the reference profile however are just the vertical velocity w multiplied with a vertical derivative $\partial/\partial z$, so we can work out:

$$-\bar{\alpha}\left(\bar{T}+T'\right)\frac{\mathrm{D}\bar{p}}{\mathrm{D}t} = -\bar{\alpha}\left(\bar{T}+T'\right)w\frac{\partial\bar{p}}{\partial z} = -\bar{\alpha}\left(\bar{T}+T'\right)w\bar{\rho}\bar{g} \tag{1.39}$$

$$\rho\bar{c_p}\frac{\mathrm{D}\bar{T}}{\mathrm{D}t} = \rho\bar{c_p}w\frac{\partial\bar{T}}{\partial z} = \rho\bar{\alpha}\bar{T}\bar{g}w, \tag{1.40}$$

where in the derivation of the last step we use the fact that $\bar{T}$ is adiabatic (Schubert et al., 2001).

With these assumptions our equations take the following form:

$$\text{Mass:}\qquad \bar{\rho}\bar{\chi_T}\frac{\partial p'}{\partial t} - \bar{\rho}\bar{\alpha}\frac{\partial T'}{\partial t} + \nabla\cdot\bar{\rho}\left(1+\bar{\chi_T}p'-\bar{\alpha}T'\right)\boldsymbol{u} = 0, \tag{1.41}$$

$$\text{Momentum:}\qquad \bar{\rho}\left(1+\bar{\chi_T}p'-\bar{\alpha}T'\right)\frac{\mathrm{D}\boldsymbol{u}}{\mathrm{D}t} + \nabla p' - \nabla\bar{\bar{\tau}} = -\bar{\rho}\bar{\alpha}\bar{g}T'\hat{\boldsymbol{r}} + \bar{\rho}\chi_T p'\bar{g}\hat{\boldsymbol{r}}, \tag{1.42}$$

$$\text{Energy:}\qquad \bar{\rho}\left(1+\bar{\chi_T}p'-\bar{\alpha}T'\right)\left(\bar{c_p}\frac{\mathrm{D}T'}{\mathrm{D}t} + \bar{\alpha}\bar{g}w\bar{T}\right) - \bar{\alpha}\left(\bar{T}+T'\right)\left(\frac{\mathrm{D}p'}{\mathrm{D}t} + w\bar{\rho}\bar{g}\right) =$$

$$\nabla\cdot\left(k\nabla\left(\bar{T}+T'\right)\right) + \Phi + \bar{\rho}\left(1+\bar{\chi_T}p'-\bar{\alpha}T'\right)H. \tag{1.43}$$

To non-dimensionalise the reference state, we write

$$\rho = \rho_0\left(\hat{\bar{\rho}}+\hat{\rho}'\right) = \rho_0\hat{\bar{\rho}}\left(1-\alpha_0\Delta T_0\hat{\bar{\alpha}}\hat{T}' + \chi_{T0}p_0\hat{\bar{\chi}}_T\hat{p}'\right), \tag{1.44}$$

where α_0 and χ_{T0} are representative values for the reference state variables $\bar{\alpha} = \alpha_0\hat{\bar{\alpha}}$ and $\bar{\chi_T} = \chi_{T0}\hat{\bar{\chi}}_T$, and ΔT_0 is a value representative of the difference in non-adiabatic temperature T' across the mantle driving the mantle convection process.

1.2.3 Dimensionless Numbers

The choice of $u_0 = \kappa/D$ for the scaling of velocity does not imply that the typical velocity is of that magnitude, in fact in typical convection dominated mantle simulations $\hat{u} \gg 1$. A better estimate for the velocity of a density anomaly ρ' of size l sinking through a viscous fluid is obtained by comparing the viscosity and buoyancy terms in (1.42) which leads to (cf. Stokes law)

$$u \approx \frac{l_0^2 g_0 \rho'}{\mu_0}. \tag{1.45}$$

The Rayleigh number expresses the ratio of timescales l/u for convection and l^2/κ for diffusion over the length scale l. For the mantle where flow is driven by a density difference $\Delta\rho_0 = \rho_0\alpha_0\Delta T_0$, we obtain a Rayleigh number

$$\mathbf{Ra} = \frac{D^2/\kappa_0}{\mu_0/\left(D g_0 \rho_0 \alpha_0 \Delta T_0\right)} = \frac{D^3 \rho_0 g_0 \alpha_0 \Delta T_0}{\kappa_0 \mu_0}. \tag{1.46}$$

The perturbation density difference $\Delta\rho_0$ itself can be related to the representative value ρ_0 for (full) density through the dimensionless number

$$\boldsymbol{\epsilon} = \frac{\Delta\rho_0}{\rho_0} = \alpha_0 \Delta T_0. \tag{1.47}$$

We can also compare the diffusive time scale D^2/κ_0 with the viscous time scale D^2/ν_0, with kinematic viscosity $\nu_0 = \mu_0/\rho_0$, through the Prandtl number

$$\mathbf{Pr} = \frac{D^2/\kappa_0}{D^2/\nu_0} = \frac{\nu_0}{\kappa_0} = \frac{\mu_0}{\kappa_0 \rho_0}. \tag{1.48}$$

Focusing on terms in (1.41) and (1.42) linear in $(\boldsymbol{u}, p')$

$$\bar{\rho}\bar{\chi_T}\frac{\partial p'}{\partial t} + \nabla \cdot \bar{\rho}\boldsymbol{u} + \ldots = 0, \tag{1.49}$$

$$\bar{\rho}\frac{\partial \boldsymbol{u}}{\partial t} + \nabla p' + \ldots = 0, \tag{1.50}$$

we may recognise a wave equation with wave speed $c^2 = 1/(\bar{\rho}\bar{\chi_T})$. This wave speed is the speed

of sound and is in practice many orders of magnitude faster than the representative diffusive velocity u_0. We introduce the following dimensionless number, the Mach number, based on the ratio between the two

$$\mathbf{M^2} = \frac{{u_0}^2}{{c_0}^2} = \frac{\kappa_0^2 \rho_0 \chi_{T0}}{D^2} \tag{1.51}$$

To quantify the amount of compression, we can compare the characteristic length scale h_{d0} over which the density increases due to compression, calculated from (1.38) using representative values ρ_0, χ_{a0}, and g_0, with the actual depth of the mantle

$$\frac{D}{h_{d0}} = D\rho_0\chi_{a0}g_0 = \frac{1}{\bar{\gamma}}\mathbf{Di}. \tag{1.52}$$

which can also be computed (see Schubert et al. (2001) for details) as the ratio of the so called dissipation number

$$\mathbf{Di} = \frac{\alpha_0 g_0 D}{c_{p_0}}, \tag{1.53}$$

and the Grüneisen parameter

$$\gamma = \frac{\alpha}{\rho c_p \chi_a} \tag{1.54}$$

associated with the equation of state.

1.2.4 Non-dimensional equations

Using the definitions from the previous sections

$$\text{Mass:}\quad \mathbf{M^2Pr}\ \hat{\rho}\hat{\chi}_T\frac{\partial \hat{p}'}{\partial \hat{t}} - \epsilon\ \hat{\rho}\hat{\alpha}\frac{\partial \hat{T}'}{\partial \hat{t}} + \hat{\nabla}\cdot\hat{\rho}\left(1 + \mathbf{M^2Pr}\ \hat{\chi}_T\hat{p}' - \epsilon\ \hat{\alpha}\hat{T}'\right)\hat{\boldsymbol{u}} = 0, \tag{1.55}$$

$$\begin{aligned}\text{Momentum:}\quad & \frac{1}{\mathbf{Pr}}\hat{\rho}\left(1 + \mathbf{M^2Pr}\ \hat{\chi}_T\hat{p}' - \epsilon\ \hat{\alpha}\hat{T}'\right)\frac{\mathrm{D}\hat{\boldsymbol{u}}}{\mathrm{D}\hat{t}} + \hat{\nabla}\hat{p}' - \hat{\nabla}\hat{\bar{\tau}} = \\ & -\mathbf{Ra}\ \hat{\rho}\hat{\alpha}\hat{g}\hat{T}'\hat{\boldsymbol{r}} + \frac{\mathbf{Di}}{\gamma}\frac{\bar{c_p}}{\bar{c_v}}\hat{\rho}\hat{\chi}_T\hat{p}'\hat{g}\hat{\boldsymbol{r}},\end{aligned} \tag{1.56}$$

$$\begin{aligned}\text{Energy:}\quad & \hat{\rho}\left(1 + \mathbf{M^2Pr}\ \hat{\chi}_T\hat{p}' - \epsilon\ \hat{\alpha}\hat{T}'\right)\left(\hat{c_p}\frac{\mathrm{D}\hat{T}'}{\mathrm{D}\hat{t}} + \mathbf{Di}\ \hat{\alpha}\hat{g}\hat{w}\hat{\bar{T}}\right) - \hat{\alpha}\left(\hat{\bar{T}} + \hat{T}'\right)\left(\frac{\boldsymbol{\epsilon}\mathbf{Di}}{\mathbf{Ra}}\frac{\mathrm{D}\hat{p}'}{\mathrm{D}\hat{t}} + \mathbf{Di}\ \hat{\rho}\hat{g}\hat{w}\right) = \\ & \hat{\nabla}\cdot\left(\hat{k}\hat{\nabla}\left(\hat{\bar{T}} + \hat{T}'\right)\right) + \frac{\mathbf{Di}}{\mathbf{Ra}}\ \hat{\Phi} + \frac{\mathbf{Ra_H}}{\mathbf{Ra}}\ \left(1 + \mathbf{M^2Pr}\ \hat{\chi}_T\hat{p}' - \epsilon\ \hat{\alpha}\hat{T}'\right)\hat{H},\end{aligned} \tag{1.57}$$

Rayleigh number	$\mathbf{Ra}$	$10^7 - 10^9$
Internal heating Rayleigh number	$\mathbf{Ra}_H$	10^9
Prandtl number	$\mathbf{Pr}$	10^{23}
Mach number squared	$\mathbf{M^2}$	10^{-33}
	$\boldsymbol{\epsilon}$	$3 \cdot 10^{-2}$
Dissipation number	$\mathbf{Di}$	0.5
Grüneisen parameter	γ	1

Table 1.1: Some typical values for various non-dimensional number in the mantle. (based on Schubert et al. (2001)

where we have introduced an additional non-dimensional number

$$\mathbf{Ra_H} = \frac{\alpha_0 \rho_0^3 D^5 c_{p_0} H_0}{\mu_0 k_0^2}, \tag{1.58}$$

which measures the contribution of internal heating to the convective vigour (Schubert et al., 2001, section 6.10).

From table 1.1 we can see that the typical Prandtl number in the mantle is very high, which means that the viscous effect of the stress term in the momentum equation can be assumed to be immediate compared to the diffusive effect for temperature, and thus we can drop the $1/\mathbf{Pr}$ total derivative term in the momentum equation. Similarly, despite a high Prandtl number, the combination $\mathbf{M^2 Pr}$ is very small, and we likewise neglect terms scaled with it. Finally, $\boldsymbol{\epsilon}$ which measures the importance, relative to the full density, of density variations due to thermal expansion associated with non-adiabatic temperature differences, is small enough to neglect terms scaled with it. This means in all terms other than the buoyancy term, we only consider density variations associated with the vertical reference profile $\bar{\rho}$. These assumptions, and assumptions in previous sections lead to the so called anelastic liquid approximation.

Anelastic Liquid Approximation (ALA) Approximation

$$\text{Assumptions:} \qquad \frac{1}{\mathbf{Pr}} \ll 1, \quad \mathbf{M^2 Pr} \ll 1, \quad \boldsymbol{\epsilon} \ll 1, \tag{1.59}$$

$$\text{Mass:} \qquad \hat{\nabla} \cdot \hat{\bar{\rho}} \hat{\boldsymbol{u}} = 0, \tag{1.60}$$

$$\text{Momentum:} \qquad \hat{\nabla} \hat{p}' - \hat{\nabla} \hat{\bar{\tau}} = -\mathbf{Ra}\ \hat{\bar{\rho}} \hat{\bar{\alpha}} \hat{\bar{g}} \hat{T}' \hat{\boldsymbol{r}} + \frac{\mathbf{Di}}{\gamma} \frac{\bar{c}_p}{\bar{c}_v} \hat{\bar{\rho}} \hat{\bar{\chi}}_T \hat{p}' \hat{\bar{g}} \hat{\boldsymbol{r}}, \tag{1.61}$$

$$\text{Energy:} \qquad \hat{\bar{\rho}} \hat{\bar{c}}_p \frac{\mathrm{D}\hat{T}'}{\mathrm{D}\hat{t}} - \mathbf{Di}\ \hat{\bar{\alpha}} \hat{\bar{\rho}} \hat{\bar{g}} \hat{w} \hat{T}' = \hat{\nabla} \cdot \left(\hat{k} \hat{\nabla} \left(\hat{\bar{T}} + \hat{T}' \right) \right) + \frac{\mathbf{Di}}{\mathbf{Ra}}\ \hat{\Phi} + \frac{\mathbf{Ra_H}}{\mathbf{Ra}}\ \hat{\bar{\rho}} \hat{H}, \tag{1.62}$$

Note that the only time derivative left is in the energy equation (1.62), so that we can see the combination of (1.60) and (1.61) as a steady state system that we can solve for $\hat{p}'$ and $\hat{\boldsymbol{u}}$ for given $\hat{T}'$. The non-adiabatic temperature $\hat{T}'$ evolves over time according to (1.62) but this equation is also coupled to (1.60) and (1.61) via the velocity $\hat{\boldsymbol{u}}$, so that the three equations cannot be considered separately. Further coupling is typically added through the fact that the viscosity $\hat{\mu}$ used in $\hat{\bar{\tau}}$ is temperature dependent.

As we saw in section 1.2.3, the ratio $\mathbf{Di}/\gamma$ can be seen as a measure of density variation due to compression over the entire mantle depth. Although $\mathbf{Di}$ is not necessarily very small, including this variation does not have a very large effect on a vigorously convecting mantle, and the Boussinesq approximation, which neglects all density variations except for the buoyancy term, i.e. we use $\bar{\rho} = \rho_0$ elsewhere, simplifies the equations substantially.

Incompressible (Boussinesq) Approximation

$$\text{Assumptions:} \quad \frac{1}{\mathbf{Pr}} \ll 1, \quad \mathbf{M^2 Pr} \ll 1, \quad \boldsymbol{\epsilon} \ll 1, \mathbf{Di} \ll 1, \quad \bar{\rho} = \rho_0, \quad \bar{\alpha} = \alpha_0, \quad \bar{c_p} = c_{p0}, \quad \bar{g} = g_0, \tag{1.63}$$

$$\text{Mass:} \quad \hat{\nabla} \cdot \hat{\boldsymbol{u}} = 0, \tag{1.64}$$

$$\text{Momentum:} \quad \hat{\nabla}\hat{p}' - \hat{\nabla}\hat{\bar{\tau}} = -\mathbf{Ra}\, \hat{T}'\hat{\boldsymbol{r}}, \tag{1.65}$$

$$\text{Energy:} \quad \frac{\mathrm{D}\hat{T}'}{\mathrm{D}\hat{t}} = \hat{\nabla} \cdot \left(\hat{\kappa}\hat{\nabla}\left(\hat{\bar{T}} + \hat{T}'\right)\right) + \frac{\mathbf{Ra_H}}{\mathbf{Ra}}\, \hat{\bar{\rho}}\hat{H}. \tag{1.66}$$

Finally, an often used approximation in between the incompressible Boussinesq approximation, and the Anelastic Liquid Approximation (ALA), is the so called Extended Boussinesq Approximation (EBA). It uses the same approximation for the mass and momentum equations, using $\bar{\rho} = \rho_0$ in all terms except the buoyancy which is still dependent on ρ' (and not p'), but maintains the terms scaled with $\mathbf{Di}$ in the energy equation (1.62).

1.3 Fluidity

Fluidity is a finite element flow solver that started out as a general purpose Computational Fluid Dynamics (CFD) code (Pain, 2000), and has seen many applications over the years: ranging from the modelling of rock fracturing (Zimmerman et al., 2004), fluidised beds (Pain et al., 2001a), air pollution (Aristodemou et al., 2018), flow through porous media (Mostaghimi et al., 2015), in particular, oil and gas reservoirs (Jackson et al., 2015), fluid-structure interaction (Yang et al., 2016; Xiao et al., 2016), and reactor physics (Buchan et al., 2013) through coupling with the Boltzmann transport solver (Pain et al., 2006). One of its defining features is its dynamic, anisotropic mesh adaptivity (Pain et al., 2001b), which allows remeshing during the simulation to focus resolution on dynamically important features as they arise in the flow. This makes it particularly well-suited for multi-scale problems in which small scale and large scale features are tightly coupled.

As part of an effort to introduce these techniques to global ocean simulations (Pain et al., 2005; Piggott et al., 2008), a massive code re-engineering effort took place, which involved rewriting most of the code base in modern fortran, coupling to the PETSc (Balay et al., 2022) library to use its scalable linear solver algorithms, the introduction of rigorous continuous integration testing (Farrell et al., 2011), a new configuration system with an automatically generated graphical user interface (Ham et al., 2009) to make Fluidity's overwhelming number of configuration options more manageable, and novel interpolation schemes (Farrell et al., 2009; Farrell et al., 2011) to preserve physical conservation properties of the solution fields through an adapt.

Davies, Wilson, and Kramer, 2011 introduce Fluidity as a computational modelling framework for geodynamics, solving mantle convection under the incompressible Boussinesq, ALA, or EBA approximation. This required, among other things, to change the way the coupled mass (incompressibility) and momentum equations, cf. (1.64) and (1.65), which after discretisation lead to a so called saddle point system of equations, see e.g. (2.14), are solved for velocity and pressure. Such systems are typically solved using a Schur complement approach (see May et al., 2008, for an overview of different solution strategies to solve the Stokes saddle point system) which requires the inversion of the velocity block in the matrix, see e.g. (2.23) for the Schur complement of the matrix system in (2.22) with a velocity block K. In a typical Navier Stokes CFD solver, the viscosity and advection terms are decoupled from the coupled saddle point system, at the expense of temporal accuracy, and only an (approximation to) the time derivative remains which is easily invertible. In the Stokes equations however this velocity block contains the discretisation of the viscosity operator, and its coupling needs to be taken into account accurately. This leads to an iterative approach where the action of the inverse of the velocity block needs to be solved for in an inner iteration inside an outer iteration to solve the Schur complement system (for more details see Davies et al., 2011). In the paper, we demonstrate the effectiveness of, in particular *anisotropic*, mesh-adaptivity for mantle convection processes, and validate the code for a number of well established benchmarks.

Of particular relevance for mantle convection modelling is Fluidity's ability to simulate multi-material scenarios in which the distribution of multiple distinct materials is tracked each with

its own material properties, such as equation of state and rheology, through the domain. It uses a field-based approach using a number of volume fraction fields each associated with a material which are 1 where the material is present, and 0 where it is not. The materials are advected by advecting the corresponding volume fraction fields, using a control volume scheme with control volumes that are centred around the vertices. The challenge for both the numerical advection scheme, as well as the interpolation schemes used during the mesh adaptation stage, is that these need to conserve the volume of the individual materials, stay bounded - both the individual volume fractions as well as the sum of these fractions need to stay strictly between 0 and 1 - and are minimally dissipative maintaining sharp interfaces between the materials without introducing spurious mixing. For more details see Wilson (2010).

1.4 Fluidity for Geodynamical Modelling

Fluidity has already been applied in a large number of mantle convection studies. This section provides a brief overview of studies that apply Fluidity for geodynamical modelling that I have contributed to. See page 172 for a list of publications.

The combination of material tracking and mesh adaptivity makes it particularly well suited for the study of subduction zones. Garel et al. (2014) study the interaction of subducted slabs under an overriding plate with the mantle transition zone and classify four distinct subduction regimes controlled by the age of the subducting and overriding plate as they influence their relative strength and buoyancy. Le Voci et al. (2014) studies influence of hydration and buoyancy on the flow regime and thermal structure in the mantle wedge between subducting and overriding plate which is important for understanding arc volcanism. This was extended in Davies et al. (2015) to 3D models of the mantle wedge. Perrin et al. (2016) uses thermobarometry (Lee et al., 2009) to chemically determine the equilibration pressures and temperatures of primitive arc lavas from worldwide intraoceanic subduction zones and compare them to kinematically driven thermal wedge models in Fluidity.

Another good example where anisotropic mesh adaptivity can deliver significant reductions in

computational costs, is in the modelling of thermal plumes in the mantle. Jones et al. (2016) uses Fluidity to study whether heterogeneities present in deep mantle material are preserved when it is transported through plume conduits to the Earth's surface. These heterogeneities have been proposed as a potential explanation of spatial variation in the geochemistry of hotspot lavas, such as that observed in the double hotspot track of Hawaii. The Fluidity models in Jones et al. (2016) however demonstrate that materials with different density and viscosity do not maintain their spatial distribution present at the base of the plume, rather the denser material ends up being concentrated nearer to the centre of the plume. Jones et al. (2017) proposes an alternive explanation of the lateral variation in the double hotspot track of Hawaii based on a directional change in the Pacific plate motion coinciding with the emergence of the double volcanic track. This is motivated through a combination of a geochemical analysis to explain the melt at different depths of the melt products, which combined with a significant tilt of the plume and a relatively recent change in the motion of the Pacific plate explaining the lateral variation in the form of two geochemically distinct types of volcanic tracks. The mechanics of this potential mechanism are then verified in Fluidity in plume models enforcing a similar change in plate motion at the top.

Not all intraplate volcanic activity is thought to be associated with hotspot activity. Edge-driven convection and shear-driven upwelling are two other mechanisms thought to play a role in a number of intraplate volcanic provinces. Duvernay et al. (2021) studies these mechanisms in a number of 2D and 3D Fluidity models that use Fluidity's recently implemented particle-in-cell method (Mathews, 2021) to track the occurence of melting. Another aspect of intraplate volcanism that is poorly understood is the interaction of mantle plumes with the continental lithosphere, where the heterogenous structure of the lithosphere complicates our understanding of how this interaction relates to the volcanic surface expression. In Duvernay et al. (2022) a number of 3D models demonstrate this complex relation. Plumes located below thick cratonic lithosphere inhibit melting but the material transported upwards may be channeled away laterally due to lithospheric gradients, leading to magmatism that is located far away from the main conduit and which may be concentrated near step changes making it hard to distinguish from that generated by edge driven convection.

Davies et al. (2019) provide an improved statistical analysis of the power spectrum of residual topography, the difference between observed topography and isostatic topography (see the next section), and tries to reconcile this with predicted dynamic topography from global mantle models in Fluidity. It is shown that this is only possible if the lithospheric structure is correctly incorporated in the models. Finally, as discussed in section 4.5, the extensions of Fluidity's adaptivity capabilities to spherical domains, detailed in chapter four, have already been applied in Chen et al., 2022a and Chen et al., 2022b which studies the effect of sphericity on subduction zone models.

1.5 Outline and Scope of Thesis

This thesis consists of three related topics in the numerical modelling of mantle convection.

Chapter two of this thesis describes a new free surface method, implemented in Fluidity, that deals with a well-known numerical instability in mantle convection modelling in the presence of a free surface. The separation of the hydrostatic pressure component from the dynamics of the convection process, as introduced in section 1.2.2, relies on the assumption that this hydrostatic pressure can be integrated downwards from a horizontal, i.e. perpendicular to gravity, reference level of equal pressure. Taking into account that the location where the external pressure is actually applied is determined by topography however, this difference in height leads to a horizontal variation in hydrostatic pressure in the mantle, due to the difference in weight of the material above in each vertical column, even when assuming a constant density. This difference can drive mantle flow with the topography evolving accordingly, which would, in the absence of any other dynamics and again ignoring density differences, restore the topography of the mantle to a level top surface.

The existing topography of Earth's surface is primarily associated with lateral density differences near the surface, in the crust and lithosphere (Flament et al., 2013), in which the density differences are hydrostatically balanced with variations in topographical height. This so called *isostatic topography* is therefore decoupled from the dynamics of the mantle. In contrast, *dy-*

namic topography is topography which is supported by dynamics in the mantle and as such dynamically adapts to the flow in the mantle as it evolves. In this adjustment process the surface over, e.g., a region in the mantle with upwelling hot material is uplifted gradually until the hydrostatic pressure has increased sufficiently, due to the increased surface height, to balance the push from the upwards mantle flow below.

In a numerical model this vertical movement of the surface can be tracked by tracking the velocity of the mantle at the surface. The effect of increased hydrostatic pressure can then be simulated by either moving the mesh nodes (Lagrangian approach) at the surface boundary, or by simply applying the increased hydrostatic pressure as a boundary condition at a fixed boundary (Eulerian approach). If this adjustment is done at the end of each timestep, corresponding to an explicit time stepping method, the effect of the increased hydrostatic pressure is not felt immediately, and thus, in a sense, the mantle flow is free to push up material without any immediate feedback over the duration of a timestep. This causes a numerical instability, which as I will demonstrate in chapter two can be prevented by introducing implicit time integration. This requires the vertical position of the free surface to be solved in conjunction with the velocity and pressure of the Stokes system. Moreover, I will show that this method, which can be viewed as an implicit (backward) Euler time integration, in contrast to the explicit (forward) Euler time integration, can be improved upon by its second-order Crank-Nicolson variant with a considerable improvement in the temporal accuracy of the method. To test the new method I demonstrate its performance against an expanded set of analytical benchmark cases with a free surface based on Zhong et al. (1996), as well as demonstrating that our method remains numerically stable in the two-material Rayleigh-Taylor instability case (Kaus et al., 2010) which has a known numerical instability for large timesteps.

The method, which also appeared in Kramer, Wilson, and Davies, "An implicit free-surface algorithm for geodynamical simulations" (2012), is further analysed and discussed alongside a number of more recent publications on this topic, in section 2.6. I show that the free surface degrees of freedom can be eliminated, and that the method, evaluated in a fixed Eulerian frame, can be related to the stabilisation method of Kaus et al. (2010) for Lagrangian free surface models. Furthermore we derive a formal stability criterion inspired by analysis from

Rose et al. (2017).

The importance of analytical test cases to rigorously study the performance of different numerical schemes is highlighted in chapter two. The set of solutions worked out in that chapter, and in the appendix of Kramer et al., 2012, have already been used in a number of publications for the verification, analysis, and comparison of free surface methods (Furuichi et al., 2015; Rose et al., 2017; Wilson et al., 2017). A number of analytical benchmark solutions exist for Stokes flow in Cartesian boxes in two or three dimensions. To construct such analytical solutions in the spherical shell domain of Earth's mantle, or even in its two-dimensional cylindrical shell approximation, with appropriate boundary conditions, is a lot more involved.

In *chapter three* I derive a set of in total eight analytical solutions in cylindrical and spherical shell domains, with free slip and zero slip boundary conditions and with either a generic monomial (single term polynomial) right-hand side forcing term, or an infinitely thin density anomaly. The solutions have also been implemented in a python package (Kramer, 2020) and thus made readily available to the geodynamical modelling community. In demonstrating the use of this set of analytical solutions in convergence studies, we discuss the lack of convergence for continuous discretisations of pressure, such as in the popular Taylor Hood element pair, in the presence of a jump in the pressure solution. One of the eight cases (spherical, free slip with infinitely thin density anomaly) has previously been used as a benchmark, based on Zhong et al. (2008a) in a number of other publications for different geodynamical models (Davies et al., 2013; Burstedde et al., 2013; Liu et al., 2019), but since these only looked at surface diagnostics, they failed to notice the lack of convergence in the interior which contains a pressure discontinuity. Having the full analytical solution readily available makes it a lot easier to do this analysis, also in other models. As an example, we have already verified the correct convergence (including the lack of convergence for continuous discretisations to a discontinuous pressure solution) in the new Firedrake (Rathgeber et al., 2016)-based model G-ADOPT (Davies et al., 2022) using these solutions.

Chapter four discusses the use of mesh adaptivity for geodynamical models in spherical shell domains. The efficacy of mesh adaptivity, in particular anisotropic mesh adaptivity, was already

demonstrated in Davies et al. (2011) for Cartesian domains. Here we discuss some of the issues to make this technique available in curved spherical or cylindrical domains, and a relatively simple approach to overcome these. As before, we demonstrate the functionality and efficiency of the method using a number of relevant benchmarks. The methods have already been applied, enabling the modelling of subduction zones in spherical geometries in Chen et al., 2022a and Chen et al. (2022b).

Taken together this thesis represents a considerable contribution to the development of accurate and efficient numerical models of thermal convection processes in Earth's mantle.

Chapter 2

An Implicit Free Surface Algorithm for Geodynamical Simulations

This chapter introduces a new free surface method for geodynamical simulations. It is based on Kramer, Wilson, and Davies, "An implicit free-surface algorithm for geodynamical simulations" (2012) but has been rearranged and adapted to fit the structure of this thesis. An additional section, section 2.6, discusses further developments in the literature since then and the various approaches to free surface modelling that have been taken. It also shows that the implicit method, presented and analysed in sections 2.1 to 2.5, which requires additional free surface degrees of freedom and which is evaluated in a fixed Eulerian frame, can be seen, through elimination of these degrees of freedom, to be related to the stabilisation method of Kaus et al. (2010) for Lagrangian free surface models. Furthermore we formally demonstrate unconditional stability of the implicit method for $\theta > \frac{1}{2}$ using the analysis of Rose et al. (2017), although we come to a different conclusion.

2.1 Introduction

While the majority of Earth's present-day surface topography results from crustal and lithospheric thickness variations, generated by the movement of tectonic plates along Earth's surface,

there is mounting evidence to suggest that a significant proportion results from viscous stresses created by flow within Earth's mantle. Although such dynamic topography is transient, it can exert a substantial influence upon surface processes (Braun, 2010); it has, for example, played a role in the geological evolution of the North American continent (Liu et al., 2008; Spasojevic et al., 2009), the establishment of Amazon drainage patterns (Shephard et al., 2010) and in controlling the overflow of North Atlantic Deep Water across the Greenland-Scotland Ridge (Wright et al., 1996; Poore et al., 2009). In turn, surface processes, such as erosion of topography and deposition of eroded sediments at oceanic trenches, may actively influence patterns of deformation, affecting plate motions and mantle flow (e.g. Koons, 1990; Molnar et al., 1990; Beaumont et al., 1996; Willett, 1999; Beaumont et al., 2001; Braun, 2006; Braun, 2010; Kaus et al., 2008; Iaffaldano et al., 2006; Iaffaldano et al., 2011).

Key to an improved understanding of the interactions between surface processes and mantle and lithosphere dynamics are numerical models of this coupled system. However, to model such interactions in a self-consistent manner, one must take into account Earth's free surface, which has, thus far, proved challenging. Several distinct methods are currently used to simulate surface topography in geodynamical models. Dynamic topography may be derived from the normal stress at a free slip boundary (Hager et al., 1985; McKenzie, 1977; Zhong et al., 1993). This approach however ignores the timescales involved in the response of surface topography to changes in the interior. In studies by Zhong et al. (1996) and Gurnis et al. (1996) it is shown how the history-dependent free surface evolution can be taken into account by adjusting the normal stress boundary condition, to include topographic stresses based on the evolution of free surface height calculated in the previous timestep. This method modifies the boundary condition at the surface in an unchanged Eulerian mesh.

Methods that do move the mesh to follow topography include fully Lagrangian schemes (e.g. Melosh et al., 1980; Lavier et al., 2000), in which all calculations are done on a Lagrangian mesh that follows the flow velocity, and Arbitrary Lagrangian-Eulerian (ALE) methods (e.g. Fullsack, 1995) that employ a mesh that does not necessarily move with the flow velocity everywhere. For these methods a zero normal stress boundary condition can be applied naturally at the moving free surface. Other free surface modelling approaches include: using marker chain or level set

functions to track the free surface on a background Eulerian mesh (e.g. Harlow et al., 1965; Muhlhaus, 2007); and the 'sticky-air' approximation, where a low viscosity, low density layer is placed above a free slip boundary, thus allowing the material interface to behave similarly to a free surface (Schmeling et al., 2008; Crameri et al., 2012).

While each method has its own advantages and disadvantages (for a detailed discussion see Crameri et al., 2012), most approaches pose limitations on the computational timestep. To ensure numerical stability in free surface simulations, the computational timestep must often be at least an order of magnitude less than the timestep in an identical simulation employing a free slip boundary. This is due to the temporally explicit coupling between free surface movement, which is computed at a previous timestep, and the resulting topographic stresses; an upward velocity at the free surface does not feel the increasing (decreasing) load from rising (falling) topography until the next timestep. As a consequence, with current methods, free surface simulations are computationally expensive, and are generally considered intractable for global mantle convection models (e.g. Bunge et al., 2002; Tackley, 2008; Zhong et al., 2008b; Wolstencroft et al., 2009; Davies et al., 2009; Styles et al., 2011).

In an attempt to overcome this issue, Kaus et al. (2010) introduce a free surface stabilisation approach, which adds stabilisation terms to the momentum equation, mimicking the feedback of changing topography on the underlying dynamics. Such an approach allows for larger timesteps with free surface simulations and maintains solution accuracy. An alternative approach, which appears to have similar benefits (Fuchs et al., 2011), is presented by Schmeling et al. (2008), based upon a 4th order Runge Kutta scheme combined with a predictor corrector step for advecting markers. In this chapter, we introduce a new free surface method, equally applicable to both Eulerian and Lagrangian models, in which free surface elevation is treated as an independent variable that is solved for in conjunction with the momentum and continuity equation, using *implicit* time integration. This removes the timestep constraint without the need for additional stabilisation terms. Moreover, we show that the method can be made second order accurate in time at no additional cost, where previous methods are only first order accurate. The method therefore dramatically improves computational efficiency, allowing for far larger timesteps than explicit free surface methods, whilst maintaining solution accuracy.

The structure of the chapter is as follows: we begin by presenting an overview of our methodology, including the governing equations and boundary conditions, where the boundary conditions are dealt with in a manner similar to Zhong et al. (1996). We then demonstrate that the solution strategy employed for an implicit free surface treatment requires only a minor modification from our standard solution strategy for velocity and pressure, as implemented in Fluidity (Davies et al., 2011). An explicit free surface method is also described, as we use this for comparative purposes. We work out a number of analytical benchmark solutions in a Cartesian box involving free surface boundary conditions both at the top (Earth's surface) and bottom (Core-Mantle Boundary). We next present the results of a series of test cases, based on these analytical solutions as well as on previously published benchmarks, which demonstrate the computational efficiency and physical accuracy of our method. We end by discussing the advantages of the method and its potential use in large-scale geodynamical models.

2.2 Methodology

2.2.1 Equations

To explain the boundary conditions employed at the free surface, we start from the incompressible Stokes equations with a pressure that includes the hydrostatic component, in other words we are solving equations (1.64) and (1.65), returning to dimensional variables and, at first, maintaining the original full gravity term $\rho g \hat{\boldsymbol{r}}$ on the right-hand side, and thus also the full pressure gradient ∇p on the right-hand side.

$$\begin{aligned} -\nabla \cdot \overline{\overline{\tau}} + \nabla p &= -\left(\rho_0 + \rho'\right) g \hat{\boldsymbol{r}}, \\ \nabla \cdot \boldsymbol{u} &= 0, \end{aligned} \tag{2.1}$$

with velocity $\boldsymbol{u}$, deviatoric stress tensor

$$\overline{\overline{\tau}} = \mu \left(\nabla \boldsymbol{u} + (\nabla \boldsymbol{u})^T \right), \tag{2.2}$$

μ is the dynamic viscosity, full pressure p, gravitational acceleration g and $\hat{\boldsymbol{r}}$ a unit vector in the upward direction. We assume a density distribution $\rho = \rho_0 + \rho'$, where ρ_0 is the reference density $\bar{\rho} = \rho_0$ and ρ' a perturbation density. These equations are considered together with the following boundary conditions:

$$\text{No slip: } \boldsymbol{u} = \boldsymbol{0} \tag{2.3}$$

$$\text{Free slip: } \begin{cases} \boldsymbol{u} \cdot \boldsymbol{n} = 0, & \text{(2.4a)} \\ \boldsymbol{n} \cdot \overline{\overline{\tau}} \cdot \boldsymbol{t} = 0, & \text{(2.4b)} \end{cases}$$

$$\text{Free surface: } \begin{cases} \boldsymbol{n} \cdot \boldsymbol{u} = \dfrac{\partial \eta}{\partial t} \boldsymbol{n} \cdot \hat{\boldsymbol{r}}, & \text{(2.5a)} \\ \boldsymbol{n} \cdot \left(\overline{\overline{\tau}} - p\overline{\overline{I}} \right) = \boldsymbol{0}. & \text{(2.5b)} \end{cases}$$

Here, $\boldsymbol{n}$ is the outward pointing normal vector to the boundary and $\boldsymbol{t}$ any tangential vector. At the free surface, the kinematic boundary condition (2.5a) relates the normal velocity to the movement of the free surface. This movement is given by the time-derivative of the free surface elevation η, which measures the distance, in the upward direction, between a fixed reference plane $z = z_0$ and the free surface at $z = z_0 + \eta$. The inner product $\boldsymbol{n} \cdot \hat{\boldsymbol{r}}$ takes into account potential different directions of this normal velocity and the upward direction $\hat{\boldsymbol{r}}$. Indeed, at the core-mantle-boundary, these are opposite and the inner product becomes negative. The second condition (2.5b), assuming a void with zero pressure on the outside of the domain, enforces a zero stress condition on the stress tensor

$$\overline{\overline{\sigma}} = \overline{\overline{\tau}} - p\overline{\overline{I}}, \tag{2.6}$$

where $\overline{\overline{I}}$ is the identity matrix.

Removal of hydrostatic pressure

As explained in section 1.2.2, a common step when solving equations (2.1) - (2.5) is to subtract the main hydrostatic component from the full pressure p, and solve in terms of a perturbation pressure $p' = p - \rho_0 g(z_0 - z)$, where z is defined as positive upwards. Using the definition of the stress tensor in terms of perturbation pressure: $\overline{\overline{\sigma}}' = \overline{\overline{\tau}} - p'\overline{\overline{I}}$, the governing equations become:

$$\begin{aligned} -\nabla \cdot \overline{\overline{\sigma}}' &= -\rho' g \hat{\boldsymbol{r}}, \\ \nabla \cdot \boldsymbol{u} &= 0. \end{aligned} \tag{2.7}$$

Because $\boldsymbol{n} \cdot \overline{\overline{\sigma}}' \cdot \boldsymbol{n} = \boldsymbol{n} \cdot \overline{\overline{\sigma}} \cdot \boldsymbol{n} - \rho_0 g(z - z_0)$, the normal component of (2.5b) changes to:

$$\boldsymbol{n} \cdot \overline{\overline{\sigma}}' \cdot \boldsymbol{n}\Big|_{z=z_0+\eta} = -\rho_0 g \eta. \tag{2.8}$$

Now the hydrostatic component has been removed, the vertical variation of $\overline{\overline{\sigma}}'$ near the free surface boundary has become significantly smaller. As a result, we can approximate the influence of topography in our model without actually changing the geometry, and apply boundary condition (2.8) at the reference level $z = z_0$. Since the local density ρ may differ from the reference ρ_0, due to thermal and compositional heterogeneity, we also take into account the hydrostatic pressure variation associated with the perturbation density ρ', by using the full local density:

$$\boldsymbol{n} \cdot \overline{\overline{\sigma}}' \cdot \boldsymbol{n}\Big|_{z=z_0} = -\rho g \eta. \tag{2.9}$$

Because this boundary condition is evaluated at a fixed level $z = z_0$, it can be easily implemented in a Eulerian model, without having to move the mesh. Note that in this case the normal $\boldsymbol{n}$ is simply pointing upwards (or downwards for a bottom free surface), so that $\boldsymbol{n} \cdot \overline{\overline{\sigma}}' \cdot \boldsymbol{n}$ simplifies to σ'_{zz} and the inner product $\boldsymbol{n} \cdot \hat{\boldsymbol{r}}$ in (2.5a) is simply a factor of $+1$ or -1 for top and bottom free surfaces, respectively.

The model equations with this boundary condition, the same as used in Zhong et al. (1996), form a linear system, whereas the zero normal stress condition (2.5b) applied at exactly $z = z_0 + \eta$ leads to a non-linearity. However, the difference between the two formulations is only significant

if the amplitude of the topography is of the same order as the horizontal length scales involved (as shown in Crameri et al., 2012).

To model the case where the zero normal stress condition is evaluated at exactly $z = z_0 + \eta$, the computational mesh must be moved with the free surface, using, for example, ALE methods (Fullsack, 1995; Jimack et al., 1991). We would like to emphasise that with such moving mesh methods, we can still subtract the reference hydrostatic pressure and use boundary condition (2.8). Note that in such cases, we have to use ρ_0 as opposed to ρ, since the hydrostatic pressure associated with the perturbation density is already taken into account by the change in volume of cells near the free surface. Using this form of the boundary condition however, the free surface method presented in the following sections remains applicable and offers the same second order accuracy and improved stability. The method is therefore equally applicable to ALE discretisations. In all results presented here however, a fixed Eulerian mesh is used as moving the mesh would have a negligible influence on the cases examined.

Finally, rather than assuming a zero external pressure, we may also consider the movement of a free surface into a region of different density ρ_{ext}. Examples include an ocean above Earth's crust and the higher density core below Earth's mantle. In such cases, we assume an ambient hydrostatic pressure, $p_{\text{ext}} = -\rho_{\text{ext}} g z$, which modifies the normal stress boundary condition as follows:

$$\boldsymbol{n} \cdot \overline{\overline{\sigma}}' \cdot \boldsymbol{n} \Big|_{z=z_0} = -\Delta\rho g \eta, \tag{2.10}$$

where $\Delta\rho = \rho - \rho_{\text{ext}}$.

2.2.2 Discrete method

For the weak form of (2.7) we multiply the momentum equation and continuity equation with vector- and scalar-valued test functions $\boldsymbol{N}$ and M respectively, and integrate over the domain Ω. Furthermore, we integrate by parts the deviatoric stress and velocity divergence terms,

yielding surface integrals across the boundary Γ. The resulting equations are:

$$\begin{aligned}\int_\Omega \nabla \boldsymbol{N} : \overline{\overline{\tau}} - \int_\Omega \boldsymbol{N} \cdot \nabla p' - \int_\Gamma \boldsymbol{N} \cdot \overline{\overline{\tau}} \cdot \boldsymbol{n} = -\int_\Omega \boldsymbol{N} \cdot \hat{\boldsymbol{r}} \rho' g, \\ \int_\Omega (\nabla M) \cdot \boldsymbol{u} - \int_\Gamma M \boldsymbol{n} \cdot \boldsymbol{u} = 0.\end{aligned} \tag{2.11}$$

On free slip and no slip boundaries, the normal velocity, $\boldsymbol{n} \cdot \boldsymbol{u}$, is zero and the boundary integral drops out from the continuity equation. However, for free surface boundaries this integral remains. On these boundaries, we wish to weakly impose (2.10) and do so by substitution of this equation into the $\overline{\overline{\tau}}$ boundary integral in the momentum equation:

$$\int_\Omega \nabla \boldsymbol{N} : \overline{\overline{\tau}} - \int_\Omega \boldsymbol{N} \cdot \nabla p' - \int_{\Gamma_{\text{no/free slip}}} \boldsymbol{N} \cdot \overline{\overline{\tau}} \cdot \boldsymbol{n} - \int_{\Gamma_{\text{free surface}}} \boldsymbol{N} \cdot \boldsymbol{n} \left(p' - \Delta \rho g \eta\right) = -\int_\Omega \boldsymbol{N} \cdot \hat{\boldsymbol{r}} \rho' g, \tag{2.12a}$$

$$\int_\Omega (\nabla M) \cdot \boldsymbol{u} - \int_{\Gamma_{\text{free surface}}} M \boldsymbol{n} \cdot \boldsymbol{u} = 0. \tag{2.12b}$$

Explicit free surface method

In this chapter we assume a standard Continuous Galerkin finite element discretisation of (2.12) as outlined in Davies et al., 2011, in which the discrete velocity and pressure solutions are written as linear combinations of a set of basis functions $\boldsymbol{N}_b$ and M_a respectively:

$$\boldsymbol{u} = \sum_b u_b \boldsymbol{N}_b \text{ and } p' = \sum_a p'_a M_a. \tag{2.13}$$

This leads to a discrete linear system of equations:

$$\begin{pmatrix} \mathrm{K} & \mathrm{G} \\ \mathrm{G}^T & 0 \end{pmatrix} \begin{pmatrix} \underline{u} \\ \underline{p}' \end{pmatrix} = \begin{pmatrix} \underline{f} - \underline{h} \\ 0 \end{pmatrix}, \tag{2.14}$$

where $\underline{u}$ and $\underline{p}'$ are vectors of the coefficients u_b and p'_a. The matrices K and G and right-hand

side vectors $\underline{f}$ and $\underline{h}$ are given by:

$$\begin{aligned}
\mathrm{K}_{bc} &= \int_\Omega [\nabla \boldsymbol{N}] : \left[\mu \left(\nabla \boldsymbol{N} + (\nabla \boldsymbol{N})^T\right)\right], \\
\mathrm{G}_{ba} &= \int_\Omega (\nabla M_a) \cdot \boldsymbol{N}_b - \int_{\Gamma_{\text{free surface}}} M_a \boldsymbol{N}_b \cdot \boldsymbol{n}, \\
\underline{f}_b &= -\int_\Omega \boldsymbol{N}_b \cdot \hat{\boldsymbol{r}} \rho' g, \quad \underline{h}_b = \int_{\Gamma_{\text{free surface}}} \boldsymbol{N}_b \cdot \boldsymbol{n} \Delta\rho g \eta.
\end{aligned}$$

Note that the pressure boundary integral in the momentum equation (2.12) and the normal velocity boundary integral in the continuity equation (both are integrals over the free surface) give rise to the same contribution to the discrete pressure gradient operator G and the discrete divergence operator G^T, so that the system remains symmetric. The η boundary integral in the momentum equation has been added as an additional term $-\underline{h}$ on the right-hand side. The boundary integrals for no-slip and free slip disappear through the application of strong Dirichlet boundary conditions for velocity and weakly imposing zero shear stress on the free slip boundaries (see Davies et al., 2011).

The explicit free surface method tracks free surface elevation η by a simple backward Euler time integration of the kinematic boundary condition, meaning that at the end of a timestep the free surface is updated using the latest velocity:

$$\eta^{n+1} = \eta^n + \frac{\Delta t}{\boldsymbol{n} \cdot \hat{\boldsymbol{r}}}\, \boldsymbol{u}^n \cdot \boldsymbol{n}. \tag{2.15}$$

This new η^{n+1} is used in the next timestep to compute the right-hand side term $\underline{h}$.

For consistency with the implicit method introduced in the next section, we define a rescaled free surface variable $\tilde{\eta} = \Delta\rho g \eta$, and discretise it by a linear combination of basis functions Q_d:

$$\tilde{\eta} = \sum_d \tilde{\eta}_d Q_d. \tag{2.16}$$

The functions Q_d are finite element basis functions along the free surface only, associated with node d in a surface mesh. For the results presented here we obtain these by restricting the pressure basis functions M_a to the free surface. The equation that updates the free surface

values after each timestep then follows from a standard Galerkin discretisation:

$$\sum_e \mathrm{F}_{de}\tilde{\eta}_e^{n+1} = \sum_e \mathrm{F}_{de}\tilde{\eta}_e^{n} + \Delta t \int_{\Gamma_{\text{free surface}}} Q_d \sum_b u_b \boldsymbol{N}_b \cdot \boldsymbol{n}, \tag{2.17}$$

where F is a free surface mass matrix, and d and e are free surface node indices,

$$\mathrm{F}_{de} = \int_{\Gamma_{\text{free surface}}} \frac{\boldsymbol{n}\cdot\hat{\boldsymbol{r}}}{\Delta\rho g} Q_d Q_e. \tag{2.18}$$

It should be noted that this linear system, associated with matrix F can be easily solved, either with only a few iterations of a linear solver (used herein), or by lumping the matrix. Likewise, the actual free surface elevation η can be recovered from $\tilde{\eta}$ in an equally trivial Galerkin projection. In all results presented here, we use a piecewise quadratic representation for velocity $\boldsymbol{u}$ (P2) and a piecewise linear representation (P1) for pressure p' and free surface variable $\tilde{\eta}$. When the density is constant along the free surface (as is the case in all simulations examined herein), this implies that free surface elevation η is also piecewise linear.

Explicit method with non-linear iterations

As will be shown in the following sections, the explicit method is only first order accurate. Improved accuracy can be obtained when multiple iterations are performed per timestep. In each iteration, the linear system is updated and solved. Such iterations are typically used when non-linearity is introduced to the system by, for example, coupling to a temperature advection-diffusion equation (see Davies et al., 2011). In this chapter, such a method is used to update the free surface term $\underline{h}$.

Suppose in the first iteration we have obtained a new free surface value $\tilde{\eta}^*$. In a subsequent iteration we may then use:

$$\underline{h}_b = \int_{\Gamma_{\text{free surface}}} \boldsymbol{N}_b \cdot \boldsymbol{n} \sum_d Q_d \left((1-\theta)\tilde{\eta}_d^n + \theta\tilde{\eta}_d^*\right). \tag{2.19}$$

For $\theta = 0$ we maintain the same fully explicit method. As will be shown in the following

sections, setting $\theta = 1/2$ leads to a scheme that is second order accurate in time.

Implicit free surface

For an implicit treatment of the free surface, the free surface values $\tilde{\eta}_d$ are stored in a vector $\underline{\tilde{\eta}}$ and solved for in conjunction with $\underline{u}$ and $\underline{p}'$. The free surface integral term $\underline{h}$ is moved to the left-hand side of (2.14) and written in matrix form:

$$\underline{h} = \mathrm{H}\underline{\tilde{\eta}}, \text{ with } \mathrm{H}_{bd} = \int_{\Gamma_{\text{free surface}}} \boldsymbol{N}_b \cdot \boldsymbol{n} Q_d. \tag{2.20}$$

The same matrix H can be used to write the discretised kinematic boundary condition (2.17) as:

$$-\mathrm{H}^T\underline{u} + \mathrm{F}\frac{\underline{\tilde{\eta}}^{n+1} - \underline{\tilde{\eta}}^n}{\Delta t} = 0, \tag{2.21}$$

This leads to the combined system:

$$\begin{pmatrix} \mathrm{K} & \mathrm{G} & \mathrm{H} \\ \mathrm{G}^T & 0 & 0 \\ \mathrm{H}^T & 0 & -\Delta t^{-1}\mathrm{F} \end{pmatrix} \begin{pmatrix} \underline{u} \\ \underline{p}' \\ \underline{\tilde{\eta}}^{n+1} \end{pmatrix} = \begin{pmatrix} \underline{f} \\ 0 \\ -\Delta t^{-1}\mathrm{F}\underline{\tilde{\eta}}^n \end{pmatrix}. \tag{2.22}$$

Comparing (2.14) and (2.22) we may recognise that the same symmetric saddle point structure has been preserved, meaning that the usual solution methods are available for this linear system (see May et al., 2008, for an overview of preconditioned iterative methods for problems of this type). In effect, during the solution procedure, the vector of pressure degrees of freedom is extended with additional degrees of freedom along the free surface, and the pressure gradient matrix G is similarly extended to $\begin{pmatrix} G & H \end{pmatrix}$. Note that, as the extra degrees of freedom are only defined on the free surface, this requires minimal additional computational cost to solve the system.

We follow the same pressure correction approach, known as Schur Complement Reduction, as

outlined in Davies et al. (2011), but now based on the Schur complement:

$$\mathrm{S} = \begin{pmatrix} G^T \\ H^T \end{pmatrix} K^{-1} \begin{pmatrix} G & H \end{pmatrix} + \Delta t^{-1} \begin{pmatrix} 0 & 0 \\ 0 & \mathrm{F} \end{pmatrix}. \tag{2.23}$$

The same Schur complement matrix can be used in preconditioners for a fully coupled solution approach. Therefore the implicit free surface method may be implemented in a manner that is minimally invasive to solver strategies in existing geodynamical models.

Crank Nicolson time integration

In (2.22) only $\tilde{\underline{\eta}}$ carries a superscript n and $n+1$ to indicate the previous and current (to be solved for) time level. The solution of $\underline{u}$ and $\underline{p}'$, on the other hand, does not depend on previous timesteps. To make (2.21) a second order time integration however, $\underline{u}$ needs to be interpreted as the velocity at $t^{n+1/2}$. We will therefore indicate the velocity solved for in the current timestep with $\underline{u}^{n+1/2}$. To ensure second order temporal convergence of the whole system, the pressure and free surface need to be evaluated at the same time level $t^{n+1/2}$ in the discrete momentum equation, the first row of (2.22). Therefore, we also interpret the pressure solved for in the current timestep to be at this time level and write $\underline{p}' = \underline{p}'^{n+1/2}$. The free surface elevation used in the momentum equation is weighted between the beginning and end of timestep value: $(1-\theta)\tilde{\underline{\eta}}^n + \theta\tilde{\underline{\eta}}^{n+1}$. The system can now be rewritten, while maintaining the same symmetric form as before:

$$\begin{pmatrix} \mathrm{K} & \mathrm{G} & \theta\mathrm{H} \\ \mathrm{G}^T & 0 & 0 \\ \theta\mathrm{H}^T & 0 & -\theta\Delta t^{-1}\mathrm{F} \end{pmatrix} \begin{pmatrix} \underline{u}^{n+1/2} \\ \underline{p}'^{n+1/2} \\ \tilde{\underline{\eta}}^{n+1} \end{pmatrix} = \begin{pmatrix} \underline{f} - (1-\theta)\mathrm{H}\tilde{\underline{\eta}}^n \\ 0 \\ -\theta\Delta t^{-1}\mathrm{F}\tilde{\underline{\eta}}^n \end{pmatrix}. \tag{2.24}$$

In the following section we will show that for $\theta = 1/2$ (Crank Nicolson) we indeed obtain a second order accurate scheme, while for $\theta = 1$ we obtain a scheme that is first order accurate in time.

2.3 Analytical solutions

In this section, based on the appendix of Kramer et al. (2012), we work out the analytical solutions for benchmarks used in section 2.4.1. We follow the approach of Zhong et al., 1996 that combines approaches of Solomon et al., 1982 and Parsons et al., 1983. Similar analytical solutions are also provided in Ramberg, 1967.

We consider a domain in 2 dimensions, $0 \leq x \leq L$ and $-D \leq z \leq 0$, where D represents the depth of Earth's mantle. For a divergence free velocity field $\boldsymbol{u} = (u, w)$, we can find a stream function ψ such that:

$$u = -\frac{\partial \psi}{\partial z}, \quad w = \frac{\partial \psi}{\partial x}. \tag{2.25}$$

After substitution of this into the momentum equation of (2.1) and taking its curl, we obtain:

$$\frac{\partial^4 \psi}{\partial x^4} + 2\frac{\partial^4 \psi}{\partial x^2 \partial z^2} + \frac{\partial^4 \psi}{\partial z^4} = -\frac{\partial f}{\partial x}, \tag{2.26}$$

where $f = -\rho' g$ is the buoyancy term in the vertical momentum equation. A generic solution for the homogeneous case $f = 0$ that satisfies reflective boundary conditions at $x = 0$ and $x = L$ is given by:

$$\psi(x, z, t) = \sin(kx) \left(A(t) \sinh(kz) + B(t) \cosh(kz) + C(t) z \sinh(kz) + E(t) z \cosh(kz) \right), \tag{2.27}$$

with $k = 2\pi/\lambda$ where λ is an integer fraction of L.

Single free surface

In this case we consider a free surface condition at the top of the domain, $z = 0$, a free slip condition at the bottom, $z = -D$, and no buoyancy forcing ($f = 0$). An expression for the free surface that conforms to solution (2.27) is given by:

$$\eta^*(x, t) = F(t) \cos(kx). \tag{2.28}$$

The free slip condition (2.4) provides us with 2 equations, the no normal flow and the zero shear stress condition. The free surface condition (2.5) at the top provides 3 equations because in addition to the kinematic boundary condition and zero shear stress, it also enforces a no normal stress condition. More specifically, we consider the no normal stress condition (2.9) evaluated at $z = 0$. To evaluate this boundary condition however, we need to know what the pressure is. In order to avoid this problem, we take the x-derivative of the boundary condition; the x-derivative of the pressure can then be eliminated by substitution of the x-component of the momentum equation:

$$\begin{aligned} \left.\frac{\partial \sigma'_{zz}}{\partial x}\right|_{z=0} &= \left.\frac{\partial \tau_{zz}}{\partial x} - \frac{\partial p'}{\partial x}\right|_{z=0} = -g\rho \left.\frac{\partial \eta^*}{\partial x}\right|_{z=0}, \\ \left.\frac{\partial \tau_{zz}}{\partial x} - \frac{\partial \tau_{xx}}{\partial x} - \frac{\partial \tau_{zx}}{\partial z}\right|_{z=0} &= -g\rho \left.\frac{\partial \eta^*}{\partial x}\right|_{z=0}, \\ -2A(t)k^3\mu \sin(kx) &= \rho g F(t) k \sin(kx). \end{aligned} \tag{2.29}$$

These five equations form a linear system for the variables A, B, C, E and F which we can solve for. In particular, the kinematic boundary condition introduces a time derivative of F so that we obtain the simple ODE:

$$F(t) = -\tau \frac{dF(t)}{dt}, \tag{2.30}$$

where τ is the relaxation time:

$$\tau = \frac{Dk + \sinh(Dk)\cosh(Dk)}{\sinh^2(Dk)}\tau_0, \quad \tau_0 = \frac{2k\mu}{\rho g}. \tag{2.31}$$

Using the initial condition $F(0) = F_0$, the solution is given by:

$$\begin{aligned} F(t) &= F_0 e^{-t/\tau}, \\ A(t) = -\frac{F_0}{k\tau_0}e^{-t/\tau}, \quad B(t) &= -\frac{F_0}{k\tau}e^{-t/\tau}, \\ C(t) = \frac{F_0}{\tau}e^{-t/\tau}, \quad E(t) &= \frac{F_0}{\tau \tanh(Dk)}e^{-t/\tau}. \end{aligned} \tag{2.32}$$

Two free surfaces

In this case we also consider a free surface at the bottom of the domain, given by $z = -D + \zeta^*$:

$$\zeta^*(x,t) = G(t)\cos(kx). \tag{2.33}$$

In addition to replacing the no-normal flow condition at the bottom with the kinematic boundary condition, this introduces a sixth equation in the form of a no-normal-stress condition, which we express in the form of (2.10) using $\Delta\rho = \rho_\zeta - \rho_{\text{ext}}$ where ρ_{ext} represents the approximate density in the outer core. Note that this implies $\Delta\rho < 0$. Here, we use ρ_η and ρ_ζ for the densities at (the inside of) the top and bottom boundary respectively.

Again, the boundary condition forms a linear system of equations, which we can solve for A, B, C, E, F and G. The kinematic boundaries have introduced time derivatives of both F and G so that we obtain a 2 variable ODE:

$$\begin{pmatrix} F \\ G \end{pmatrix} = -\begin{pmatrix} \tau_\eta & -\gamma\tau_\eta \\ -\gamma\tau_\zeta & \tau_\zeta \end{pmatrix} \begin{pmatrix} \frac{\partial F}{\partial t} \\ \frac{\partial G}{\partial t} \end{pmatrix}, \tag{2.34}$$

where we use the following timescales τ_η and τ_ζ associated with the free surface at the top and bottom respectively, and a factor γ:

$$\begin{aligned} \tau_\eta &= \frac{Dk + \sinh(Dk)\cosh(Dk)}{\sinh^2(Dk)}\tau_{\eta,0}, \quad \tau_{\eta,0} = \frac{2k\mu}{\rho_\eta g}, \\ \tau_\zeta &= \frac{Dk + \sinh(Dk)\cosh(Dk)}{\sinh^2(Dk)}\tau_{\zeta,0}, \quad \tau_{\zeta,0} = \frac{2k\mu}{-\Delta\rho g}, \\ \gamma &= \frac{Dk\cosh(Dk) + \sinh(Dk)}{Dk + \sinh(Dk)\cosh(Dk)}. \end{aligned} \tag{2.35}$$

The eigenvalues of the ODE matrix gives two relaxation times:

$$\tau_\pm = \tfrac{1}{2}\left(\tau_\eta + \tau_\zeta\right) \pm \tfrac{1}{2}\sqrt{\left(\tau_\eta + \tau_\zeta\right)^2 - 4\left(1-\gamma^2\right)\tau_\eta\tau_\zeta}. \tag{2.36}$$

Note that $0 \leq \gamma \leq 1$ and that for $\lambda \ll D$, γ rapidly goes to zero, so that, as expected, the top and bottom free surface time scales become independent.

For initial conditions $F(0) = F_0$ and $G(0) = G_0$, we obtain:

$$\begin{aligned} F(t) &= \frac{F_0(\tau_\eta - \tau_-) - \gamma G_0 \tau_\eta}{\tau_+ - \tau_-} e^{-t/\tau_+} - \frac{F_0(\tau_\eta - \tau_+) - \gamma G_0 \tau_\eta}{\tau_+ - \tau_-} e^{-t/\tau_-}, \\ G(t) &= \frac{G_0(\tau_\zeta - \tau_-) - \gamma F_0 \tau_\zeta}{\tau_+ - \tau_-} e^{-t/\tau_+} - \frac{G_0(\tau_\zeta - \tau_+) - \gamma F_0 \tau_\zeta}{\tau_+ - \tau_-} e^{-t/\tau_-}, \\ A(t) &= -\frac{F(t)}{k\tau_{\eta,0}}, \quad B(t) = k^{-1}\frac{\partial F}{\partial t}, \quad C(t) = -\frac{\partial F}{\partial t}, \\ E(t) &= \frac{\frac{\partial G}{\partial t} - \cosh(Dk)\frac{\partial F}{\partial t}}{\sinh(Dk)}. \end{aligned} \tag{2.37}$$

Two free surfaces with density anomaly

This is the benchmark given in Zhong et al., 1996, where in addition to a bottom and top free surface, we now also consider a density anomaly $\rho' = -\alpha\rho_0 Q\cos(kx)\delta(z+d)$ at a depth $z = -d$ which gives a right-hand side term in the momentum equation:

$$f = \rho_0 g \alpha Q \cos(kx)\delta(z+d), \tag{2.38}$$

where Q represents the amplitude scaling of the temperature anomaly. The solution for this case is derived, following Zhong et al., 1996, by splitting the generic solution in two parts:

$$\psi(x,z,t) = \begin{cases} \sin(kx)(A_1(t)\sinh(kz) + B_1(t)\cosh(kz) + \\ \qquad C_1(t)z\sinh(kz) + E_1(t)z\cosh(kz)) & \text{if } -d < z < 0, \\ \sin(kx)(A_2(t)\sinh(kz) + B_2(t)\cosh(kz) + \\ \qquad C_2(t)z\sinh(kz) + E_2(t)z\cosh(kz)) & \text{if } -D < z < -d. \end{cases} \tag{2.39}$$

In addition to the six equations associated with the top and bottom free surface boundary condition, we need four further equations to solve for $A_1, B_1, C_1, E_1, A_2, B_2, C_2, E_2, F$ and G. Three of those are given by requiring continuity of the horizontal and vertical velocity, using (2.25), and continuity of shear stress:

$$\tau_{xz} = \mu\frac{\partial u}{\partial z} + \mu\frac{\partial w}{\partial x} = \mu\left(\frac{\partial^2}{\partial x^2} - \frac{\partial^2}{\partial z^2}\right)\psi = -\mu\left(k^2 + \frac{\partial^2}{\partial z^2}\right)\psi. \tag{2.40}$$

Continuity is therefore enforced through:

$$\lim_{z\uparrow -d}\psi = \lim_{z\downarrow -d}\psi, \qquad \lim_{z\uparrow -d}\frac{\partial\psi}{\partial z} = \lim_{z\downarrow -d}\frac{\partial\psi}{\partial z}, \qquad \lim_{z\uparrow -d}\frac{\partial^2\psi}{\partial z^2} = \lim_{z\downarrow -d}\frac{\partial^2\psi}{\partial z^2}. \tag{2.41}$$

Finally, a jump condition for the third derivative of ψ can be derived from:

$$\lim_{\epsilon\to 0}\int_{-d-\epsilon}^{-d+\epsilon}\frac{\partial^4\psi}{\partial x^4} + 2\frac{\partial^4\psi}{\partial x^2\partial z^2} + \frac{\partial^4\psi}{\partial z^4} = \lim_{\epsilon\to 0}\int_{-d-\epsilon}^{-d+\epsilon} -\frac{\partial f}{\partial x}, \tag{2.42}$$

$$\lim_{z\downarrow -d}\frac{\partial^3\psi}{\partial z^3} - \lim_{z\uparrow -d}\frac{\partial^3\psi}{\partial z^3} = \rho_0\alpha g Q k\sin(kx). \tag{2.43}$$

The solution of the ten-equation linear system again gives rise to an ODE in F and G.

$$\begin{pmatrix} F \\ G \end{pmatrix} = -\begin{pmatrix} \tau_\eta & -\gamma\tau_\eta \\ -\gamma\tau_\zeta & \tau_\zeta \end{pmatrix}\begin{pmatrix} \frac{\partial F}{\partial t} \\ \frac{\partial G}{\partial t} \end{pmatrix} + \begin{pmatrix} M \\ N \end{pmatrix}. \tag{2.44}$$

where the inhomogeneous part is given by:

$$M = \left(\frac{\alpha\rho_0 Q}{\rho_\eta}\right)\frac{-kD\sinh(kd) + kd\cosh(k(D-d))\sinh(kD) + \sinh(k(D-d))\sinh(kD)}{\sinh^2(kD)}, \tag{2.45}$$

$$N = \left(\frac{\alpha\rho_0 Q}{-\Delta\rho}\right)\frac{kD\sinh(kd)\cosh(kD) - kd\cosh(kd)\sinh(kD) + \sinh(kd)\sinh(kD)}{\sinh^2(kD)}. \tag{2.46}$$

When reaching a steady state, the time derivatives vanish and therefore the steady solution is given by $F(t\to\infty) = M$ and $G(t\to\infty) = N$. Note that the homogeneous part of the ODE is the same as in the previous case with no forcing. This means the solution for F and G is the same when considered as a deviation from the $t\to\infty$ steady state limit:

$$F(t) = \frac{(F_0 - M)(\tau_\eta - \tau_-) - \gamma(G_0 - N)\tau_\eta}{\tau_+ - \tau_-}e^{-t/\tau_+} - \frac{(F_0 - M)(\tau_\eta - \tau_+) - \gamma(G_0 - N)\tau_\eta}{\tau_+ - \tau_-}e^{-t/\tau_-} + M,$$

$$G(t) = \frac{(G_0 - N)(\tau_\zeta - \tau_-) - \gamma(F_0 - M)\tau_\zeta}{\tau_+ - \tau_-}e^{-t/\tau_+} - \frac{(G_0 - N)(\tau_\zeta - \tau_+) - \gamma(F_0 - M)\tau_\zeta}{\tau_+ - \tau_-}e^{-t/\tau_-} + N.$$

The coefficients for the solution of ψ are given by:

$$\begin{aligned}
A_1(t) &= -\frac{F(t)}{k\tau_{\eta,0}}, \quad B_1(t) = k^{-1}\frac{\partial F}{\partial t}, \quad C_1(t) = -\frac{\partial F}{\partial t}, \\
E_1(t) &= \frac{\frac{\partial G}{\partial t} - \cosh(Dk)\frac{\partial F}{\partial t} + \xi\sinh(k(D-d))}{\sinh(Dk)}, \\
A_2(t) &= \frac{-F(t)}{k\tau_{\eta,0}} + k^{-1}\xi\left(\cosh(kd) - kd\sinh(kd)\right), \\
B_2(t) &= k^{-1}\frac{\partial F}{\partial t} + k^{-1}\xi\left(\sinh(kd) - kd\cosh(kd)\right), \\
C_2(t) &= -\frac{\partial F}{\partial t} - \xi\sinh(kd), \\
E_2(t) &= \frac{\frac{\partial G}{\partial t} - \cosh(Dk)\frac{\partial F}{\partial t} - \xi\sinh(kd)\cosh(kD)}{\sinh(Dk)},
\end{aligned} \tag{2.47}$$

where ξ is given by:

$$\xi = \frac{\alpha Q \rho_0 g}{2k\mu}. \tag{2.48}$$

2.4 Test cases

In this section we present several comparisons between the explicit and implicit free surface methods. We first demonstrate the order of accuracy of each method in space and time by evaluating the error in the free surface calculation against known analytical solutions (described in the previous section 2.3). We also discuss the relative stability of the two methods for these cases. This is demonstrated further via a simulation of a lithospheric instability beneath a free surface, which with the explicit method at too large a timestep results in the so-called 'drunken sailor' instability.

2.4.1 Analytical comparison

We consider the idealised geometry, shown in Figure 2.1, of a two-dimensional box, $0 \leq x \leq L$, $-D \leq z \leq 0$. Boundary conditions are defined on the top, bottom, left and right boundaries and an additional internal boundary surface is defined to allow internal fluxes to be specified

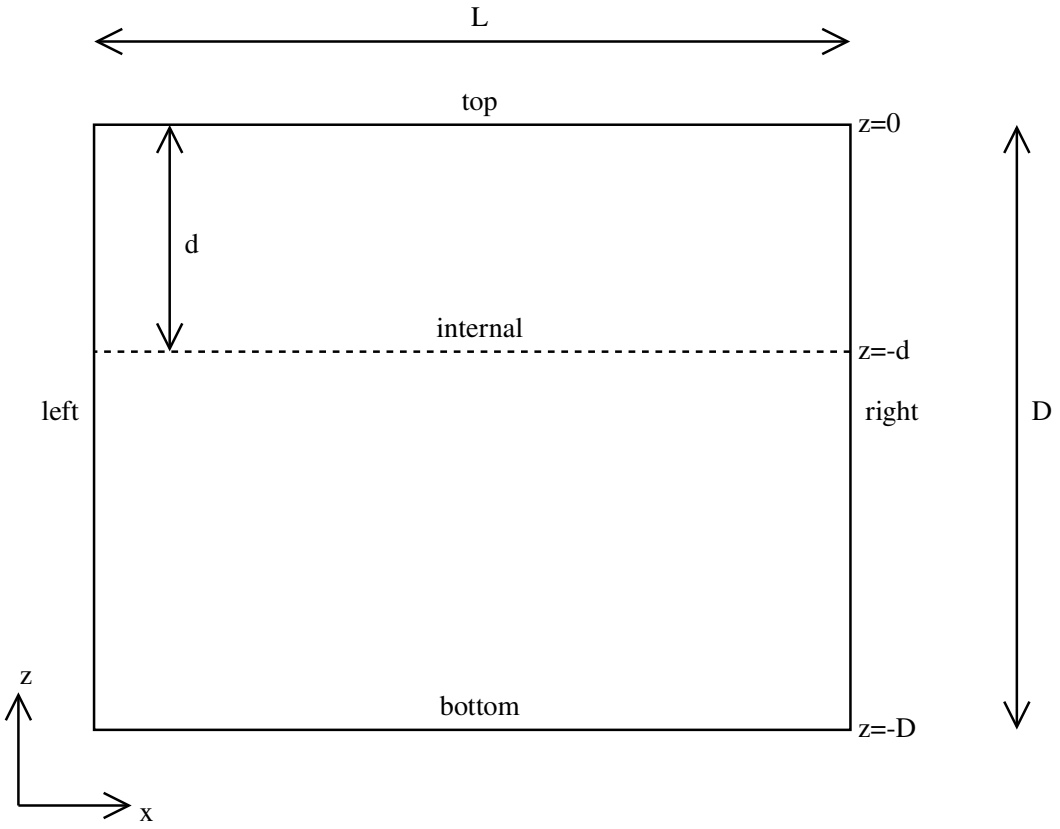


Figure 2.1: Illustration of the idealised two-dimensional domain used in the analytical test cases. Boundary conditions are applied at the top, bottom, left and right boundaries while the internal surface may be used to apply a density anomaly. z is taken as pointing upwards.

Mantle thickness	D	3×10^6	m
Viscosity	μ	1×10^{21}	Pa s
Gravitational acceleration	g	10	$\mathrm{m\,s^{-2}}$
Reference density	ρ_0	4500	$\mathrm{kg\,m^{-3}}$
Top external density	$\rho_{\mathrm{ext}}\vert_{z>0}$	0	$\mathrm{kg\,m^{-3}}$
Bottom external density	$\rho_{\mathrm{ext}}\vert_{z<-D}$	9000	$\mathrm{kg\,m^{-3}}$
Thermal expansivity	α	2×10^{-5}	$\mathrm{K^{-1}}$
Temperature anomaly scale	Q	1	K m

Table 2.1: Model parameters for the analytical free surface test cases.

in some cases. By varying the boundary and initial conditions, several test cases are produced which demonstrate advantages of the implicit method and deficiencies in its explicit counterpart.

Simulations are non-dimensionalised using the depth, D, as a length scale and a relaxation time as a timescale. D and other physical parameters are defined in Table 2.1. The relaxation timescale varies between simulations. For small scale features, where the wavelength of the topographic feature, $\lambda \ll D$, it is given by:

$$\tau_0 = \frac{2k\mu_0}{|\Delta\rho|g}, \tag{2.49}$$

where $k = 2\pi/\lambda$ is the wavenumber. For very large scale features, where λ is of the same order as D, the formulae for the exact relaxation timescales are presented in 2.3. We will demonstrate that the relaxation time is an important indicator for the stability criterion of the explicit method, whereas the stability of the implicit method appears independent of the chosen timestep.

Single free surface

In the first case, we consider a single free surface, $\eta(x,t)$, at the top, $z = 0$, of the domain. All other external boundaries have free slip conditions applied while no condition is applied at the internal boundary. The perturbation density, ρ', is zero throughout the simulation. However, an initial free surface is prescribed, given by:

$$\eta(x,0) = F_0 \cos(kx), \tag{2.50}$$

Wavelength, λ	Relaxation timescale, τ (kyr)	Approximate relaxation timescale (2.49), τ_0 (kyr)
$D/4$	11.81	11.81
$D/2$	5.90	5.90
D	2.95	2.95
$2D$	1.52	1.48
$4D$	1.02	0.74

Table 2.2: Relaxation timescales for a single free surface.

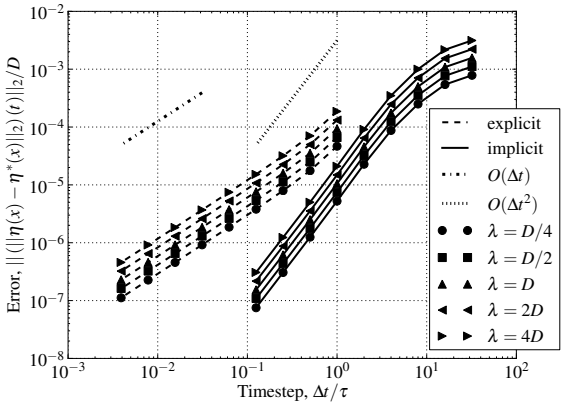
where $F_0 = 1 \times 10^3\,\mathrm{m}$ is the initial free surface amplitude. The simulation is run for $\lambda = D/4, D/2, D, 2D$ and $4D$ using both the explicit and implicit free surface methods. The relaxation timescale (used for non-dimensionalisation) for each wavelength considered is presented in Table 2.2 along with the approximate relaxation timescale, τ_0 (2.49), for comparison. In all cases, $L = \lambda$ and the mesh is made up of structured triangles with a vertical edge length, Δz, of $D/80$ and a horizontal edge length, Δx, of $L/80$.

For both the implicit and explicit cases nine different timestep sizes are considered. The explicit method is not stable beyond a timestep Δt larger than the relaxation time τ, so simulations are performed between limits of $\Delta t = \tau$ and $\Delta t = \tau/256$. All simulations attempted beyond a timestep of τ rapidly became unstably unbounded. The implicit case is not limited by timestep size, which we vary from 32τ to $\tau/8$.

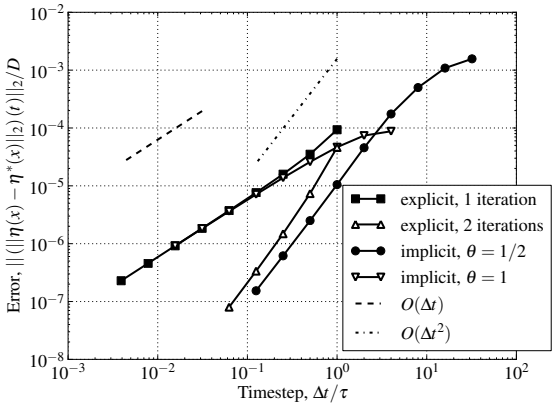
At each timestep of the simulation the error between the free surface elevation, η, and the analytical solution, η^* (see 2.3), is evaluated in a surface $L2$ norm on the top domain boundary (η^* is also treated as a piecewise linear function for this calculation). At the end of the simulation, these spatial errors are squared, weighted by the timestep, Δt, and summed into a discrete temporal $L2$ norm, which is then used to test the temporal order of convergence of both methods. In the implicit case this temporal norm is taken over 64 relaxation times (so the largest timestep calculation performs only two timesteps). Due to the small timesteps required, and the resulting long simulation times, the temporal error was evaluated over 4 relaxation times for the explicit method (four timesteps in the largest Δt case).

The results using a single iteration per timestep of the explicit method and $\theta = 1/2$ (see

(a) Temporal convergence



(b) Implicitness ($\lambda = D$)



(c) Solution

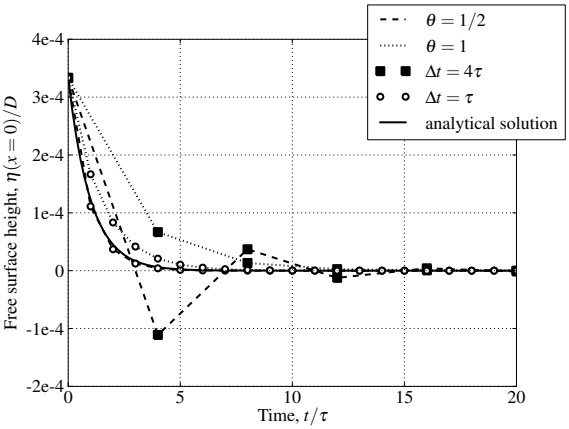


Figure 2.2: (a) Error between the numerical, η, and analytical, η^*, free surface elevations versus timestep size, Δt, for the case with a single free surface. The error is normalised by domain depth, D, and measured both across the top of the domain and through time using an $L2$ norm. The timestep is normalised by the free surface relaxation timescale, τ (see Table 2.2). The explicit method is first order while the implicit method is second order for a range of wavelengths (domain widths), λ. (b) Normalised error in the free surface elevation versus normalised timestep for a wavelength equal to the domain depth, $\lambda = D$. The explicit method from (a) can be made second order by taking two iterations per timestep while the implicit method becomes first order when the implicitness factor, θ, is set to one. In both (a) and (b) explicit simulations were run until $t = 4\tau$ while implicit simulations were run until $t = 64\tau$ before the temporal error was calculated. (c) The normalised free surface elevation at $x = 0$ versus normalised time using the implicit method with different timesteps and θs. The timesteps selected represent the cross-over in error in (b). At timesteps significantly larger than the relaxation time, $\theta = 1/2$ results in oscillatory behaviour and a smoother solution is achieved with $\theta = 1$. At a timestep equal to the relaxation time, $\theta = 1/2$ is almost indistinguishable from the analytical solution while with $\theta = 1$ a larger error is still clearly present. All numerical solutions were calculated with a normalised grid resolution, $\Delta x/L = \Delta z/D$, of 1/80.

equation (2.24)) for the implicit method are presented in Figure 2.2(a). These demonstrate that the implicit method is temporally second order accurate compared to the first order accuracy of the explicit method at a wide range of wavelengths. At the limit of stability for the explicit method, $\Delta t = \tau$, the same error can be achieved with the implicit method with a timestep twice as large. At the other end of the timestep range considered, the lowest errors achieved by the explicit method can be reproduced with the implicit method with a timestep 50 times larger.

The order of convergence of the explicit method may be improved to match the implicit method at the cost of an extra iteration per timestep if θ (see equation (2.19)) is set to 1/2, as shown in Figure 2.2(b). However, the absolute error of the implicit, $\theta = 1/2$, case is still lower and the iterated explicit method remains limited to $\Delta t \leq \tau$. The accuracy of the implicit method may also be reduced by selecting $\theta = 1$ (see equation (2.24)), which results in it becoming almost indistinguishable from the explicit method (see Figure 2.2(b)) at timesteps lower than the relaxation time.

Above a timestep of approximately three times the relaxation time the implicit, $\theta = 1/2$, method, though still stable and converging to the correct steady state, becomes oscillatory. This can be seen in Figure 2.2(c), where the free surface elevation, η is shown at $x = 0$ over 20 relaxation times. At this timestep, $\Delta t = 4\tau$, the method is effectively 'stepping over' the physics of the free surface. The oscillations may be damped out by selecting $\theta = 1$. In fact, at this timestep, the $\theta = 1$ case appears more accurate than with $\theta = 1/2$ (see Figure 2.2(b)), though this roll-over may be an artefact of the discrete temporal $L2$ norm used. Once the free surface evolution is resolved by the $\theta = 1/2$ implicit case it is clearly more accurate, being almost indistinguishable from the analytical solution in Figure 2.2(c) at $\Delta t = \tau$.

Two free surfaces

In the second analytical comparison we modify the single free surface set-up to include a free surface, $\zeta(x, t)$, at the bottom of the domain, $z = -D$, representing the core-mantle boundary.

Wavelength, λ	Relaxation timescales, τ_+ (kyr)	τ_- (kyr)	Approximate relaxation timescale (2.49), τ_0 (kyr)
$D/2$	5.90	5.90	5.90
D	3.03	2.87	2.95
$2D$	2.04	0.98	1.48
$4D$	1.89	0.15	0.74

Table 2.3: Relaxation timescales for two free surfaces.

This is initialised to:

$$\zeta(x, 0) = G_0 \cos(kx), \tag{2.51}$$

where $G_0 = 1 \times 10^3\,\mathrm{m}$ is the initial free surface amplitude. The simulation is run for $\lambda = D/2, D, 2D$ and $4D$ using both the explicit and implicit methods. The relaxation timescales for each wavelength considered are presented in Table 2.3 alongside the approximate relaxation timescale, τ_0 (2.49), for comparison. The minimum of the timescales, τ_-, is used for non-dimensionalisation.

Bounding the domain at the top and bottom by two free surfaces introduces a null space into the z component of velocity, w. We remove this by pinning w to zero at the stationary point $(x, z) = (L/4, -D/2)$. All other details of the simulation set-up remain the same as in the single free surface case.

Temporal convergence results for the top free surface η are presented in Figure 2.3 (results for the lower free surface ζ are identical). Again the errors in the explicit free surface method are evaluated over four minimum relaxation timescales. However, at the larger timesteps considered, simulations were also performed over a time period of $t = 64\tau_-$. These were found to be unstable when the timestep exceeded $\tau_-/8$ or $\tau_-/16$, depending on the wavelength. Simulations above these timesteps are excluded from the graph.

For the single free surface case, the largest stable timestep for the explicit method (as presented in Figure 2.2(a)) was found to be $\Delta t = \tau$ when run for the same, longer time, $t = 64\tau$. It therefore appears that having two free surfaces makes the explicit method more unstable. It may also be the case that the single free surface would exhibit instability at $\Delta t \leq \tau$ if the

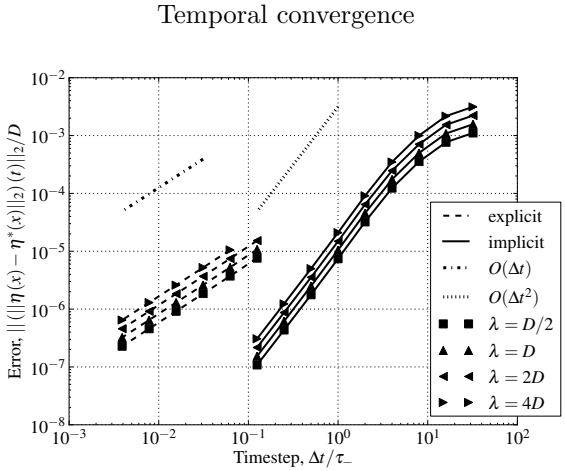


Figure 2.3: Error between the numerical, η, and analytical, η^*, free surface elevations versus timestep size, Δt, for the case with two free surfaces. The error is normalised by domain depth, D, and measured both across the top of the domain and through time using an $L2$ norm. The timestep is normalised by the minimum relaxation timescale, τ_- (see Table 2.3). The explicit method is first order accurate while the implicit method is second order accurate for a range of wavelengths (domain widths), λ. As both free surfaces are initialised with the same elevation the graph for the lower free surface is identical. All numerical solutions were calculated with a normalised grid resolution, $\Delta x/L = \Delta z/D$, of 1/80. Explicit simulations were run until $t = 4\tau_-$ while implicit simulations were run until $t = 64\tau_-$ before the temporal error was calculated.

simulations were run for even longer time periods. In figure 2.3 only the results for the explicit method with one iteration is displayed, but the same instability beyond $\Delta t \gtrsim \tau_-/16$ was observed when using two iterations.

As with the single free surface case, the implicit method for two free surface is seen to be stable across all timesteps considered and result in second order convergence. The apparently lower limit of stability for the explicit method means that, at its highest error, a timestep approximately 10 times larger may be taken with the implicit method, while, at its lowest error, the ratio is still about 50 across a range of wavelengths.

Two free surfaces with density anomaly

The final analytical comparison was proposed by Zhong et al. (1996). This keeps the top and bottom free surfaces from the previous case but with initial amplitudes of $F_0 = 0$ and $G_0 = 0$ respectively. In addition, a buoyancy anomaly is introduced such that:

$$\rho' g = -\rho_0 \alpha \Delta T g, \tag{2.52}$$

where g, ρ_0 and α are the gravity magnitude, reference density and thermal expansivity respectively (see Table 2.1) and ΔT is a temperature anomaly:

$$\Delta T = Q\cos(kx)\delta(z+d), \tag{2.53}$$

where Q is a scaling parameter (see Table 2.1) and $\delta(z+d)$ is a Dirac delta function located at depth, d. Once integrated with respect to z we introduce this buoyancy as a weakly imposed vertical momentum flux over the internal surface indicated in Figure 2.1. The vertical velocity is also pinned to zero at the stationary point $(x, z) = (L/4, -d)$ to remove the null space.

The buoyancy anomaly establishes convection within the domain and drives the free surfaces towards a non-zero amplitude steady state. Two anomaly depths, $d = D/2$ and $d = D/4$, are considered at a wavelength of $\lambda = D$ between timesteps of $32\tau_-$ and $\tau_-/8$ in the implicit case and τ_- and $\tau_-/128$ in the explicit case. As was the case without a buoyancy anomaly, simulations with $\Delta t \gtrsim \tau_-/16$ were found to be unstable with the explicit method. The relaxation timescales are identical to the case with no buoyancy and are given in Table 2.3 for $\lambda = D$.

Temporal convergence results are presented in Figure 2.4(a) and again demonstrate second order convergence for the implicit method versus first order for the explicit case with the same number of iterations per timestep (one). Solution accuracy is illustrated in Figure 2.4(b) where η and ζ are plotted at $x = 0$ for five minimum relaxation timescales. The solution for $\Delta t = \tau_-/4$ is indistinguishable from the analytical solution (see section 2.3) and yet was run with a timestep four times larger than possible with the explicit method and achieves an error over five times lower (see Figure 2.4(a)).

All results presented in Figure 2.4 were performed on a structured triangular mesh with a vertical edge length, Δz, of $D/160$ and a horizontal edge length, Δx, of $L/160$. The increased resolution relative to the previous cases was found to be necessary as erroneous temporal convergence occurred at lower resolutions for both methods (see Figure 2.5(a)). This is due to the high solution gradients induced by the buoyancy anomaly delta function within the domain. As illustrated in Figure 2.5(b), for the $d = D/2$ case, the pressure solution is highly

(a) Temporal convergence (b) Solution

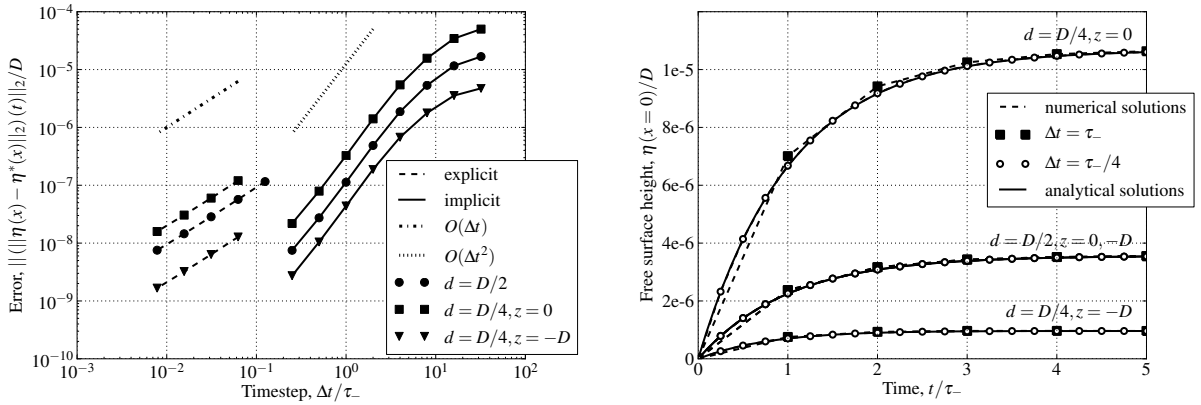


Figure 2.4: (a) Error between the numerical, η (or ζ for $z=-D$), and analytical, η^* (or ζ^* for $z=-D$), free surface elevations versus timestep size, Δt, for the case with two free surfaces and a density anomaly. The error is normalised by domain depth, D, and measured both across the domain boundary and through time using an $L2$ norm. The timestep is normalised by the minimum relaxation timescale, τ_- (see Table 2.3). The explicit method is first order while the implicit method is second order for a range of density anomaly depths, d, and for the upper, $z=0$, and lower, $z=-D$, free surfaces. For the $d=D/2$ case the top and bottom errors are identical. Explicit simulations were run until $t=4\tau_-$ while implicit simulations were run until $t=64\tau_-$ before the temporal error was calculated. (b) The normalised free surface elevation at $x=0$ ($\eta(x=0)/D$ for $z=0$, $\zeta(x=0)/D$ for $z=-D$) versus normalised time using the implicit method with different timesteps and anomaly depths, d. All numerical results were calculated using a normalised grid spacing, $\Delta x/L=\Delta z/D$, of $1/160$.

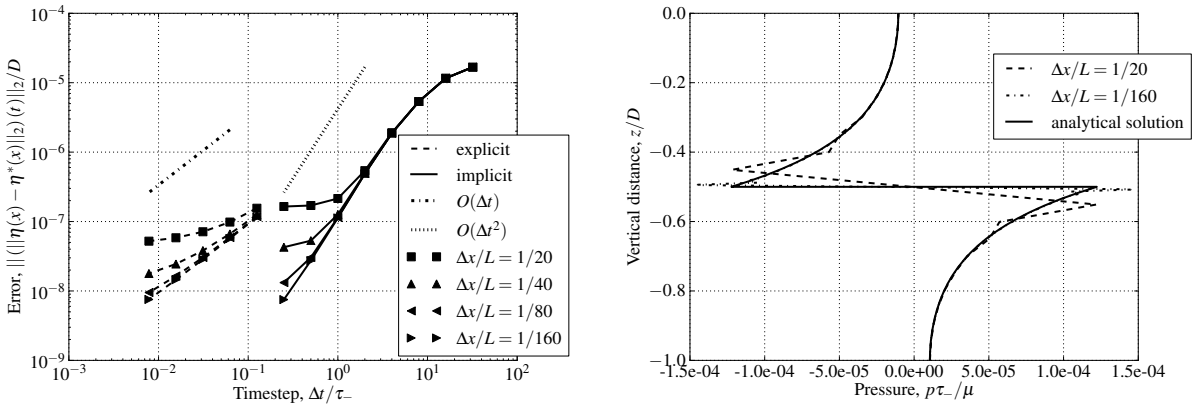
discontinuous and, at lower resolutions, e.g. $\Delta x/L=\Delta z/D=1/20$, is poorly represented causing, with decreasing timesteps, convergence to an incorrect solution.

Finally, we test the spatial convergence of both methods by timestepping to a steady state, within a tolerance of 10^{-10}, and evaluating the free surface error in an $L2$ norm over the top and bottom of the domain. Here the implicit method takes timesteps of $100\tau_-$ while the explicit method is limited by stability to $\Delta t=\tau_-/16$. As the free surface in both cases is piecewise linear in space, both are seen to achieve second order spatial accuracy, as shown in Figure 2.5(c) for η with $d=D/2$.

All three analytical cases demonstrate that, when configured with $\theta=1/2$, the implicit method achieves a higher order of convergence than the explicit method with a single solve per timestep. While the explicit method's accuracy may be improved by increasing the number of iterations, and doubling the solver cost, per timestep, its stability is severely limited by the timestep size, which is not the case with the implicit method. We proceed to investigate the stability

(a) Temporal convergence for different spatial resolutions

(b) Pressure solution ($x = \lambda/2$, $d = D/2$)



(c) Spatial convergence ($d = D/2$)

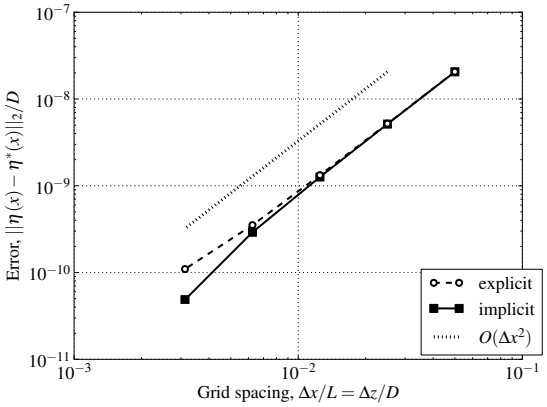


Figure 2.5: (a) Error between the numerical, η, and analytical, η^*, free surface elevations versus timestep for the explicit and implicit methods at a range of spatial resolutions in the case with two free surfaces and a density anomaly. The meshes were refined in both horizontal and vertical direction, such that in all cases $\Delta x/L = \Delta z/D$. The error is normalised by domain depth, D, and measured both across the top of the domain and through time using an $L2$ norm. The timestep is normalised by the minimum relaxation timescale, τ_- (see Table 2.3). High spatial resolution is necessary to ensure convergence to the correct analytical solution. Explicit simulations were run until $t = 4\tau_-$ while implicit simulations were run until $t = 64\tau_-$ before the temporal error was calculated. (b) A profile through the pressure solution at $x = \lambda/2$ demonstrating the presence of a sharp discontinuity around the density anomaly, which must be adequately resolved. Numerical solutions are shown at two spatial resolutions after a time, t, of $64\tau_-$. The analytical solution is at a steady state. (c) Normalised spatial error in the free surface elevation versus normalised grid spacing after the simulation has reached a steady state. Both implicit and explicit methods achieve second order accuracy using piecewise linear finite elements for pressure and the free surface and piecewise quadratic elements for velocity. All results were calculated using an anomaly depth, d, of half the domain depth, $D/2$, and a wavelength equal to the domain depth, $\lambda = D$.

properties of both methods further with a geophysically motivated example, the case of a lithospheric instability beneath a free surface.

2.4.2 Rayleigh-Taylor instability: 'drunken sailor'

In this section we simulate the Rayleigh-Taylor instability proposed by Kaus et al. (2010). A square two-dimensional domain, $-2.5 \times 10^5\,\mathrm{m} \leq x \leq 2.5 \times 10^5\,\mathrm{m}$, $-5 \times 10^5\,\mathrm{m} \leq z \leq 0\,\mathrm{m}$, is considered with free slip velocity boundary conditions at the sides, a no slip boundary condition at the base and a free surface boundary condition at the top. Inside the domain, a dense material of higher viscosity ($\rho_1 = 3300\,\mathrm{kg\,m^{-3}}$, $\mu_1 = 1 \times 10^{21}\,\mathrm{Pa\,s}$) is initially above a material of lower density and viscosity ($\rho_1 = 3200\,\mathrm{kg\,m^{-3}}$, $\mu_2 = 1 \times 10^{20}\,\mathrm{Pa\,s}$). The materials are separated by a sharp material boundary, which is initially at a depth of $1 \times 10^5\,\mathrm{m}$ with a sinusoidal perturbation, $5 \times 10^3\,\mathrm{m}$ in amplitude:

$$z = -1 \times 10^5\,\mathrm{m} + 5 \times 10^3\,\mathrm{m} \cos\left(\frac{2\pi x}{5 \times 10^5\,\mathrm{m}}\right). \tag{2.54}$$

Over time this unstable stratification produces two dense drips of material that flow down the sides of the domain. The free surface, initialised with no topography, responds to the internal deformation by warping down above the drips and up in the centre of the domain.

The locations of the different materials are indicated by a volume fraction, ϕ, which is equal to one in the dense upper material and zero in the lower material. The density and viscosity are then given by:

$$\rho = \rho_1\phi + \rho_2(1-\phi), \tag{2.55}$$

$$\mu = \mu_1\phi + \mu_2(1-\phi). \tag{2.56}$$

Taking the hydrostatic reference density as that of the dense upper material bordering the free surface, $\rho_0 = \rho_1$, the perturbation density is given by:

$$\rho' = (\rho_2 - \rho_1)(1-\phi). \tag{2.57}$$

The volume fraction, ϕ, is advected using a linear advection equation:

$$\frac{\partial \phi}{\partial t} + \boldsymbol{u} \cdot \nabla \phi = 0, \tag{2.58}$$

which is discretised in space on a dual mesh using a finite volume flux-limited scheme (HyperC, Leonard, 1991; Wilson, 2009). The control volumes of the dual mesh are defined around the P2 nodes of the finite element mesh. Advection is treated explicitly in time and subcycled to ensure a maximum Courant number, C, of 1/4.

This case is used to examine the relative stabilities of the explicit and implicit free surface methods over a time period of $t = 6\,\mathrm{Myr}$. In the explicit case the timestep size, Δt, is defined at the start of the simulation and held constant for its duration. In the implicit case a target advective Courant number, C, is set on the dual mesh. The timestep is then automatically adjusted, based on the velocity of the previous timestep, $\boldsymbol{u}^n$, in an attempt to ensure that the target Courant number is maintained. This process is restricted to ensure that large jumps in the timestep do not occur at the start of the simulation when the velocity is initially zero. Iterations between the velocity/pressure/free surface and volume fraction solution steps are used to converge the non-linearity in the coupled system. The domain is discretised using a structured triangular mesh with equal $5 \times 10^3\,\mathrm{m}$ vertical and horizontal edge lengths.

Figure 2.6: Simulations of a Rayleigh-Taylor instability, in a square domain $-2.5 \times 10^5\,\mathrm{m} \leq x \leq 2.5 \times 10^5\,\mathrm{m}$, $-5 \times 10^5\,\mathrm{m} \leq z \leq 0\,\mathrm{m}$, where comparatively dense, viscous material (dark grey) sinks through less dense material of lower viscosity (light grey - see text for further details). (a) An explicit free surface simulation at a constant timestep, Δt, of 2000 years, in which the simulation evolves smoothly. (b) An implicit free surface simulation, at a Courant number, C, of approximately 5. Although the implicit simulation evolves at substantially larger timesteps than the explicit case (see Figure 2.8(a)), the results remain consistent.

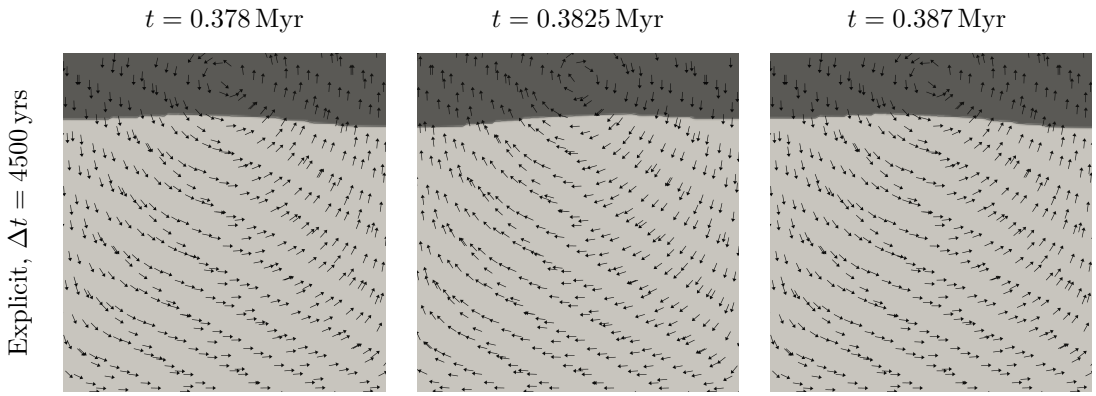
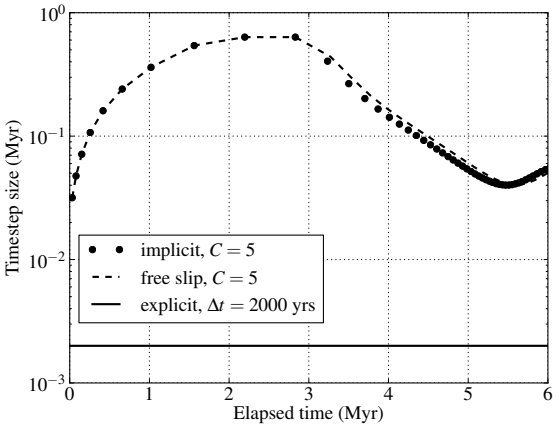


Figure 2.7: Simulations of a Rayleigh-Taylor instability, in a square domain $-2.5 \times 10^5\,\mathrm{m} \leq x \leq 2.5 \times 10^5\,\mathrm{m}$, $-5 \times 10^5\,\mathrm{m} \leq z \leq 0\,\mathrm{m}$, where comparatively dense, viscous material (dark grey) sinks through less dense material of lower viscosity (light grey - see text for further details). An explicit free surface simulation at a constant timestep, Δt, of 4500 years, in which a sloshing instability develops, where the velocity oscillates between consecutive timesteps.

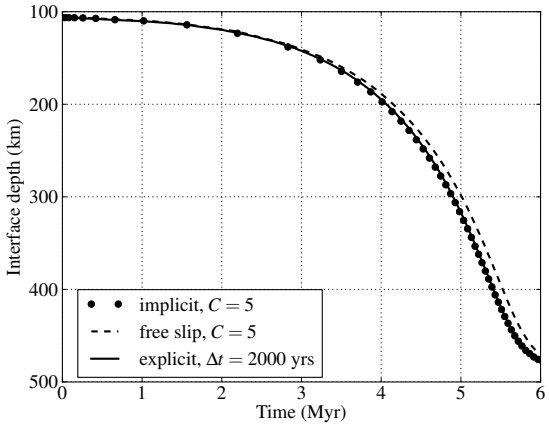
Simulations employing an explicit free surface treatment with one non-linear iteration were found to be stable at $\Delta t \leq 4000$ years. At these timesteps the topography amplitude increases gradually, but decays towards the end of the simulation, as high density material reaches the base of the domain and the velocity decreases again (see Figures 2.6(a) and 2.8). However, at larger timesteps a sloshing instability occurs, where the velocity field oscillates between consecutive timesteps, eventually becoming physically unbounded (see Figure 2.7). These results are consistent with those of Kaus et al. (2010). When two non-linear iterations are used, the explicit method is unstable with $\Delta t > 2000$ years. Since we would hope that the solution would converge with non-linear iterations, the explicit free surface treatment is considered unstable at $\Delta t > 2000$ years, which is substantially less than the estimated free surface relaxation time of approximately 25000 years for this problem (based on equation (2.49)).

The implicit free surface treatment, by contrast, remains stable at significantly larger timesteps and with an increasing number of non-linear iterations (five are used in the implicit results discussed below). Although the timestep size varies substantially throughout the simulation (see Figure 2.8(a)), it is consistently at least an order of magnitude greater than that of the stable explicit case ($\Delta t = 2000$ years), varying between $\Delta t \approx 25000$ years and $\Delta t \approx 600000$ years (targeting a Courant number, C, of 5). Nonetheless, solution accuracy is maintained at these larger timesteps, as demonstrated by a comparison of the material interface and free surface

(a) Timestep size



(b) Material interface depth



(c) Free surface height

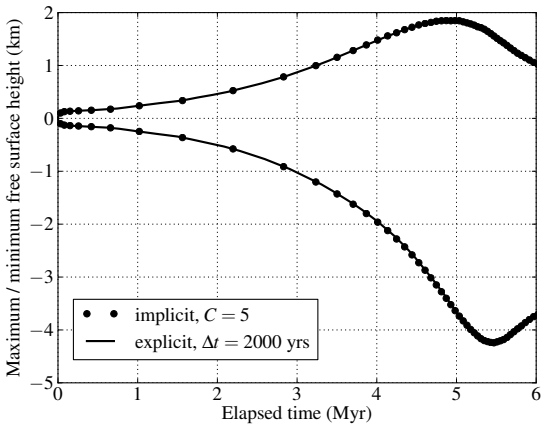


Figure 2.8: A series of comparisons between explicit ($\Delta t = 2000$ years) and implicit (Courant number, $C = 5$) free surface simulations of a Rayleigh Taylor instability in a square domain $-5 \times 10^5\,\mathrm{m} \leq z \leq 0\,\mathrm{m}$ (see Figure 2.6). (a) Timestep size, Δt, versus time – note the logarithmic scale. (b) Depth of the material interface at $x = -2.5 \times 10^5$ m; (c) Maximum and minimum free surface height. For comparison, the results from a simulation with a free slip boundary condition on the top of the domain are shown. This targets the same Courant number as the simulation with an implicit free surface. Note that the implicit free surface simulation remains stable at substantially larger timesteps than the explicit simulation, while results remain consistent. It also evolves at timesteps similar to the free slip case.

evolution to the stable explicit simulation (see Figure 2.8(b, c)). It should be noted that the implicit free surface simulation evolves at similar timesteps to a simulation with a free slip top boundary condition targeting the same Courant number (Figure 2.8(a)). Indeed, the computational requirements of both cases are very similar, with the implicit free surface simulation taking only a factor of 1.04 greater wall-time than the free slip case. On the other hand, the explicit free surface simulation, running at timesteps that are a fraction of those of the free slip case and with fewer non-linear iterations, took a factor of 21.96 greater wall-time.

2.5 Preliminary Conclusions

Here we discuss the conclusions based on the analysis in the previous sections, as it appeared in Kramer et al. (2012). These will be further refined in the sections that follow.

We have presented a new algorithm for simulating a free surface in geodynamical models. The method couples the equation for the evolution of free surface elevation to the Stokes system of velocity and pressure, using implicit time integration. It is straightforward to implement, does not complicate the solution procedure and requires similar computation per timestep as a standard free slip case. The implicit time integration allows simulations to evolve at much larger time steps when compared to previous explicit free surface methods. Moreover, the method is second order accurate in time, meaning that the same level of accuracy is achieved even at these larger timesteps. The method therefore substantially reduces the computational cost of free surface simulations.

We have demonstrated these benefits by comparing model predictions to a number of analytical cases. These clearly show that although accurate, the explicit method is bound by timesteps that can be an order of magnitude smaller than the relaxation time for the problem under examination. Such small timestep constraints would render free surface simulations prohibitively expensive for large scale geodynamical models. Conversely, the new implicit method remains stable at much larger timesteps, while producing the same accurate solutions. We have also demonstrated that for a well known Rayleigh-Taylor benchmark case, the drunken sailor insta-

bility, reported in Kaus et al., 2010 and reproduced here with the explicit method, does not occur with the implicit free surface treatment. Again for this case, we show that the implicit method remains accurate at larger timesteps, leading to a dramatic reduction in computational cost when compared to the explicit case.

It should be noted that although the implicit method remains stable at timesteps that are orders of magnitude larger than the relaxation time of the problem under examination, the relaxation of these large scale features would clearly not be resolved with such timesteps. In such cases, the large scale response of the free surface to changes in the interior would be immediate, leading to similar predictions of free surface elevation as those computed from a free slip calculation. However the relaxation time for smaller scale features in the topography may be much larger. Accurately resolving the response time of such features is only possible with a true free surface and it is therefore essential when these smaller scale features are embedded in a large scale model to apply a free surface method that remains stable in such conditions.

2.6 Further Developments

In this section we discuss a number of publications on the topic of free surface methods for geodynamical models since Kramer et al. (2012). We discuss a number of publications and approaches that have appeared since then, and in particular we discuss how the stabilisation method of Kaus et al. (2010), which was introduced for models with a Lagrangian mesh moving with the free surface, can be reinterpreted in an Eulerian framework, as a semi-implicit time-integration scheme for the free surface which is closely related to the implicit scheme analysed in more detail in this chapter.

Simultaneously with Kramer et al. (2012), an overview paper by Crameri et al., 2012 appeared that evaluates the popular sticky air approach, in which the free surface is modelled through an additional low-viscosity layer on top representing air with the free surface being the interface between the air and the high-viscosity mantle material below. They compare six different numerical codes and in particular discuss some of the limitations of the sticky air approach

compared with Lagrangian approaches in which the mesh is deformed to move with the free surface. All methods discussed do require additional stabilisation to deal with larger time steps.

2.6.1 Stabilisation Method of Kaus

As mentioned in previous sections, Kaus et al. (2010) introduce a free surface stabilisation term that also deals with the instability discussed in this chapter. It is derived for models in a Lagrangian frame in which the free surface moves with the velocity at the surface, but this movement only happens at the end of each timestep, and thus changes in vertical velocity do not immediately feed back in terms of a different load felt at the top and the associated change in hydrostatic pressure. In Andrés-Martínez et al. (2015) this method is extended to also take into account horizontal movement at the surface, which for a sloped free surface also induces a change in free surface elevation. Here, we will briefly show that the same stabilisation terms can also be used in an Eulerian framework and be interpreted as an alternative implicit time integration scheme for the free surface.

We split the movement of the free surface (2.15) in a horizontal part and vertical part. For this we use an auxiliary scalar function $z - \eta$, where z is just a general vertical coordinate that measures the (negative) depth below the equilibrium free surface at $z = 0$, and is not necessarily aligned with any of the coordinate axes, and in spherical or cylindrical shell domains (see next chapter) with equilibrium free surface at $r = R_T$ we simply use $z = r - R_T$. In this context the free surface elevation η is a function of all coordinates, but simply constant in the vertical direction. Thus $z - \eta$ is the vertical distance to the free surface everywhere in the domain, which is 0 for all points at the free surface boundary, i.e. the free surface is its 0-contour, and the normal $\boldsymbol{n}$ to the free surface can be written as a multiple of

$$\nabla (z - \eta) = \hat{\boldsymbol{r}} - \nabla \eta \tag{2.59}$$

where $\nabla\eta$ is a horizontal vector, i.e. $\hat{\boldsymbol{r}} \cdot \nabla\eta = 0$. Using this we can rewrite (2.15) to

$$\eta^{n+1} - \eta^n = \Delta t \frac{\boldsymbol{n} \cdot \boldsymbol{u}}{\boldsymbol{n} \cdot \hat{\boldsymbol{r}}} = \Delta t \frac{(\hat{\boldsymbol{r}} - \nabla\eta) \cdot \boldsymbol{u}}{(\hat{\boldsymbol{r}} - \nabla\eta) \cdot \hat{\boldsymbol{r}}} = \Delta t \left(\hat{\boldsymbol{r}} \cdot \boldsymbol{u} - \nabla\eta \cdot \boldsymbol{u}\right). \tag{2.60}$$

This change in free surface during a timestep leads to a change in hydrostatic pressure (assuming a density difference $\Delta\rho$):

$$\Delta\rho\ g \left(\eta^{n+1} - \eta^n\right) = \Delta\rho\ g \Delta t\ \alpha \left(\hat{\boldsymbol{r}} \cdot \boldsymbol{u} - \beta \nabla\eta \cdot \boldsymbol{u}\right), \tag{2.61}$$

where $0 \leq \alpha, \beta \leq 1$ are coefficients introduced in Andrés-Martínez et al. (2015) to weigh the two terms separately. β scales the contribution of the horizontal movement, thus with $\beta = 0$ we retrieve the same as in Kaus et al. (2010), where α corresponds to the Θ-coefficient in Kaus et al. (2010).

In Kaus et al. (2010) and Andrés-Martínez et al. (2015) this change in pressure is simply added as an additional surface forcing term to compensate for the lagging Lagrangian movement of the free surface. In fact Kaus et al. (2010) includes the more general case of different density layers in the interior of the domain whose movement with the mesh and its effect on pressure is not immediately updated, causing the same instability as the free surface instability described in this chapter, be it that the instability is scaled by $\Delta\rho$ and thus the interior instability is generally a lot less restrictive for the time step than the one at the free surface. Nonetheless Kaus et al. (2010) applies the additional stabilisation term at all vertical grid layers, where by construction it vanishes if $\Delta\rho = 0$.

In both papers the stabilisation is achieved by making the term(s) dependent on the velocity $\boldsymbol{u}$ that we are solving for, and thus they are added to the left-hand side of the equation, added into the K-matrix. We can show however that their stabilisation term can also be interpreted in an Eulerian frame, in which we impose (2.9), through time-integration of the corresponding term

$$\int_{\Gamma_{\text{free surface}}} \boldsymbol{N} \cdot \boldsymbol{n} \Delta\rho g \eta \tag{2.62}$$

on the left-hand side of (2.12) using a value of $\eta = \eta^n + \alpha(\eta^{n+1} - \eta^n)$. Instead of introducing an

independent variable η^{n+1} to be solved for, as we did in our implicit method in section 2.2.2, we substitute (2.60) and end up with the following system (cf. (2.14)):

$$\begin{pmatrix} \mathrm{K} + \mathrm{S}^{\mathrm{Kaus}} & \mathrm{G} \\ \mathrm{G}^T & 0 \end{pmatrix} \begin{pmatrix} \underline{u} \\ \underline{p}' \end{pmatrix} = \begin{pmatrix} \underline{f} - \underline{h} \\ 0 \end{pmatrix}, \tag{2.63}$$

in which the explicit part of the boundary integral is the same $\underline{h}$ as in (2.14), and the implicit, $\boldsymbol{u}$-dependent part is expressed using the stabilisation matrix

$$\mathrm{S}^{\mathrm{Kaus}}{}_{bc} = \int_{\Gamma_{\text{free surface}}} \frac{\alpha \Delta \rho g}{\boldsymbol{n} \cdot \hat{\boldsymbol{r}}} \boldsymbol{N}_b \cdot \boldsymbol{n} \, \boldsymbol{n} \cdot \boldsymbol{N}_c \tag{2.64}$$

such that we get a stabilisation term of the form:

$$\mathrm{S}^{\mathrm{Kaus}} \underline{u} = \int_{\Gamma_{\text{free surface}}} \frac{\alpha \Delta \rho g}{\boldsymbol{n} \cdot \hat{\boldsymbol{r}}} \boldsymbol{N}_b \cdot \boldsymbol{n} \, \boldsymbol{n} \cdot \boldsymbol{u} \tag{2.65}$$

$$= \int_{\Gamma_{\text{free surface}}} \alpha \Delta \rho g \boldsymbol{N}_b \cdot \boldsymbol{n} \left(\hat{\boldsymbol{r}} \cdot \boldsymbol{u} - \beta \nabla \eta \cdot \boldsymbol{u} \right). \tag{2.66}$$

In Andrés-Martínez et al., 2015 it is remarked that the stabilisation matrix becomes asymmetric for $\beta \geq 0$, which is detrimental for most solution strategies for the system. This asymmetry is ultimately due to an inconsistent choice of normal vectors $\boldsymbol{n}$. They assume 2D Cartesian coordinates with y being the vertical, and only apply the stabilisation term as a force in the y direction. This corresponds to assuming $\boldsymbol{n}$ in (2.66) being in the same vertical y-direction, i.e. assuming $\boldsymbol{n} = \hat{\boldsymbol{r}} = \hat{y}$. This leads to the second term in (2.66), where $\nabla \eta$ is always in the x-direction being asymmetric. From (2.65) it becomes clear however that as long as the actual free surface normal $\boldsymbol{n}$ is used, the stabilisation term is not purely in the vertical direction, but does remain symmetric. This makes intuitive sense as the compensating force should in fact be the missing force normal to the free surface.

Andrés-Martínez et al. (2015) show that for stability the β-term is only required for very steep slopes (more than 30 degrees). If the β-term is omitted, it does make more sense to only consider the vertical component of the stabilisation term, i.e. use $\boldsymbol{n} = \hat{\boldsymbol{r}} = \hat{y}$ in the first term of (2.66). In an Eulerian framework this has the advantage that the additional matrix $\mathrm{S}^{\mathrm{Kaus}}$

becomes independent of changes in the free surface, and only needs assembling once.

Andrés-Martínez et al. (2015) observe that for some cases they obtain the most accurate answers using $\alpha = \frac{2}{3}$ which they relate to $\frac{1}{3}, \frac{2}{3}$-weighting obtained in a finite-element-like time integration, see equation (30) in Andrés-Martínez et al. (2015), but it remains unclear why this weighting would not then also apply to all other terms, and in fact what time-integration they have used for the Lagrangian movement. In the Eulerian frame described here we expect $\alpha = \frac{1}{2}$ to be most accurate. Optimal convergence, possibly at second order, may only be possible if care is taken to consider what time levels the velocities and pressures are considered at (as we did in section 2.2.2), and be consistent with the update of the free surface (2.15).

A strong form variant of the stabilisation term of Kaus et al. (2010) suitable for finite difference discretisations is presented in Duretz et al. (2011). Although they do investigate the influence of the stabilisation terms on the spatial accuracy, showing it does not affect the convergence with Δx, they do not investigate temporal convergence as we have in this chapter.

2.6.2 Eliminating the Free Surface Degrees of Freedom

Regardless of the question of accuracy, the stabilisation method does have the advantage that it does not require an additional set of degrees of freedom to be solved for, in the form of free surface elevations. This simplifies its implementation. An advantage of the implicit method advocated in this chapter, section 2.2.2, is that it leaves the structure of the inner solve in the form of the K matrix unchanged. If the stabilisation can be kept symmetric however, the addition of $\mathrm{H}^{\mathrm{Kauss}}$ may in fact be beneficial for solver convergence.

The additional free surface degrees of freedom of the implicit method in section 2.2.2 can however be eliminated through a Schur complement reduction on the F block in (2.24). Using the bottom row of that system (corresponding to (2.21)), we can express

$$\underline{\tilde{\eta}}^{n+1} = \underline{\tilde{\eta}}^{n} + \Delta t F^{-1} H^T \underline{u}^{n+1/2} \tag{2.67}$$

which we can substitute in the top row, thus eliminating $\tilde{\underline{\eta}}^{n+1}$:

$$\begin{pmatrix} \mathrm{K} + \Delta t\theta\ \mathrm{H}\mathrm{F}^{-1}\mathrm{H}^T & \mathrm{G} \\ \mathrm{G}^T & 0 \end{pmatrix} \begin{pmatrix} \underline{u}^{n+1/2} \\ \underline{p}'^{n+1/2} \end{pmatrix} = \begin{pmatrix} \underline{f} - \mathrm{H}\tilde{\underline{\eta}}^n \\ 0 \end{pmatrix} \tag{2.68}$$

Note that in the general case F^{-1} is a dense matrix, so this doesn't immediately suggest a practical method. One could however implement it with iterative solvers with a relatively cheap inner solve for F^{-1}, which would be an additional nested inner loop inside the inversion of $\mathrm{K} + \Delta t\theta\ \mathrm{H}^T\mathrm{F}^{-1}\mathrm{H}$ which in turn forms an inner loop inside the Schur complement solve of the combined $\underline{u}, \underline{p}'$ system.

Note however that $\mathrm{F}^{-1}H$ is the Galerkin projection of the vertical component of velocity into the free surface function space. If we make the following simplifying assumptions:

1. The system is modelled in an Eulerian frame, with a non-moving free surface boundary.
2. This boundary is horizontal and completely flat (i.e. a Cartesian domain, no curved boundaries as in a spherical domain).
3. $\Delta\rho$ and g are constant along the free surface.
4. The function space for η is the same as, or a superset of, the function space containing the vertical component of $\boldsymbol{u}$ at the free surface.

then $\mathrm{F}^{-1}H$ is in fact just the identity operator (or an inclusion if the vertical velocity space is a subspace of the free surface function space). Furthermore, with $\alpha = \theta, \beta = 0$, we have $\mathrm{S}^{\mathrm{Kaus}} = \Delta t\theta H$ and thus we obtain the exact same system as in (2.63). Thus with these assumptions, the implicit free surface method in section 2.2.2 is mathematically the same as the Eulerian version of the Kaus stabilisation scheme introduced in the previous section.

For Eulerian models that do not satisfy assumptions 2-4, it is reasonable to assume that the Eulerian scheme of (2.63) with a stabilisation term of the form (2.65) is still very close to the scheme of section 2.2.2. In fact, the scheme of section 2.2.2 can always be written in the form

(2.63) if we choose a function space for η such that (2.15) can be represented exactly for the chosen discretisation of $\boldsymbol{u}$. Although this still has to be confirmed by running some relevant test cases, including in non Cartesian domains, we expect the numerical properties of both schemes to be practically identical. The new variant in the form (2.63) has the advantage of not needing to include the free surface degrees of freedom in the coupled $\boldsymbol{u}, p$ Stokes system solve. The free surface solution can be obtained in a separate step afterwards through (2.15) and used in the next timestep to assemble the right-hand side vector $\underline{h} = \mathrm{H}\underline{\tilde{\eta}}^n$.

2.6.3 Nonlinear approach

Another approach to deal with the free surface stability problem is to solve the nonlinear Stokes problem in a Newton iteration and update the free surface movement in every iteration. This approach is taken in Furuichi et al. (2015). In their work the free surface is tracked through a Marker in Cell (MIC) method. For the updates during the Newton iteration however, they also consider an Eulerian advection scheme to avoid the cost of the MIC at every Newton iteration. It should be noted that although the free surface is updated in the residual calculations, the effect of the movement is not taken into account in the Jacobian matrix. A true full Newton approach where the nonlinearity due to the movement of nodes in a Lagrangian mesh is taken into account is also possible and was discussed, e.g., by May et al. (2011). This does however require the ability to take the derivative of the entire discretisation with respect to the coordinates of the mesh nodes which can be challenging in terms of implementation. In a modern framework that allows symbolic differentiation of the discrete system, like Firedrake (Rathgeber et al., 2016), used in the geodynamical modelling of Davies et al. (2022), this would however be fairly straightforward.

The additional cost of the Newton iterations can of course be prohibitive. In a tightly coupled model that is already very nonlinear, the Newton iterations might be required regardless in which case the cost of updating the free surface during the Newton iterations might be relatively small. In a model that is otherwise linear, or near linear, the Newton iterations in fact come down to completely redoing the same timestep after updating the free surface and thus the

computational cost is multiplied by the number of iterations required. This approach is in fact the same as taken with the nonlinear explicit method in section 2.2.2. In its implementation in Fluidity however no explicit residuals are calculated, but one can iterate to convergence in the free surface solution (and other fields) itself. Rather than completely converging the residual, or the solution, one can also perform a fixed number of iterations purely to improve the stability.

2.6.4 Stability Analysis and Exponential Time Integration

In Rose et al. (2017) a more detailed stability analysis is presented of explicit free surface methods, and the stabilisation of Kaus et al. (2010). They then present a new exponential time integration of the free surface, which they name "nonstandard finite-difference". The stability criterion they derive for the free surface with stabilisation as in Kaus et al. (2010) is however, I believe, incorrect. Therefore I will first briefly review the steps from their analysis reformulated in the notation of this chapter, thus making clear that this analysis also applies to the implicit time integration scheme of this chapter.

As a starting point, Rose et al. (2017) notes that instead of applying a zero pressure boundary condition at the true location of a moving free surface in a Lagrangian model, one can simply apply the hydrostatic pressure associated with the free surface deviation η (corresponding to ζ in Rose et al. (2017)): "we will therefore evaluate the integrals in Eq. (10) over the hydrostatic reference surface and introduce a temporary auxiliary variable ζ which represents the (small) topography of the free surface relative to that reference surface." Doing so however implies that the solution $\boldsymbol{u}, p$ is in fact solved for only in the fixed domain below the reference level. Thus the changing domain $\Omega(t)$ and its boundary $\Gamma(t)$ in their equations (13) and onwards can in fact not be interpreted as moving with the free surface at all. Their equation (13) in our notation takes the form

$$\mathrm{K}\underline{u} + \mathrm{G}\underline{p}' + H\underline{\tilde{\eta}} = 0, \tag{2.69}$$

and if a changing domain were taken into account in the integrals, and in particular in that of the continuity equation $\mathrm{G}^T\underline{u} = 0$, the problem would become nonlinear and the normal

mode analysis would not be valid. Thus the rest of the analysis really comes down to the same approximation made in an Eulerian frame in which the free surface does not move. Note that the hydrostatic pressure has been removed here, and no other external forcing is assumed so that $\underline{f} = 0$, and we indeed get the same as in the explicit Eulerian method, equation (2.14), in this chapter.

The next step considers normal mode solutions $\underline{u}_i, \underline{p}'_i, \underline{\tilde{\eta}}_i$ with relaxation time τ_i for which

$$\mathrm{F}\frac{\mathrm{d}}{\mathrm{d}t}\underline{\tilde{\eta}}_i(t) = \mathrm{F}\frac{\mathrm{d}}{\mathrm{d}t}\underline{\tilde{\eta}}_i(t=0)e^{-t/\tau_i} = -\mathrm{F}\frac{1}{\tau_i}\underline{\tilde{\eta}}_i(t) = \mathrm{H}^T\underline{u}_i \tag{2.70}$$

(this is equation (14) in Rose et al. (2017) except we have already introduced the spatial FEM discretisation of the kinematic boundary condition (2.15)). We can use this to eliminate the free surface

$$K\underline{u}_i + \mathrm{G}\underline{p}'_i - \tau_i \mathrm{H}\mathrm{F}^{-1}\mathrm{H}^T\underline{u}_i = 0 \tag{2.71}$$

Thus we might find normal solutions by solving the following generalised eigenvalue problem

$$\begin{pmatrix} \mathrm{K} & \mathrm{G} \\ \mathrm{G}^T & 0 \end{pmatrix} \begin{pmatrix} \underline{u}_i \\ \underline{p}'_i \end{pmatrix} = \tau_i \begin{pmatrix} \mathrm{H}\mathrm{F}^{-1}\mathrm{H}^T & 0 \\ 0 & 0 \end{pmatrix} \begin{pmatrix} \underline{u}_i \\ \underline{p}'_i \end{pmatrix} \tag{2.72}$$

Note that although $\underline{u}_i, \underline{p}'_i$, and $\underline{\tilde{\eta}}_i$ are time dependent, they are just being rescaled by a factor e^{-t/τ_i} over time, so they still represent the same eigen solution over time.

In the explicit method we solve for a given free surface elevation $\underline{\tilde{\eta}}^n$ at time t^n:

$$\begin{pmatrix} \mathrm{K} & \mathrm{G} \\ \mathrm{G}^T & 0 \end{pmatrix} \begin{pmatrix} \underline{u} \\ \underline{p}' \end{pmatrix} = \begin{pmatrix} -\mathrm{H}\underline{\tilde{\eta}} \\ 0 \end{pmatrix} \tag{2.73}$$

Thus if we start from $\underline{\tilde{\eta}}^n = \underline{\tilde{\eta}}_i$, then by construction

$$\mathrm{H}^T\underline{u} = -\frac{1}{\tau_i}F\eta^n, \tag{2.74}$$

and thus if we update the free surface according to (2.67), we get

$$\underline{\tilde{\eta}}^{n+1} = \underline{\tilde{\eta}}^{n} + \Delta t F^{-1} H^T \underline{u} = (1 - \frac{\Delta t}{\tau_i})\underline{\tilde{\eta}}^{n}. \tag{2.75}$$

For stability we require that the amplification factor satisfies $|1-\Delta t/\tau_i| < 1$, or $\Delta t < 2\tau_i$. Thus if $\tau_{\min}$ is the smallest relaxation time, which as we have seen is associated with the largest (in length) free surface mode, we require $\Delta t < 2\tau_{\min}$, in agreement with Rose et al. (2017).

Now let us consider the case of the stabilised method. In Rose et al. (2017) the same assumptions are made as in section 2.6.2 such that we may assume

$$\mathrm{S}^{\mathrm{Kaus}}\underline{u} = \Delta t\theta \mathrm{H}\mathrm{F}^{-1}\mathrm{H}^T\underline{u} \tag{2.76}$$

and thus for a given $\underline{\tilde{\eta}}^n$ we solving the same system as in (2.68) for $\underline{u}$ and $\underline{p}'$. One could therefore look at the normal modes of

$$\begin{pmatrix} \mathrm{K} + \Delta t\theta \mathrm{H}\mathrm{F}^{-1}\mathrm{H}^T & \mathrm{G} \\ \mathrm{G}^T & 0 \end{pmatrix} \begin{pmatrix} \underline{u}_i^S \\ \underline{p}'^S_i \end{pmatrix} = \tau_i^S \begin{pmatrix} \mathrm{H}\mathrm{F}^{-1}\mathrm{H}^T & 0 \\ 0 & 0 \end{pmatrix} \begin{pmatrix} \underline{u}_i^S \\ \underline{p}'^S_i \end{pmatrix} \tag{2.77}$$

but this is the same as

$$\begin{pmatrix} \mathrm{K} & \mathrm{G} \\ \mathrm{G}^T & 0 \end{pmatrix} \begin{pmatrix} \underline{u}_i^S \\ \underline{p}'^S_i \end{pmatrix} = (\tau_i^S - \Delta t\theta) \begin{pmatrix} \mathrm{H}\mathrm{F}^{-1}\mathrm{H}^T & 0 \\ 0 & 0 \end{pmatrix} \begin{pmatrix} \underline{u}_i^S \\ \underline{p}'^S_i \end{pmatrix} \tag{2.78}$$

Thus we obtain the same normal modes $\underline{u}_i^S = \underline{u}_i$, $\underline{p}'^S_i = \underline{p}'_i$ where $\tau_i^S - \Delta t\theta = \tau_i$, or $\tau_i^S = \tau_i + \Delta t\theta$, and we conclude that the stabilisation method increases the relaxation time with $\Delta t\theta$, and we obtain a relaxed stability criterion of $\Delta t < 2(\tau_{\min} + \Delta t\theta)$.

So far we agree with Rose et al. (2017) (cf. their equation (28)). To obtain an explicit bound on Δt however, we derive

$$\Delta t - 2\Delta t\theta = (1 - 2\theta)\Delta t < 2\tau_{\min}, \tag{2.79}$$

which for $0 \leq \theta < \frac{1}{2}$ leads to

$$\Delta t < \frac{2}{1-2\theta}\tau_{\min} \tag{2.80}$$

which is different from their equation (29) which misses the 2 in the denominator. This missing 2 is important in the following step. For $\theta \geq \frac{1}{2}$ the factor $(1-2\theta)$ becomes negative (or zero for $\theta = \frac{1}{2}$) and thus (2.79) is satisfied automatically: the scheme becomes unconditionally stable!

This conclusion should not be a surprise; as we have derived in the previous section, the stabilised system, although it looks like an explicit Euler time integration of the original system with a stabilisation term to increase the minimal timestep, is in fact equivalent to an implicit θ-scheme time discretisation of the free surface dynamics. Instead of labelling the stabilisation of Kauss as quasi-implicit, as in Rose et al. (2017), it is therefore more appropriately interpreted as semi-implicit (as opposed to fully implicit for the nonlinear case (Furuichi et al., 2015) and the previous section). The stability for $\theta \geq \frac{1}{2}$, and second order convergence for the linear case, is then a standard result.

It should be noted that although we indeed get unconditional stability for $\theta \geq \frac{1}{2}$, if we look at the amplification factor in

$$\underline{\tilde{\eta}}^{n+1} = \left(1 - \frac{\Delta t}{\tau_i^S}\right)\underline{\tilde{\eta}}^n \tag{2.81}$$

which we derive assuming a $\underline{\tilde{\eta}}^n = \underline{\tilde{\eta}}_i^S$ with

$$\mathrm{H}^T \underline{u}_i^S = -\frac{1}{\tau_i^S}\underline{\tilde{\eta}}^n \tag{2.82}$$

which is required to make (2.77) equivalent with (2.68), then this amplification factor $1-\Delta t/\tau_i^S$ can become negative, leading to oscillatory behaviour for short timescale modes. As long as we satisfy the stability criterion strictly, e.g. $\theta > \frac{1}{2}$, these oscillations will be dampened out over time. As such oscillations may still be undesirable, to ensure monotonic decrease of all modes we need to ensure a positive damping factor with $\Delta t > \tau_i^S$ or $\Delta t > \tau_{\min}/(1-\theta)$. This thus requires a timestep restriction for all $\theta < 1$ that is stricter than the stability criterion, even for the fully explicit case $\theta = 0$. This also explains the oscillatory behaviour observed in figure 2.2c) for $\theta = \frac{1}{2}$.

The main contribution of Rose et al. (2017) however is the introduction of a new time-integration scheme, which in our notation can be written as

$$\underline{\tilde{\eta}}^{n+1} = \underline{\tilde{\eta}}^{n} + \tau^* \left(1 - e^{-\Delta t/\tau^*}\right) \mathrm{F}^{-1}\mathrm{H}^T \underline{u} \tag{2.83}$$

and is solved in conjunction with the same, unstabilised system as in (2.73). For the normal mode analysis we can therefore use the same relation between $\underline{u}_i$ and $\underline{\tilde{\eta}}_i$ as in (2.74) and obtain

$$\underline{\tilde{\eta}}^{n+1} = \left(1 - \frac{\tau^*}{\tau_i}\left(1 - e^{-\Delta t/\tau^*}\right)\right) \underline{\tilde{\eta}}^{n} \tag{2.84}$$

which can be made unconditionally stable by choosing

$$\tau^* \leq 2\tau_{\min}. \tag{2.85}$$

Otherwise we have a timestep restriction

$$\Delta t \leq -\tau^* \log\left(1 - 2\frac{\tau_{\min}}{\tau^*}\right) \tag{2.86}$$

As we observed previously, to ensure non-oscillatory behaviour stricter criteria can be imposed to guarantee a positive damping factor, e.g. $\tau^* \leq \tau_{\min}$.

A drawback of this scheme is that it becomes quite important to carefully choose τ^*, as a value of τ^* that is too small leads to over-stabilisation of the free surface dynamics. A good choice would therefore be $\tau^* \approx \tau_{\min}$ but it is not straightforward to derive an estimate for $\tau_{\min}$ in all cases. A number of approaches are discussed in Rose et al. (2017). It remains to be seen how this scheme behaves in a large scale application with modes at various length scales: how does the choice of τ^* near $\tau_{\min}$ associated with large scale modes, affect the temporal accuracy of the evolution of smaller scale free surface modes?

Finally, Rose et al. (2017) compares the stabilised scheme, which we argue is the same as our implicit scheme, with the new exponential time integration. They do this using the analytical test case worked out in 2.3. This comparison is a little inconclusive as for this case the explicit

time integration can in fact be made exact if τ^* is chosen to be the same as the relaxation time of the free surface mode. For other choices of τ^* the scheme is first order, as is the quasi/semi implicit scheme with $\theta = 0$ or $\theta = 1$. As they observe for $\theta = \frac{1}{2}$ the semi implicit scheme converges at second order which we can now explain from the fact that it is equivalent to the implicit scheme studied in this chapter. Rose et al. (2017) also compare the two methods for the "drunken sailor" case, but only at relatively low CFL, and for the chosen values it is not immediately obvious which method is more accurate.

2.7 Final Conclusions

The implicit scheme for free surface evolution in geodynamical models, introduced and analysed in Kramer et al. (2012), and here in sections 2.2 and 2.4, is accurate and stable for large time steps. It can be made unconditionally stable using $\theta \geq \frac{1}{2}$ and second order accurate with $\theta = \frac{1}{2}$. With a number of simplifying assumptions it was shown in section 2.6.2 that the scheme can in fact be seen to be equivalent in an Eulerian frame to the stabilisation scheme of Kaus et al. (2010) for Lagrangian models. This analysis also makes it possible to solve the Stokes system for velocity and pressure without having to explicitly include additional free surface degrees of freedom in the system, which simplifies its implementation.

Similar conclusions can most likely be drawn for the case where these simplifying assumptions are not met, e.g. in a curved spherical shell domain, but this requires implementation and further testing. In particular we note the importance of maintaining symmetry in the stabilisation term as we advocate in (2.65) to maintain consistency with original implicit scheme where we do include η in the Stokes system. This symmetry is in fact also important for the stability analysis of section 2.6.4.

The analytical solutions, originally based on Zhong et al., 1996, worked out in detail in Kramer et al., 2012, and here in section 2.3, have already proven useful as benchmark in a number of publications (Furuichi et al., 2015; Rose et al., 2017; Wilson et al., 2017). Further work is needed to compare the various free surface methods that have been proposed, in particular in

more challenging circumstances: large scale models with free surface modes of various length scales and thus time scales, curved cylindrical or spherical domains, and problems with variable density at the free surface.

As a final note on an aspect of geodynamical free surface models that is easily overlooked, if the temporal evolution of the free surface in response to various forcings in the mantle is deemed important, one should also have a good understanding of the appropriate initial condition for the free surface. In models without a free surface, only the initial temperature is required as the system is in essence driven by the temporal evolution of temperature from which at any point in time velocity and pressure can be derived. The dynamic response at the surface in the form of dynamic topography can be derived from the normal stress at the surface of that solution, assuming this stress is immediately balanced by an equivalent lithostatic pressure associated with the free surface elevation of the dynamic response.

If we do include a dynamic free surface in the model, this response is not immediate, and we can choose an initial condition for the free surface that does not match the normal stresses from the initial flow in the interior, in which case we obtain immediate movement of the free surface. If we want to assume an equilibrium free surface from the start, we need to carefully select its initial condition. In a typical simulation in which the initial density distribution in the interior of the mantle leads to immediate flow with nontrivial normal stresses at the surface, a zero free surface is not in balance. An equilibrium initial free surface can be found in this case by first solving a steady state Stokes system with free slip boundary conditions (zero normal flow) forced by the initial density distribution, and calculating the free surface response required to match the resulting normal stresses. If the non-immediate response of the free surface is thought to be important for the dynamics of a specific problem, e.g. in a subduction model, then we need to consider whether this imbalance needs to be present from the start in our simulation, or whether we can achieve the lagged nature of the response by running the model for some time starting from equilibrium.

Chapter 3

Analytical solutions for mantle flow in cylindrical and spherical shells

In the previous chapter we have seen the importance of analytical test cases for a thorough evaluation and comparisons of the properties of numerical schemes for mantle convection modelling, and for testing their correct implementation. This chapter focuses on a versatile set of analytical solutions for the Stokes equations in spherical and cylindrical shell domains. We demonstrate its value by performing a numerical convergence study using the spatial discretisation of these equations in Fluidity. Here, in particular, we highlight a convergence issue for the popular Taylor-Hood (P2-P1) finite element in the presence of discontinuities in pressure. This chapter is based on Kramer, Davies, and Wilson, "Analytical solutions for mantle flow in cylindrical and spherical shells" (2021), with its mathematical notation adjusted to fit the rest of the thesis.

To make this suite of analytical solutions more readily available to the wider geodynamic modelling community, the python package *Assess*, implements the analytical solutions and provides useful functions to evaluate them at arbitrary locations in the domain. It is available from `http://github.com/stephankramer/assess` (see `https://assess.readthedocs.io` for documentation). An archived version, used in the experiments in this chapter, is available from `https://doi.org/10.5281/zenodo.3891545`. To ensure correctness, both in the manuscript

as in the python package, the coefficients for the various solutions have been extracted from the LaTeX-source automatically using SymPy (Meurer et al., 2017), verified to adhere to the equations using SageMath (The Sage Developers, 2019), and substituted in the python package.

3.1 Introduction

Recent decades have seen extensive validation, verification and benchmarking of Cartesian mantle dynamics codes, in both 2- and 3-D. Verification is typically achieved via comparisons of numerical predictions against analytical solutions (e.g. Zhong et al., 1993; Kramer et al., 2012), with benchmarking typically undertaken against solutions from other comparable codes, for incompressible (Blankenbach et al., 1989; Travis et al., 1990; Busse et al., 1994; van Keken et al., 1997; van Keken et al., 2008; Tosi et al., 2015) and compressible (King et al., 2009) convection. See also Popov et al. (2014) for an overview of geodynamical benchmarks. The number of comparable studies, within a 2-D cylindrical or 3-D spherical geometry, however, is more limited. Given a recent surge in the state-of-the-art tools available for simulating mantle dynamics in these geometries (e.g. Kronbichler et al., 2012; Logg et al., 2012; Burstedde et al., 2013; Rathgeber et al., 2016; Heister et al., 2017; Wilson et al., 2017), it is important that these tools are verified and validated against a range of analytical and benchmark solutions.

A popular method to obtain analytical solutions is the Method of Manufactured Solutions (MMS; Roache, 2002). With this approach, an arbitrary analytical solution is chosen beforehand and the necessary forcing terms on the right-hand side are derived by substitution of the solution into the left-hand side of the flow equations. A drawback of this approach is that it can be hard to choose solutions: (i) that satisfy physically realistic boundary conditions, in particular, in less trivial domains; and (ii) with a velocity that is divergence free, to avoid unnatural source terms. Alternatively, one can choose a simple analytical expression for the forcing but the derivation of the corresponding analytical solutions is often laborious.

For the Stokes equations, a well-known set of solutions in the latter category is based on a forcing term in the form of a delta-function, corresponding to an infinitely thin density anomaly at a

certain depth. The solutions to these are also used in the propagator matrix method, where a convolution of delta-function solutions at different depths is used to obtain the response to arbitrary density anomalies (e.g. Hager et al., 1989). Solutions for the Cartesian case have been published (e.g. Zhong et al., 1993; Kramer et al., 2012). Spherical solutions can be found in, for example, Ribe (2009). They have previously been used for validation by, for example, Zhong et al. (2000) and Zhong et al. (2008a), Choblet et al. (2007), Davies et al. (2013) and Burstedde et al. (2013). The derivation of these solutions is non-trivial and, often, only cases with simpler free-slip boundary conditions are explicitly presented. Here, we derive solutions for both free- and zero-slip boundary conditions. In our convergence analyses, where we compare the analytical solutions with numerical solutions obtained using the Fluidity computational modelling framework (Davies et al., 2011), we discuss a limitation of this set of solutions for the benchmarking of geodynamic codes.

For this reason, we also present solutions based on a smooth forcing term, with radial dependence formed by a polynomial of arbitrary order, again for free- and zero-slip cases. This set of solutions provides a flexible way to test mantle dynamics codes with physically relevant solutions, where, for instance, a high order polynomial forcing can be used to obtain solutions with a strong gradient near the surface. The radial dependence can be combined with spherical harmonics of arbitrary degree and order.

A key step in the derivation of these benchmarks is a decomposition of the solution into poloidal and toroidal components in the Mie representation (Backus, 1986). This results in a biharmonic equation for the poloidal scalar function. Combined with a set of conditions for the radial dependence of this poloidal function, analytical Stokes solutions can be obtained that satisfy desired free-slip or zero-slip conditions. Similar techniques have been used in Tosi et al. (2007) and Horbach et al. (2020). In Section 3.5.1, we will discuss previously published analytical benchmark cases in shell domains and how they differ from those presented here (e.g. Blinova et al., 2016; Thieulot, 2017; Horbach et al., 2020).

Finally, in addition to the delta-function and smooth cases with either free-slip or zero-slip boundary conditions in a spherical-shell domain, we present the solutions for the corresponding

four cases in a 2-D cylindrical shell domain (annulus). Although ultimately, mantle convection is a 3-D phenomenon, a number of processes can be modelled adequately in two dimensions and, accordingly, access to benchmark cases for 2-D numerical models is equally important. The number of published analytical Stokes solutions in 2-D cylindrical shell domains, which are suitable as geodynamic benchmarks and include a complete derivation, is limited. By presenting this extensive set of explicit analytical solutions, we provide a suite of verification cases for use by the wider community of mantle dynamics code developers. An implementation of the solutions is provided through the python package Assess (*analytical solutions for the stokes equations in spherical shells*; Kramer, 2020).

The remainder of this chapter is structured as follows. In Section 3.2 we derive the analytical solutions in cylindrical (section 3.2.2) and spherical (section 3.2.3) geometries. Smooth solutions are first provided, for free-slip and zero-slip cases, followed by the delta-function solutions. In Section 3.3, we briefly revise Fluidity's numerical implementation of mantle convection model solving the Stokes equations, which is used in Section 3.4 to obtain convergence results of the P2-P1 finite element discretisation to the analytical solutions. In Section 3.5 we discuss these results, and relate the analytical solutions presented here to those that have previously been published. In particular, we discuss an issue with the delta-function cases for discretisations that use continuous pressure. To demonstrate, we also show results with a $\mathrm{P2_{bubble}}$-$\mathrm{P1_{DG}}$ discretisation that overcomes this issue.

3.2 Analytical Solutions

3.2.1 Equations

The following derivation is applicable to the incompressible Stokes equations

$$-\nabla \cdot \boldsymbol{\tau} + \nabla p' = -g\rho' \hat{\boldsymbol{r}}, \tag{3.1}$$

$$\boldsymbol{\tau} = \mu \left[\nabla \boldsymbol{u} + \nabla \boldsymbol{u}^T \right], \tag{3.2}$$

$$\nabla \cdot \boldsymbol{u} = 0, \tag{3.3}$$

where the unknowns are velocity $\boldsymbol{u}$ and pressure p', with an assumed constant viscosity μ. The buoyancy force on the right hand side (RHS) of (3.1) is based on a gravity of constant magnitude g, directed in the inward radial direction $-\hat{\boldsymbol{r}}$, and a density deviation ρ': $\rho = \rho_0 + \rho'$, where ρ is the density and the reference density ρ_0 is constant. The equations are solved in a 2-D cylindrical or 3-D spherical domain, bounded by $R_- \leq r \leq R_+$, where r is the radial distance to the origin.

3.2.2 Cylindrical

As in section 2.3, any incompressible velocity field $\boldsymbol{u}$ in two dimensions, can be written as the skew gradient of a streamfunction ψ, here in polar coordinates:

$$u_r = -\frac{1}{r}\frac{\partial \psi}{\partial \varphi}, \quad u_\varphi = \frac{\partial \psi}{\partial r}, \tag{3.4}$$

where φ is the angle from the x-axis in polar coordinates, $x = r\cos(\varphi), y = r\sin(\varphi)$, and u_r and u_φ are the radial and transverse components of velocity respectively. The normal deviatoric

stress and shear stress components are given by

$$\tau_{rr} = 2\mu\hat{\boldsymbol{r}} \cdot (\nabla \boldsymbol{u}) \cdot \hat{\boldsymbol{r}} = -2\mu \frac{\partial}{\partial r}\left(\frac{1}{r}\frac{\partial \psi}{\partial \varphi}\right), \tag{3.5}$$

$$\tau_{r\varphi} = \mu\hat{\boldsymbol{r}} \cdot (\nabla \boldsymbol{u}) \cdot \hat{\boldsymbol{\varphi}} + \mu\hat{\boldsymbol{\varphi}} \cdot [\nabla \boldsymbol{u}] \cdot \hat{\boldsymbol{r}} = \mu\left(\frac{\partial^2 \psi}{\partial r^2} - \frac{1}{r}\frac{\partial \psi}{\partial r} - \frac{1}{r^2}\frac{\partial^2 \psi}{\partial \varphi^2}\right). \tag{3.6}$$

The momentum equation (3.1) can be decomposed into radial and transverse components

$$\frac{\mu}{r}\frac{\partial}{\partial \varphi}\nabla^2\psi + \frac{\partial p'}{\partial r} = -g\rho', \tag{3.7}$$

$$-\mu\frac{\partial}{\partial r}\nabla^2\psi + \frac{1}{r}\frac{\partial p'}{\partial \varphi} = 0, \tag{3.8}$$

where the Laplacian, in polar coordinates, is given by

$$\nabla^2\psi = \frac{1}{r}\frac{\partial}{\partial r}\left(r\frac{\partial \psi}{\partial r}\right) + \frac{1}{r^2}\frac{\partial^2 \psi}{\partial \varphi^2}. \tag{3.9}$$

For compactness, the derivation of equations (3.5)–(3.8) in polar coordinates has been skipped here, and is worked out in section 3.7.

The curl of the momentum equation is obtained by summation of the operators $-\frac{1}{r}\frac{\partial \bullet}{\partial \varphi}$ and $\frac{1}{r}\frac{\partial}{\partial r}(r\bullet)$ applied to the radial (3.7) and transverse (3.8) components respectively, which leads to

$$-\nabla^4\psi = \frac{g}{\mu}\frac{1}{r}\frac{\partial \rho'}{\partial \varphi}. \tag{3.10}$$

The general, real-valued, solution to the biharmonic equation $\nabla^4\psi = 0$ is given by

$$\begin{aligned}\psi(r,\varphi) = \sum_{n>1} &\left(A_n r^n + B_n r^{-n} + C_n r^{n+2} + D_n r^{-n+2}\right)\left(e_n \sin(n\varphi) + f_n \cos(n\varphi)\right) \\ &+ \left(A_1 r + B_1 r^{-1} + C_1 r^3 + D_1 r \ln r\right)\left(e_1 \sin(\varphi) + f_1 \cos(\varphi)\right) \\ &+ A_0 + B_0 \ln r + C_0 r^2 + D_0 r^2 \ln r,\end{aligned} \tag{3.11}$$

where A_n, B_n, C_n, D_n, e_n, and f_n are constant coefficients, $n \geq 0$. The A_n and B_n terms are the standard solutions to the homogeneous harmonic equation, and the C_n and D_n terms are obtained as inhomogeneous solutions of the harmonic equation with the homogeneous harmonic

solutions (A_n and B_n terms) as the right-hand side. The fact that these (the C_n and D_n terms) are homogeneous biharmonic solutions then follows from: $\nabla^4 = \nabla^2\nabla^2$. In the following we will, for simplicity, focus on $\sin(n\varphi)$-solutions for a single $n > 1$ and set $e_n = 1, f_n = 0$.

An equation for pressure can be derived by taking the *divergence* of the momentum equation

$$\nabla^2 p' = -\frac{g}{r}\frac{\partial(r\rho')}{\partial r}. \tag{3.12}$$

From (3.7) it can be seen that $\sin(n\varphi)$ solutions for ψ are associated with $\cos(n\varphi)$ solutions of p' and ρ'. The homogeneous solutions, i.e. $\rho' = 0$, are thus the standard harmonic solutions (again neglecting the $n = 0, 1$ solutions)

$$p'(r,\varphi) = \sum_{n>1} \left(G_n r^n + H_n r^{-n}\right)\cos(n\varphi), \tag{3.13}$$

where G_n and H_n are constant coefficients, $n > 1$.

After substitution of p' and ψ in (3.7)–(3.8), the following relations

$$G_n = -4\mu C_n(n+1), \quad H_n = -4\mu D_n(n-1), \tag{3.14}$$

between the coefficients of the homogeneous solutions for ψ and p' can be derived.

Smooth density profile – cylindrical

In the first test case we consider a density perturbation of the following form

$$\rho' = \frac{r^k}{R_+^k}\cos(n\varphi) \tag{3.15}$$

with $k > 0$. It is easily verified that an inhomogeneous solution to (3.10) exists of the form

$$\psi = E r^{k+3}\sin(n\varphi), \quad E = \frac{g R_+^{-k} n}{\mu\left((k+3)^2 - n^2\right)\left((k+1)^2 - n^2\right)} \tag{3.16}$$

assuming $k \neq n-3$ and $k \neq n-1$, so that a general solution can be written as

$$\psi(r,\varphi) = \left(Ar^n + Br^{-n} + Cr^{n+2} + Dr^{-n+2} + Er^{k+3}\right)\sin(n\varphi). \tag{3.17}$$

Note that for the remainder of this derivation we drop the subscript n in the coefficients for A, B, C and D.

An inhomogeneous solution for pressure of (3.12) is given by

$$p'(r,\varphi) = Fr^{k+1}\cos(n\varphi), \quad F = -\frac{gR_+^{-k}(k+1)}{(k+1)^2 - n^2}. \tag{3.18}$$

The general solution for pressure is thus

$$p'(r,\varphi) = \left(Gr^n + Hr^{-n} + Fr^{k+1}\right)\cos(n\varphi) \tag{3.19}$$

with G and H given by (3.14).

The four remaining coefficients A, B, C, and D, are fixed by a choice of boundary conditions at the inner and outer surfaces of the cylindrical domain at $r = R_+$ and $r = R_-$, respectively. At both, no-normal flow conditions are imposed via $\frac{\partial\psi}{\partial\varphi} = 0$. Two further equations are found by imposing either $\tau_{r\varphi} = 0$ (free slip), or $\frac{\partial\psi}{\partial r} = 0$ (zero slip) at both boundaries.

The solution coefficients for free-slip, no-normal flow at both boundaries are given by

$$\begin{aligned}
A &= \frac{gR_+^{-n+3}}{\mu}\frac{\alpha^{k+n+3} - \alpha^2}{4\left(\alpha+\alpha^n\right)\left(\alpha^n-\alpha\right)(k+n+1)(k-n+3)} \\
B &= \frac{gR_+^{n+3}}{\mu}\frac{\alpha^{k+n+3} - \alpha^{2n+2}}{4\left(\alpha^{n+1}+1\right)\left(\alpha^{n+1}-1\right)(k+n+3)(k-n+1)} \\
C &= \frac{gR_+^{-n+1}}{\mu}\frac{-\alpha^{k+n+3} + 1}{4\left(\alpha^{n+1}+1\right)\left(\alpha^{n+1}-1\right)(k+n+3)(k-n+1)} \\
D &= \frac{gR_+^{n+1}}{\mu}\frac{-\alpha^{k+n+3} + \alpha^{2n}}{4\left(\alpha+\alpha^n\right)\left(\alpha^n-\alpha\right)(k+n+1)(k-n+3)}
\end{aligned}$$

where we use $\alpha = R_-/R_+$.

The zero-slip solution coefficients are given by

$$A = \frac{gR_+^{-n+3}n}{\mu} \frac{\left(\alpha^{k+n+3}+\alpha^{2n}\right)(k+n+1)(n+1) - \left(\alpha^{k+n+1}+\alpha^{2n+2}\right)(k+n+3)n - \left(\alpha^{k+3n+3}+1\right)(k-n+1)}{2\left(\left(\alpha^{n+1}-\alpha^{n-1}\right)^2 n^2 - \left(\alpha^{2n}-1\right)^2\right)\left((k+3)^2-n^2\right)\left((k+1)^2-n^2\right)}$$

$$B = \frac{gR_+^{n+3}n}{\mu} \frac{-\left(\alpha^{k+3n+3}+\alpha^{2n}\right)(k-n+1)(n-1) + \left(\alpha^{k+3n+1}+\alpha^{2n+2}\right)(k-n+3)n - \left(\alpha^{k+n+3}+\alpha^{4n}\right)(k+n+1)}{2\left(\left(\alpha^{n+1}-\alpha^{n-1}\right)^2 n^2 - \left(\alpha^{2n}-1\right)^2\right)\left((k+3)^2-n^2\right)\left((k+1)^2-n^2\right)}$$

$$C = \frac{gR_+^{-n+1}n}{\mu} \frac{\left(\alpha^{k+n+1}+\alpha^{2n}\right)(k+n+3)(n-1) - \left(\alpha^{k+n+3}+\alpha^{2n-2}\right)(k+n+1)n + \left(\alpha^{k+3n+1}+1\right)(k-n+3)}{2\left(\left(\alpha^{n+1}-\alpha^{n-1}\right)^2 n^2 - \left(\alpha^{2n}-1\right)^2\right)\left((k+3)^2-n^2\right)\left((k+1)^2-n^2\right)}$$

$$D = \frac{gR_+^{n+1}n}{\mu} \frac{-\left(\alpha^{k+3n+1}+\alpha^{2n}\right)(k-n+3)(n+1) + \left(\alpha^{k+3n+3}+\alpha^{2n-2}\right)(k-n+1)n + \left(\alpha^{k+n+1}+\alpha^{4n}\right)(k+n+3)}{2\left(\left(\alpha^{n+1}-\alpha^{n-1}\right)^2 n^2 - \left(\alpha^{2n}-1\right)^2\right)\left((k+3)^2-n^2\right)\left((k+1)^2-n^2\right)}.$$

Green's function solution – cylindrical

Another set of useful solutions is found considering the following perturbation density

$$\rho' = \delta(r-r')\cos(n\varphi) \tag{3.20}$$

representing an infinitely thin density anomaly at $r = r'$ with $R_- < r' < R_+$. Since $\rho' = 0$ for $r' \neq r$, the solution is described by combining two homogeneous solutions

$$\psi(r,\varphi) = \begin{cases} \psi_-(r,\varphi) = (A_- r^n + B_- r^{-n} + C_- r^{n+2} + D_- r^{-n+2})\sin(n\varphi) & \text{for } R_- \leq r < r', \\ \psi_+(r,\varphi) = (A_+ r^n + B_+ r^{-n} + C_+ r^{n+2} + D_+ r^{-n+2})\sin(n\varphi) & \text{for } r' < r \leq R_+. \end{cases} \tag{3.21}$$

We thus have 8 coefficients that are fixed by boundary conditions and conditions at the interface. Boundary conditions at the inner and outer boundary again provide four equations. Furthermore we impose continuity of both velocity components at the interface

$$\psi_-(r',\varphi) = \psi_+(r',\varphi), \quad \text{and} \quad \frac{\partial\psi_-}{\partial r}(r',\varphi) = \frac{\partial\psi_+}{\partial r}(r',\varphi). \tag{3.22}$$

Since no lateral force is being applied at the interface we also expect continuity of the shear stress (3.6) which in combination with the above implies

$$\frac{\partial^2\psi_-}{\partial r^2}(r',\varphi) = \frac{\partial^2\psi_+}{\partial r^2}(r',\varphi). \tag{3.23}$$

Finally the eighth equation is obtained by integrating (3.10) over a small strip $r'-\epsilon \leq r \leq r'+\epsilon$, between two arbitrary angles $\varphi_1 \leq \varphi \leq \varphi_2$:

$$\int_{r=r'-\epsilon}^{r'+\epsilon} \int_{\varphi=\varphi_1}^{\varphi_2} \left(\nabla^4 \psi\right) r dr d\varphi = \int_{r=r'-\epsilon}^{r'+\epsilon} \int_{\varphi=\varphi_1}^{\varphi_2} \frac{gn\sin(n\varphi)}{\mu r} \delta(r-r') r dr d\varphi, \tag{3.24}$$

$$\left[\int_{\varphi=\varphi_1}^{\varphi_2} \hat{\boldsymbol{r}} \cdot \nabla \left(\nabla^2 \psi\right) r d\varphi \right]_{r=r'-\epsilon}^{r=r'+\epsilon} + \left[\int_{r=r'-\epsilon}^{r'+\epsilon} \hat{\boldsymbol{\varphi}} \cdot \nabla \left(\nabla^2 \psi\right) r dr \right]_{\varphi=\varphi_1}^{\varphi_2} = \int_{\varphi=\varphi_1}^{\varphi_2} \frac{gn\sin(n\varphi)}{\mu} d\varphi. \tag{3.25}$$

Taking the limit $\epsilon \to 0$, the second term on the left-hand side disappears, whereas the first term becomes

$$\int_{\varphi=\varphi_1}^{\varphi_2} \frac{\partial}{\partial r}\left(\frac{1}{r}\frac{\partial}{\partial r}\left(r\frac{\partial \psi_+}{\partial r}\right) + \frac{1}{r^2}\frac{\partial^2 \psi_+}{\partial \varphi^2}\right)\Big|_{r=r'} r' d\varphi - \int_{\varphi=\varphi_1}^{\varphi_2} \frac{\partial}{\partial r}\left(\frac{1}{r}\frac{\partial}{\partial r}\left(r\frac{\partial \psi_-}{\partial r}\right) + \frac{1}{r^2}\frac{\partial^2 \psi_-}{\partial \varphi^2}\right)\Big|_{r=r'} r' d\varphi.$$

Again using (3.22) and (3.23), only the jump term for the third radial derivative of $\psi_\pm$ remains:

$$\int_{\varphi=\varphi_1}^{\varphi_2} \left(\frac{\partial^3 \psi_+}{\partial r^3}(r',\varphi) - \frac{\partial^3 \psi_-}{\partial r^3}(r',\varphi)\right) r' d\varphi = \int_{\varphi=\varphi_1}^{\varphi_2} \frac{gn\sin(n\varphi)}{\mu} d\varphi.$$

Thus for this to hold for arbitrary φ_1 and φ_2, we need

$$\frac{\partial^3 \psi_+}{\partial r^3}(r',\varphi) - \frac{\partial^3 \psi_-}{\partial r^3}(r',\varphi) = \frac{gn\sin(n\varphi)}{\mu r'}. \tag{3.26}$$

The solution coefficients for free-slip boundary conditions at $r = R_-$ and $r = R_+$ are

$$\begin{aligned}
A_\pm &= \frac{gr'^{-n+2}}{\mu} \frac{\pm\left(\alpha_\mp^{2n-2}-1\right)}{8\left(\alpha_\pm^{2n-2}-\alpha_\mp^{2n-2}\right)(n-1)} \\
B_\pm &= \frac{gr'^{n+2}}{\mu} \frac{\pm\left(\alpha_\mp^{2n+2}-1\right)\alpha_\pm^{2n+2}}{8\left(\alpha_\pm^{2n+2}-\alpha_\mp^{2n+2}\right)(n+1)} \\
C_\pm &= \frac{gr'^{-n}}{\mu} \frac{\pm\left(\alpha_\mp^{2n+2}-1\right)}{8\left(\alpha_\mp^{2n+2}-\alpha_\pm^{2n+2}\right)(n+1)} \\
D_\pm &= \frac{gr'^{n}}{\mu} \frac{\pm\left(\alpha_\mp^{2n-2}-1\right)\alpha_\pm^{2n-2}}{8\left(\alpha_\mp^{2n-2}-\alpha_\pm^{2n-2}\right)(n-1)}
\end{aligned}$$

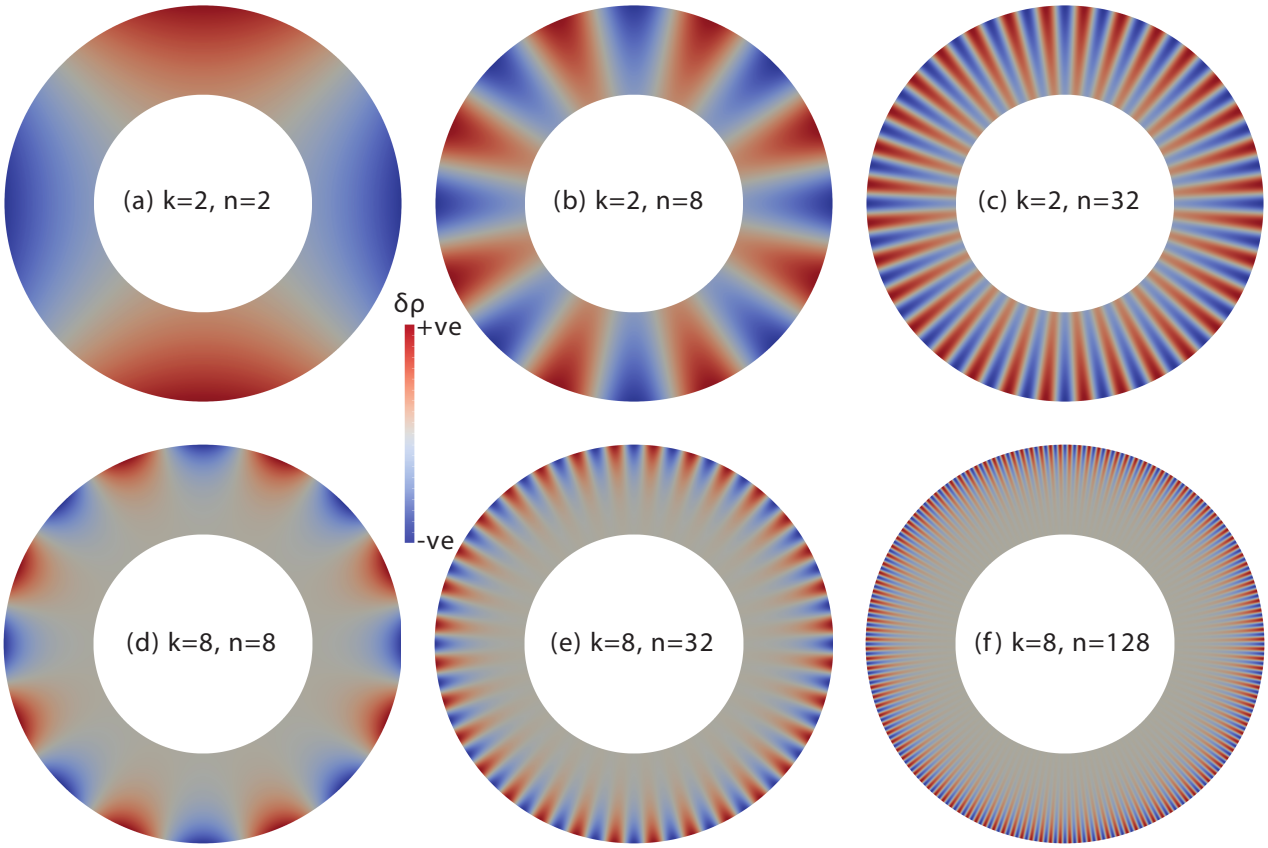


Figure 3.1: Density perturbation (ρ') field for smooth cylindrical cases across a range of n and k. As the wavenumber n increases, the wavelength of the perturbation decreases. As k increases, the perturbation becomes more concentrated towards the domain's outer boundary.

where we use $\alpha_\pm = R_\pm/r'$.

Zero-slip conditions at both boundaries lead to

$$A_\pm = \frac{gr'^{-n+2}}{\mu} \frac{\left(\left(\alpha_+^2 - \alpha_-^2\right) n + \alpha_+^{-2n} - \alpha_-^{-2n} \pm (n+1)\right)(n-1) - \left(\alpha_+^{-2n}\alpha_-^2 - \alpha_+^2\alpha_-^{-2n}\right) n \pm \left(\gamma^{\pm 2n} - \gamma^{\mp 2} n^2\right)}{8\left(\left(\gamma - \gamma^{-1}\right)^2 n^2 - \left(\gamma^{-n} - \gamma^n\right)^2\right)(n-1)}$$

$$B_\pm = \frac{gr'^{n+2}}{\mu} \frac{\left(\left(\alpha_+^2 - \alpha_-^2\right) n - \alpha_+^{2n} + \alpha_-^{2n} \pm (n-1)\right)(n+1) + \left(\alpha_+^{2n}\alpha_-^2 - \alpha_+^2\alpha_-^{2n}\right) n \pm \left(\gamma^{\mp 2n} - \gamma^{\mp 2} n^2\right)}{8\left(\left(\gamma - \gamma^{-1}\right)^2 n^2 - \left(\gamma^{-n} - \gamma^n\right)^2\right)(n+1)}$$

$$C_\pm = \frac{gr'^{-n}}{\mu} \frac{\left(\left(\alpha_-^{-2} - \alpha_+^{-2}\right) n + \alpha_+^{-2n} - \alpha_-^{-2n} \mp (n-1)\right)(n+1) - \left(\alpha_+^{-2n}\alpha_-^{-2} - \alpha_+^{-2}\alpha_-^{-2n}\right) n \mp \left(\gamma^{\pm 2n} - \gamma^{\pm 2} n^2\right)}{8\left(\left(\gamma - \gamma^{-1}\right)^2 n^2 - \left(\gamma^{-n} - \gamma^n\right)^2\right)(n+1)}$$

$$D_\pm = \frac{gr'^{n}}{\mu} \frac{\left(\left(\alpha_-^{-2} - \alpha_+^{-2}\right) n - \alpha_+^{2n} + \alpha_-^{2n} \mp (n+1)\right)(n-1) + \left(\alpha_+^{2n}\alpha_-^{-2} - \alpha_+^{-2}\alpha_-^{2n}\right) n \mp \left(\gamma^{\mp 2n} - \gamma^{\pm 2} n^2\right)}{8\left(\left(\gamma - \gamma^{-1}\right)^2 n^2 - \left(\gamma^{-n} - \gamma^n\right)^2\right)(n-1)}$$

where in addition we use $\gamma = R_-/R_+$.

3.2.3 Spherical

In this section we derive the equivalent of the four cylindrical cases in a 3-D spherical domain, $R_- \leq r \leq R_+$. A more detailed derivation of the equations can be found in Ribe (2009). In 3-D, a solenoidal velocity field $\boldsymbol{u}$ can be decomposed as

$$\boldsymbol{u} = \nabla \times (\boldsymbol{r} \times \nabla \mathcal{P}) + \boldsymbol{r} \times \nabla \mathcal{T} \tag{3.27}$$

using poloidal and toroidal scalar fields $\mathcal{P}$ and $\mathcal{T}$ (Backus, 1986), where $\boldsymbol{r} = r\hat{\boldsymbol{r}}$. In spherical coordinates

$$u_r = \frac{1}{r}\Lambda^2\mathcal{P}, \quad u_\theta = -\frac{1}{r}\frac{\partial^2(r\mathcal{P})}{\partial r \partial\theta} - \frac{1}{\sin(\theta)}\frac{\partial \mathcal{T}}{\partial \varphi}, \quad u_\varphi = -\frac{1}{r\sin(\theta)}\frac{\partial^2(r\mathcal{P})}{\partial r\partial\varphi} + \frac{\partial \mathcal{T}}{\partial\theta} \tag{3.28}$$

where φ is the longitude and θ is the co-latitude, and

$$\Lambda^2\mathcal{P} = \frac{1}{\sin(\theta)}\frac{\partial}{\partial\theta}\left(\sin(\theta)\frac{\partial\mathcal{P}}{\partial\theta}\right) + \frac{1}{\sin(\theta)^2}\frac{\partial^2\mathcal{P}}{\partial\varphi^2}, \text{ so that } \nabla^2 = \frac{1}{r^2}\left(\frac{\partial}{\partial r}r^2\frac{\partial}{\partial r} + \Lambda^2\right). \tag{3.29}$$

We further derive the following spherical components of deviatoric stress:

$$\tau_{rr} = 2\mu\frac{\partial u_r}{\partial r} = 2\mu\frac{\partial}{\partial r}\left(\frac{1}{r}\Lambda^2\mathcal{P}\right), \tag{3.30}$$

$$\tau_{r\theta} = \mu r\frac{\partial}{\partial r}\left(\frac{u_\theta}{r}\right) + \frac{\mu}{r}\frac{\partial u_r}{\partial\theta} = \mu\frac{\partial}{\partial\theta}\left(\frac{1}{r^2}\Lambda^2\mathcal{P} - \frac{\partial^2\mathcal{P}}{\partial r^2} + \frac{2}{r^2}\mathcal{P}\right) - \mu r\frac{\partial}{\partial r}\left(\frac{1}{r\sin(\theta)}\frac{\partial\mathcal{T}}{\partial\varphi}\right), \tag{3.31}$$

$$\tau_{r\varphi} = \mu r\frac{\partial}{\partial r}\left(\frac{u_\varphi}{r}\right) + \frac{\mu}{r\sin(\theta)}\frac{\partial u_r}{\partial\varphi} = \frac{\mu}{\sin(\theta)}\frac{\partial}{\partial\varphi}\left(\frac{1}{r^2}\Lambda^2\mathcal{P} - \frac{\partial^2\mathcal{P}}{\partial r^2} + \frac{2}{r^2}\mathcal{P}\right) + \mu r\frac{\partial}{\partial r}\left(\frac{1}{r}\frac{\partial\mathcal{T}}{\partial\theta}\right). \tag{3.32}$$

Using these, we can work out spherical components of the momentum equation (3.1) to be

$$-\frac{\mu}{r}\Lambda^2\nabla^2\mathcal{P} + \frac{\partial p'}{\partial r} = -g\rho', \tag{3.33}$$

$$\frac{\mu}{r}\frac{\partial^2(r\nabla^2\mathcal{P})}{\partial r\partial\theta} + \frac{\mu}{\sin(\theta)}\frac{\partial\nabla^2\mathcal{T}}{\partial\varphi} + \frac{1}{r}\frac{\partial p'}{\partial\theta} = 0, \tag{3.34}$$

$$\frac{\mu}{r\sin(\theta)}\frac{\partial^2(r\nabla^2\mathcal{P})}{\partial r\partial\varphi} + \mu\frac{\partial\nabla^2\mathcal{T}}{\partial\theta} + \frac{1}{r\sin(\theta)}\frac{\partial p'}{\partial\varphi} = 0. \tag{3.35}$$

As can be seen from these equations, the toroidal part of the solution is independent of the density distribution. A nonzero toroidal component is only introduced through a particular choice of boundary conditions. For the test cases in this paper we only consider free-slip and zero-slip boundary conditions with radial forcing so we may assume $\mathcal{T} = 0$. The assumption of the velocity field being solenoidal, which underlies the Mie representation (3.27), follows directly from the incompressibility condition and the no-normal flow condition on the boundary.

Taking the curl of the momentum equation

$$-\hat{\boldsymbol{\theta}}\frac{\mu}{\sin(\theta)}\frac{\partial\nabla^4\mathcal{P}}{\partial\varphi} + \hat{\boldsymbol{\varphi}}\mu\frac{\partial\nabla^4\mathcal{P}}{\partial\theta} = -\hat{\boldsymbol{\theta}}\frac{1}{r\sin(\theta)}\frac{\partial g\rho'}{\partial\varphi} + \hat{\boldsymbol{\varphi}}\frac{1}{r}\frac{\partial g\rho'}{\partial\theta}. \tag{3.36}$$

Considering the $\hat{\boldsymbol{\theta}}$ and $\hat{\boldsymbol{\varphi}}$ components of this equation separately, it follows that respectively the φ and θ derivatives of $\mu\nabla^4\mathcal{P} - g\rho'/r$ are zero, and therefore this combination varies in the radial direction only. Without loss of generality we may therefore seek solutions $\mathcal{P}$ that satisfy

$$\nabla^4\mathcal{P} = \frac{g\rho'}{\mu r}, \tag{3.37}$$

since for any other solution $\mathcal{P}+\mathcal{P}'$ of (3.36) we know that $\nabla^4\mathcal{P}'$ is purely radial, and therefore $\mathcal{P}'$ can be written as a sum of biharmonic solutions and a purely radial function. The biharmonic solutions are included in (3.37) and the purely radial function is discarded by (3.27).

Solutions to the biharmonic equation $\nabla^4\mathcal{P} = 0$ in 3-D are given by

$$\mathcal{P}(r,\theta,\varphi) = \sum_{l\geq 0}\sum_{m=-l}^{l}\left(A_{lm}r^l + B_{lm}r^{-l-1} + C_{lm}r^{l+2} + D_{lm}r^{-l+1}\right)Y_{lm}(\theta,\varphi), \tag{3.38}$$

where A_{lm}, B_{lm}, C_{lm}, and D_{lm} are constant coefficients, and Y_{lm} are Laplace's spherical harmonic functions of degree l and order m, which have the property that

$$\Lambda^2 Y_{lm} = -l(l+1)Y_{lm}. \tag{3.39}$$

As in 2-D, an equation for the pressure is obtained by taking the divergence of the momentum

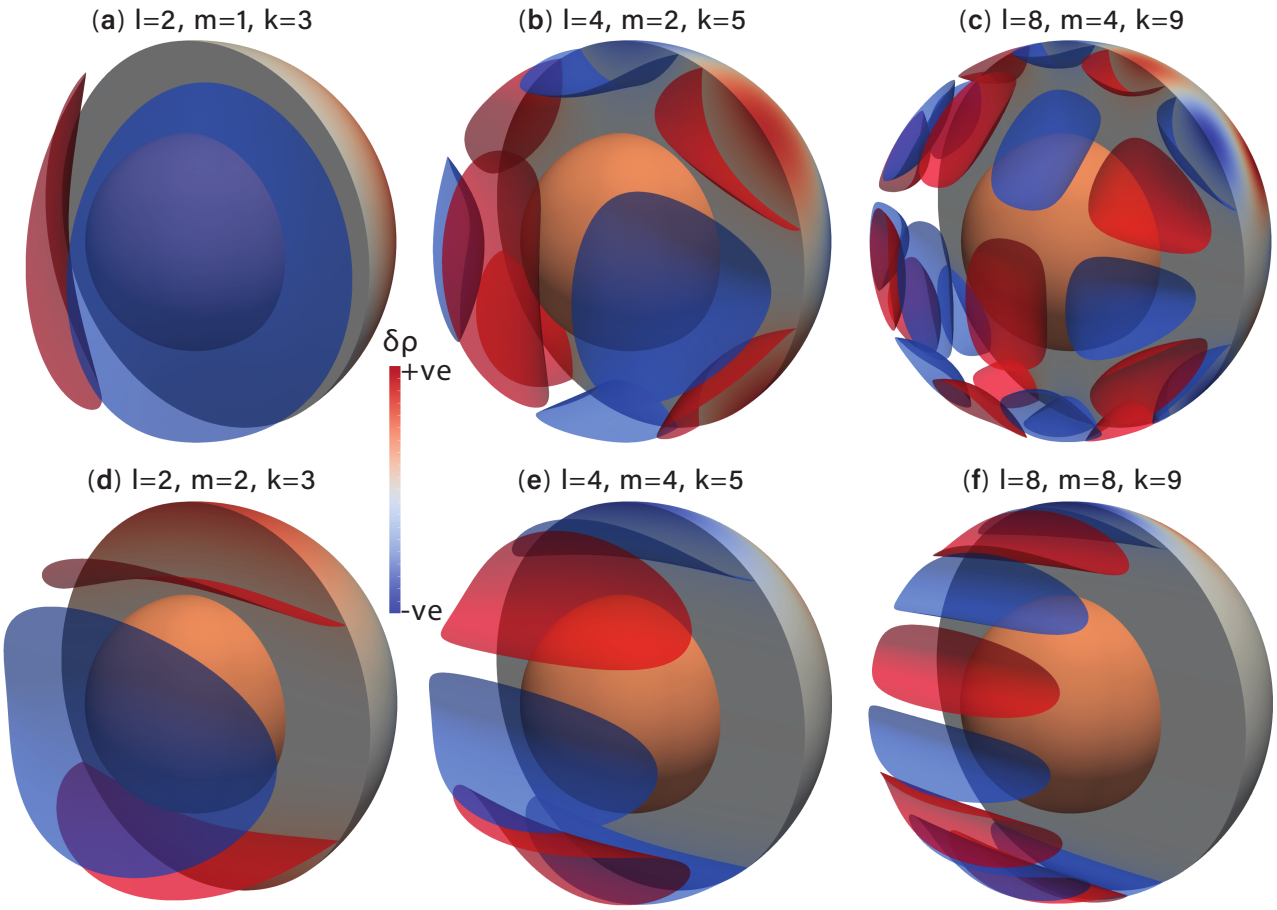


Figure 3.2: Illustrations of the density perturbation (ρ') field for smooth spherical cases across a range of l, m and k.

equation, giving

$$\nabla^2 p' = -\frac{g}{r^2}\frac{\partial}{\partial r}\left(r^2 \rho'\right). \tag{3.40}$$

Homogeneous solutions for pressure are written

$$p'(r,\theta,\varphi) = \sum_{l\geq 0}\sum_{m=-l}^{l}\left(G_{lm} r^l + H_{lm} r^{-l-1}\right) Y_{lm}(\theta,\varphi), \tag{3.41}$$

where substitution of (3.38) and (3.41) in (3.33) gives

$$G_{lm} = -2\mu(l+1)(2l+3)C_{lm}, \quad H_{lm} = -2\mu l(2l-1)D_{lm}. \tag{3.42}$$

Smooth density profile – spherical

We consider a density perturbation of the following form

$$\rho' = \frac{r^k}{R_+^k} Y_{lm}(\theta, \varphi). \tag{3.43}$$

An inhomogeneous solution of (3.37) is given by

$$\mathcal{P} = E r^{k+3} Y_{lm}, \quad E = \frac{g R_+^{-k}}{\mu \left((k+1)(k+2) - l(l+1)\right)\left((k+3)(k+4) - l(l+1)\right)} \tag{3.44}$$

with a more generic solution written as

$$\mathcal{P} = \left(A r^l + B r^{-l-1} + C r^{l+2} + D r^{-l+1} + E r^{k+3}\right) Y_{lm} \tag{3.45}$$

where we have dropped the lm subscripts of the coefficients A, B, C, D. The pressure solution for (3.40) is

$$p' = \left(G r^l + H r^{-l-1} + F r^{k+1}\right) Y_{lm}, \quad F = -\frac{g(k+2) R_+^{-k}}{(k+1)(k+2) - l(l+1)}, \tag{3.46}$$

and G and H are given by (3.42).

As before, the four coefficients A, B, C, and D are fixed by the boundary conditions

$$\textit{no-normal flow:} \qquad u_r = \frac{1}{r}\Lambda^2 \mathcal{P} = 0 \implies \mathcal{P} = 0, \qquad \text{at } r = R_\pm \tag{3.47}$$

where we use $\Lambda^2 \mathcal{P} = -l(l+1)\mathcal{P}$. The two no-normal flow conditions at $r = R_-$ and $r = R_+$ are combined with two further conditions

$$\textit{free slip:} \quad \tau_{r\theta} = \tau_{r\varphi} = 0 \implies \frac{1}{r}\Lambda^2 \mathcal{P} - \frac{\partial^2 \mathcal{P}}{\partial r^2} + \frac{2}{r^2}\mathcal{P} = 0 \implies \frac{\partial^2 \mathcal{P}}{\partial r^2} = 0, \quad \text{at } r = R_\pm, \text{ or} \tag{3.48}$$

$$\textit{zero slip:} \quad u_\theta = u_\varphi = 0 \implies \frac{\partial (r\mathcal{P})}{\partial r} = 0 \implies \frac{\partial \mathcal{P}}{\partial r} = 0, \qquad \text{at } r = R_\pm. \tag{3.49}$$

For free-slip conditions at both $r = R_-$ and $r = R_+$, the solution coefficients are given by

$$
\begin{aligned}
A &= \frac{gR_+^{-l+3}}{\mu} \frac{\alpha^{k+3} - \alpha^{-l+1}}{2\left(\alpha^{l} - \alpha^{-l+1}\right)(k+l+2)(k-l+3)(2l+1)} \\
B &= \frac{gR_+^{l+4}}{\mu} \frac{-\alpha^{k+4} + \alpha^{l+3}}{2\left(\alpha^{-l} - \alpha^{l+3}\right)(k+l+4)(k-l+1)(2l+1)} \\
C &= \frac{gR_+^{-l+1}}{\mu} \frac{\alpha^{k+4} - \alpha^{-l}}{2\left(\alpha^{-l} - \alpha^{l+3}\right)(k+l+4)(k-l+1)(2l+1)} \\
D &= \frac{gR_+^{l+2}}{\mu} \frac{-\alpha^{k+3} + \alpha^{l}}{2\left(\alpha^{l} - \alpha^{-l+1}\right)(k+l+2)(k-l+3)(2l+1)}.
\end{aligned}
$$

Zero-slip conditions at both boundaries lead to the following solution coefficients

$$
\begin{aligned}
A &= \frac{gR_+^{-l+3}}{\mu} \frac{\left(\alpha^{k+2} + \alpha^{l-1}\right)(k+l+2)(2l+3) - \left(\alpha^{k} + \alpha^{l+1}\right)(k+l+4)(2l+1) - 2\left(\alpha^{k+2l+3} + \alpha^{-l-2}\right)(k-l+1)}{\Gamma} \\
B &= \frac{gR_+^{l+4}}{\mu} \frac{\left(\alpha^{k+2l+1} + \alpha^{l+1}\right)(k-l+3)(2l+1) - \left(\alpha^{k+2l+3} + \alpha^{l-1}\right)(k-l+1)(2l-1) - 2\left(\alpha^{k+2} + \alpha^{3l}\right)(k+l+2)}{\Gamma} \\
C &= \frac{gR_+^{-l+1}}{\mu} \frac{-\left(\alpha^{k+2} + \alpha^{l-3}\right)(k+l+2)(2l+1) + \left(\alpha^{k} + \alpha^{l-1}\right)(k+l+4)(2l-1) + 2\left(\alpha^{k+2l+1} + \alpha^{-l-2}\right)(k-l+3)}{\Gamma} \\
D &= \frac{gR_+^{l+2}}{\mu} \frac{-\left(\alpha^{k+2l+1} + \alpha^{l-1}\right)(k-l+3)(2l+3) + \left(\alpha^{k+2l+3} + \alpha^{l-3}\right)(k-l+1)(2l+1) + 2\left(\alpha^{k} + \alpha^{3l}\right)(k+l+4)}{\Gamma} \\
\Gamma &= \Big(\left(\alpha^{l+1} + \alpha^{l-3}\right)(2l+1)^2 - 2\alpha^{l-1}(2l+3)(2l-1) - 4\alpha^{3l} - 4\alpha^{-l-2}\Big)(k+l+4)(k+l+2)(k-l+3)(k-l+1).
\end{aligned}
$$

Green's function solution – spherical

As in two dimensions, we find solutions for the case where

$$
\rho' = \delta(r - r')Y_{lm}(\theta, \varphi), \tag{3.50}
$$

by combining two homogeneous solutions

$$
\mathcal{P}(r,\theta,\varphi) = \begin{cases} \mathcal{P}_-(r,\theta,\varphi) = \left(A_- r^l + B_- r^{-l-1} + C_- r^{l+2} + D_- r^{-l+1}\right) Y_{lm}(\theta,\varphi) & \text{for } R_- \le r < r', \\ \mathcal{P}_+(r,\theta,\varphi) = \left(A_+ r^l + B_+ r^{-l-1} + C_+ r^{l+2} + D_+ r^{-l+1}\right) Y_{lm}(\theta,\varphi) & \text{for } r' < r \le R_+. \end{cases} \tag{3.51}
$$

The eight coefficients are found by imposing the same 4 constraints derived from the boundary conditions at $r = R_-$ and $r = R_+$ as in the previous section, and by imposing a further 4 conditions: continuity of all components of $\boldsymbol{u}$, no shear force between the two halves of the

domain, and a normal force that is proportional to the density anomaly

$$\textit{continuity of } u_r\textit{:} \qquad \mathcal{P}_-(r',\theta,\varphi) = \mathcal{P}_+(r',\theta,\varphi), \tag{3.52}$$

$$\textit{continuity of } u_\theta \textit{ and } u_\varphi\textit{:} \qquad \frac{\partial(r\mathcal{P}_-)}{\partial r}|_{r=r'} = \frac{\partial(r\mathcal{P}_+)}{\partial r}|_{r=r'} \implies \frac{\partial\mathcal{P}_-}{\partial r}(r',\theta,\varphi) = \frac{\partial\mathcal{P}_+}{\partial r}(r',\theta,\varphi), \tag{3.53}$$

$$\textit{zero-shear condition:} \qquad \frac{\partial^2\mathcal{P}_-}{\partial r^2}(r',\theta,\varphi) = \frac{\partial^2\mathcal{P}_+}{\partial r^2}(r',\theta,\varphi), \tag{3.54}$$

$$\textit{normal-shear condition:} \qquad \frac{\partial^3\mathcal{P}_+}{\partial r^3}(r',\theta,\varphi) - \frac{\partial^3\mathcal{P}_-}{\partial r^3}(r',\theta,\varphi) = \frac{gY_{lm}(\theta,\varphi)}{\mu r'}, \tag{3.55}$$

where (3.55) is derived from (3.37) in the same way as (3.26), and (3.53)–(3.55) assume (3.52).

The free-slip solution coefficients are given by

$$\begin{aligned}
A_\pm &= \frac{gr'^{-l+2}}{\mu}\frac{\pm\left(\alpha_\mp^{2l-1}-1\right)}{2\left(\alpha_\pm^{2l-1}-\alpha_\mp^{2l-1}\right)(2l-1)(2l+1)}\\
B_\pm &= \frac{gr'^{l+3}}{\mu}\frac{\pm\left(\alpha_\mp^{-2l-3}-1\right)}{2\left(\alpha_\pm^{-2l-3}-\alpha_\mp^{-2l-3}\right)(2l+1)(2l+3)}\\
C_\pm &= \frac{gr'^{-l}}{\mu}\frac{\pm\left(-\alpha_\mp^{2l+3}+1\right)}{2\left(\alpha_\pm^{2l+3}-\alpha_\mp^{2l+3}\right)(2l+1)(2l+3)}\\
D_\pm &= \frac{gr'^{l+1}}{\mu}\frac{\pm\left(-\alpha_\mp^{-2l+1}+1\right)}{2\left(\alpha_\pm^{-2l+1}-\alpha_\mp^{-2l+1}\right)(2l-1)(2l+1)}.
\end{aligned}$$

The zero-slip solution coefficients are given by

$$\begin{aligned}
A_\pm &= \frac{gr'^{-l+2}}{\mu}\frac{\alpha_+^2-\alpha_-^2+\frac{2}{2l+1}\left(\alpha_+^{-2l-1}-\alpha_-^{-2l-1}\right)\pm\frac{2l+3}{2l+1}+\frac{2}{2l-1}\left(\alpha_+^2\alpha_-^{-2l-1}-\alpha_+^{-2l-1}\alpha_-^2\right)\pm\frac{4\gamma^{\pm(2l+1)}}{(2l-1)(2l+1)}\mp\frac{\gamma^{\mp2}(2l+1)}{2l-1}}{-8\gamma^{-2l-1}-8\gamma^{2l+1}+2\left(\gamma^2+\gamma^{-2}\right)(2l+1)^2-4(2l-1)(2l+3)}\\
B_\pm &= \frac{gr'^{l+3}}{\mu}\frac{\alpha_+^2-\alpha_-^2-\frac{2}{2l+1}\left(\alpha_+^{2l+1}-\alpha_-^{2l+1}\right)\pm\frac{2l-1}{2l+1}-\frac{2}{2l+3}\left(\alpha_+^2\alpha_-^{2l+1}-\alpha_+^{2l+1}\alpha_-^2\right)\pm\frac{4\gamma^{\mp(2l+1)}}{(2l+1)(2l+3)}\mp\frac{\gamma^{\mp2}(2l+1)}{2l+3}}{-8\gamma^{-2l-1}-8\gamma^{2l+1}+2\left(\gamma^2+\gamma^{-2}\right)(2l+1)^2-4(2l-1)(2l+3)}\\
C_\pm &= \frac{gr'^{-l}}{\mu}\frac{\alpha_-^{-2}-\alpha_+^{-2}+\frac{2}{2l+1}\left(\alpha_+^{-2l-1}-\alpha_-^{-2l-1}\right)\mp\frac{2l-1}{2l+1}+\frac{2}{2l+3}\left(\alpha_+^{-2}\alpha_-^{-2l-1}-\alpha_+^{-2l-1}\alpha_-^{-2}\right)\mp\frac{4\gamma^{\pm(2l+1)}}{(2l+1)(2l+3)}\pm\frac{\gamma^{\pm2}(2l+1)}{2l+3}}{-8\gamma^{-2l-1}-8\gamma^{2l+1}+2\left(\gamma^2+\gamma^{-2}\right)(2l+1)^2-4(2l-1)(2l+3)}\\
D_\pm &= \frac{gr'^{l+1}}{\mu}\frac{\alpha_-^{-2}-\alpha_+^{-2}-\frac{2}{2l+1}\left(\alpha_+^{2l+1}-\alpha_-^{2l+1}\right)\mp\frac{2l+3}{2l+1}-\frac{2}{2l-1}\left(\alpha_+^{-2}\alpha_-^{2l+1}-\alpha_+^{2l+1}\alpha_-^{-2}\right)\mp\frac{4\gamma^{\mp(2l+1)}}{(2l-1)(2l+1)}\pm\frac{\gamma^{\pm2}(2l+1)}{2l-1}}{-8\gamma^{-2l-1}-8\gamma^{2l+1}+2\left(\gamma^2+\gamma^{-2}\right)(2l+1)^2-4(2l-1)(2l+3)}.
\end{aligned}$$

3.3 Numerical Discretisation in Fluidity

The test cases in the previous section have been examined using Fluidity, a finite element, control-volume computational modelling framework (Davies et al., 2011; Kramer et al., 2012).

3.3.1 Discretisation

The numerical solutions for velocity and pressure, $\boldsymbol{u}$ and p', are written as a linear combination of basis functions N_j and M_l

$$\boldsymbol{u} = \sum_j \boldsymbol{u}_j N_j, \quad p' = \sum_l p_l M_l. \tag{3.56}$$

Note that compared with (2.13) in the previous chapter, here we use scalar-valued basis functions N_j with vector-valued coefficients $\boldsymbol{u}_j$, i.e. for each j we have 2 or 3 (depending on the dimension of the domain) degrees of freedom, instead of vector valued basis functions $\boldsymbol{N}_b$ with scalar valued coefficients u_b. The latter is a more general way of expanding the velocity function space, whereas in this chapter, for simplicity, we assume that the velocity function space can be decomposed as the direct sum of the same scalar function space associated with each velocity component independently.

We use either the P2-P1 (Taylor Hood) or $\mathrm{P2_{bubble}}$-$\mathrm{P1_{DG}}$ element pairs. In both cases the velocity and pressure basis functions N_j and M_l are piecewise quadratic and linear respectively on a triangular (2-D) or tetrahedral (3-D) mesh of the domain Ω. Because the curved boundaries of the cylindrical and spherical-shell domains can only be approximated by the mesh, the numerical domain is denoted by Ω_h. When using the P2-P1 element pair the basis functions are continuous between cells. For the $\mathrm{P2_{bubble}}$-$\mathrm{P1_{DG}}$ element pair the piecewise linear pressure is treated as discontinuous between cells and the continuous quadratic velocity basis functions are enriched by an extra cubic "bubble" function with a corresponding cell-centred degree of freedom (Ern et al., 2004; Boffi et al., 2013).

The Stokes equations are written in the weak form, using the same N_j and M_l basis as test-

functions. After integrating by parts (3.1) and (3.3) then become (omitting boundary terms)

$$\int_{\Omega_h} \mu \left(\nabla N_i\right) \cdot \sum_j \left[\nabla N_j^T \boldsymbol{u}_j + \boldsymbol{u}_j^T \nabla N_j\right] + N_i \sum_l p_l \nabla M_l = -\int_{\Omega_h} N_i g \rho' \hat{\boldsymbol{r}} \quad \text{for all } N_i, \tag{3.57}$$

$$\int_{\Omega_h} \left(\nabla M_k\right) \cdot \sum_j \boldsymbol{u}_j N_j = 0 \quad \text{for all } M_k. \tag{3.58}$$

Note that we apply strong Dirichlet boundary conditions, so that the boundary integrals can indeed be neglected. In the free-slip case, a local rotation is applied to the velocity vectors, so that the degrees of freedom correspond to velocity components in either the normal or tangential directions. This allows us to enforce a zero normal component, while leaving the tangential components free. For additional details about Fluidity and its implementation see Davies et al. (2011).

3.3.2 Isoparametric representation of the domain

For an accurate representation of the quadratic approximation of velocity, we need to also approximate the curved cylindrical/spherical domain quadratically. This means that rather than each cell in the mesh being described by a linear map $X_{\text{lin}} : \xi \mapsto X_{\text{lin}}(\xi)$ from local coordinates ξ in a reference element to physical coordinates X, we use a quadratic map $X_{\text{quad}}(\xi)$, which maps to a curved triangle/tetrahedron that better represents the domain. This map can be obtained from a linear mesh with coordinate mappings, X_{lin}, through quadratic interpolation

$$X_{\text{quad}}(\xi) \overset{\text{quad. interp.}}{\approx} \frac{r_{\text{lin}}(\xi)}{\|X_{\text{lin}}(\xi)\|} X_{\text{lin}}(\xi), \tag{3.59}$$

at the standard Lagrange nodes of the quadratic function space. Here $r_{\text{lin}}(\xi)$ is the linear interpolation of the radius, i.e. $r_{\text{lin}} = \|X_{\text{lin}}\|$ at the vertices of the linear mesh. This particular choice ensures that for an equal-radius boundary, with the boundary vertices of the linear mesh exactly on the boundary, the quadratic Lagrange nodes also lie exactly on this boundary.

3.3.3 Forcing term

The density perturbation ρ' on the RHS of (3.57) is a prescribed analytical expression in each of the test cases. For the Green's function solutions in 2-D and 3-D, using (3.20) and (3.50) respectively, we get

$$-\int_{\Omega_h} N_i g\rho'\hat{\boldsymbol{r}} = -\int_{\Omega_h} N_i(r,\theta) g\cos(n\theta)\delta(r-r')\hat{\boldsymbol{r}} = -\int_{\Gamma'} N_i(r,\theta) g\cos(n\theta)\boldsymbol{n}, \tag{3.60}$$

$$-\int_{\Omega_h} N_i(r,\theta) g\rho'\hat{\boldsymbol{r}} = -\int_{\Omega_h} N_i(r,\theta,\varphi) gY_{lm}(\theta,\varphi)\delta(r-r')\hat{\boldsymbol{r}} = -\int_{\Gamma'} N_i(r,\theta,\varphi) gY_{lm}(\theta,\varphi)\boldsymbol{n}, \tag{3.61}$$

where Γ' is an internal boundary at $r = r'$ oriented such that its normal $\boldsymbol{n} = \hat{\boldsymbol{r}}$ points outwards.

3.3.4 Solving the linear system and dealing with nullspaces

Equations (3.57) and (3.58) form a saddle point linear system which is solved by applying a Schur decomposition technique where the outer iteration, which solves for the pressure degrees of freedom, is solved with a flexible Krylov subspace method, `FGMRES`. The inner solve associated with the velocity degrees of freedom, is solved with the Conjugate Gradient method preconditioned with an algebraic multigrid method (`GAMG` available through PETSc: Balay et al., 1997).

In all cases, the pressure solution is only defined up to an arbitrary constant. The analytical pressure solution has the property that its mean is zero. For comparative purposes we therefore subtract the volume averaged pressure from the obtained numerical pressure solution

$$p' \to p' - \frac{\int_{\Omega_h} p'}{\int_{\Omega_h} 1}. \tag{3.62}$$

Similarly, for free-slip cases, in 2-D, we may add an arbitrary rotation of the form $(-y, x) = r\hat{\boldsymbol{\theta}}$

to the velocity solution. We therefore apply the following projection to the numerical solution

$$\boldsymbol{u} \to \boldsymbol{u} - \frac{\int_{\Omega_h} r\hat{\boldsymbol{\theta}} \cdot \boldsymbol{u}}{\int_{\Omega_h} r^2} r\hat{\boldsymbol{\theta}}, \tag{3.63}$$

which ensures that the angular momentum $\int r\hat{\boldsymbol{\theta}} \cdot \boldsymbol{u}$ is zero, as it is for the analytical solutions. In the same way, in three dimensions we subtract the three rotational (rigid body) modes.

It should be noted that the same velocity and pressure modes lead to zero modes (eigenvectors) for the linear system based on (3.57) and (3.58), rendering the resulting matrix singular. In preconditioned Krylov methods we typically need to subtract the zero modes from the approximate solution at every iteration. With iterative approximation $\boldsymbol{x}^i$ and zero eigenvector $\boldsymbol{\lambda}$ we get

$$\boldsymbol{x}^i \to \boldsymbol{x}^i - \langle \boldsymbol{\lambda}, \boldsymbol{x}^i \rangle \boldsymbol{\lambda}. \tag{3.64}$$

This l_2-projection, based on the l_2 inner product $\langle \cdot, \cdot \rangle$ between the discrete solution vectors, is analogous but not equivalent to the projections in (3.62) and (3.63) which are L_2-projections based on integrals. Therefore, despite the l_2 projections fixing the nullmodes during the iterative solve, the L_2-projections should be applied as an additional step after the iterative solvers have completed to ensure convergence to the analytical solution.

3.4 Convergence Results

In this section we show the convergence of the numerical solutions obtained with Fluidity, using the P2-P1 element pair, towards the analytical solutions. For 2-D cylindrical cases, the series of meshes start at refinement level 1, where the mesh consists of 128 divisions in the horizontal, and 16 layers, giving $128 \times 16 \times 2 = 4096$ triangles. At each subsequent level the mesh is refined, doubling the resolution in both directions. For the spherical cases, the mesh at refinement level 1 is obtained from an icosahedron refined three times, starting with 1280 triangles in the horizontal, which is extruded radially to 16 layers, giving a 3-D mesh consisting of 61440 tetrahedra. Again, resolution is doubled in all directions for subsequent refinement

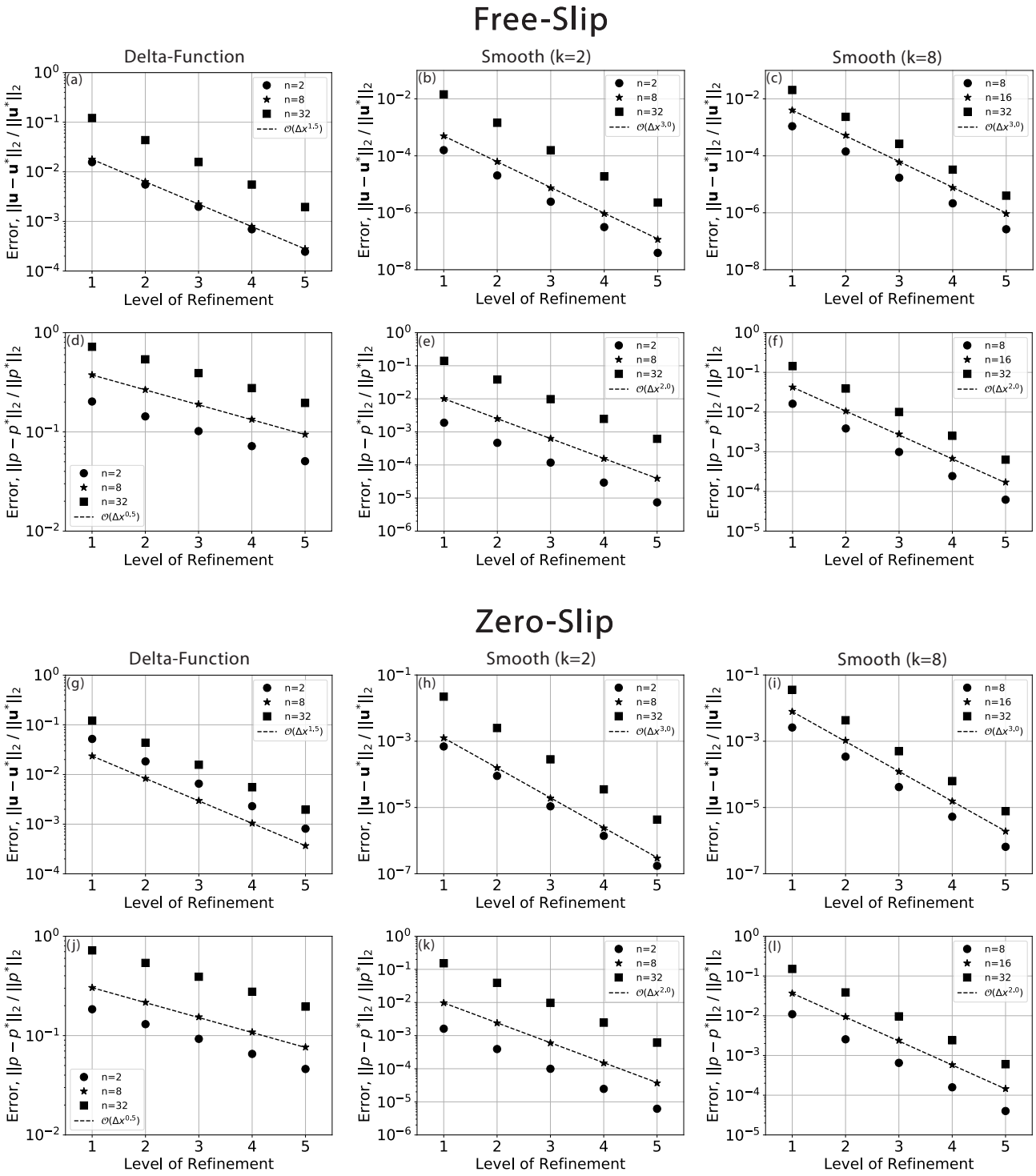


Figure 3.3: Convergence for 2-D cylindrical cases with free-slip and zero-slip boundary conditions, at a series of different wavenumbers, n, as indicated in the legend. Note that cases with a smooth forcing are run at $k = 2$ and $k = 8$, as indicated. Convergence rate is indicated by dashed lines, with the order of convergence provided in the legend.

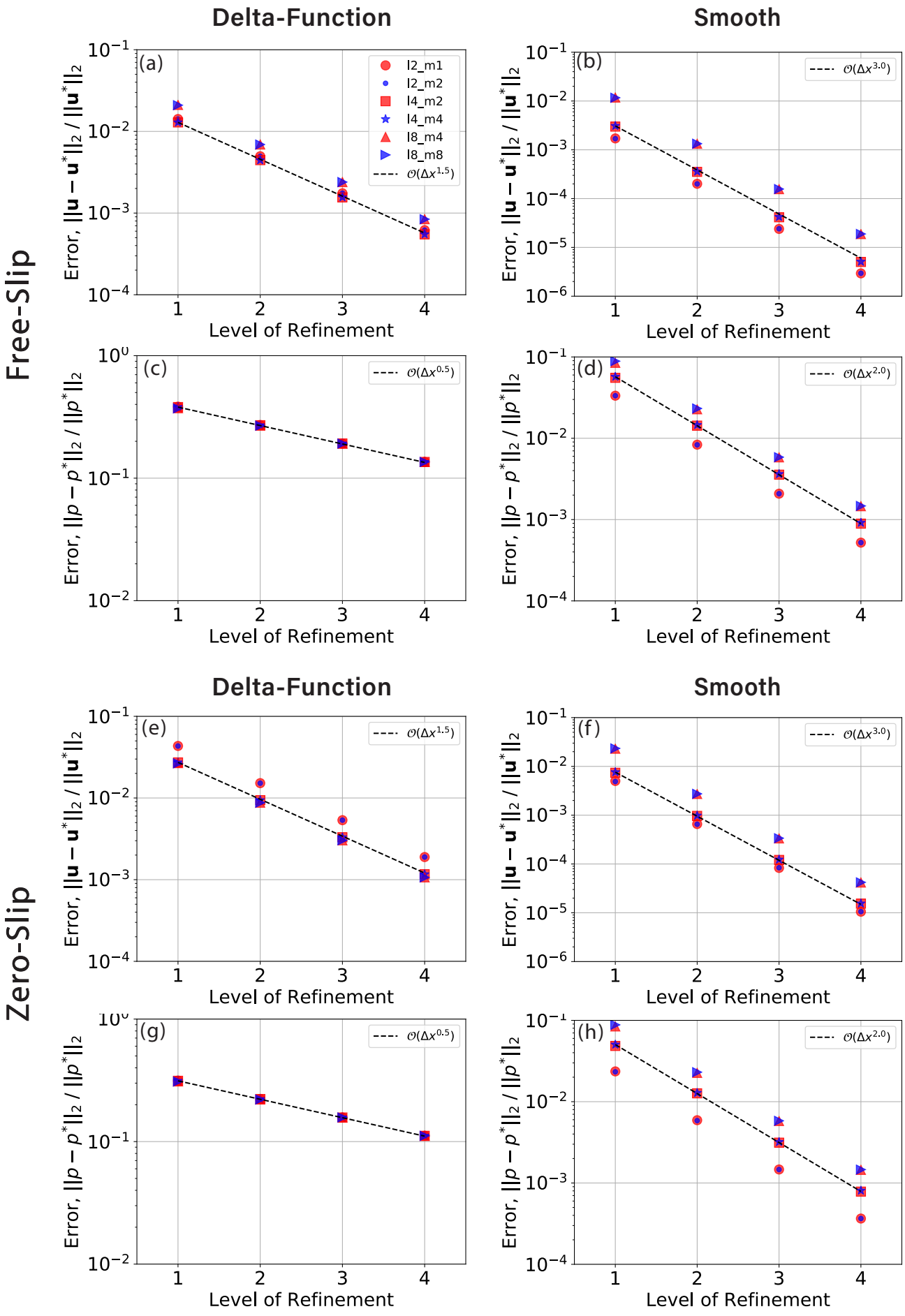


Figure 3.4: Convergence of velocity and pressure for 3-D spherical cases with free-slip and zero-slip boundary conditions, at a range of degrees l and orders m. Note that all cases with a smooth forcing are run at $k = l + 1$.

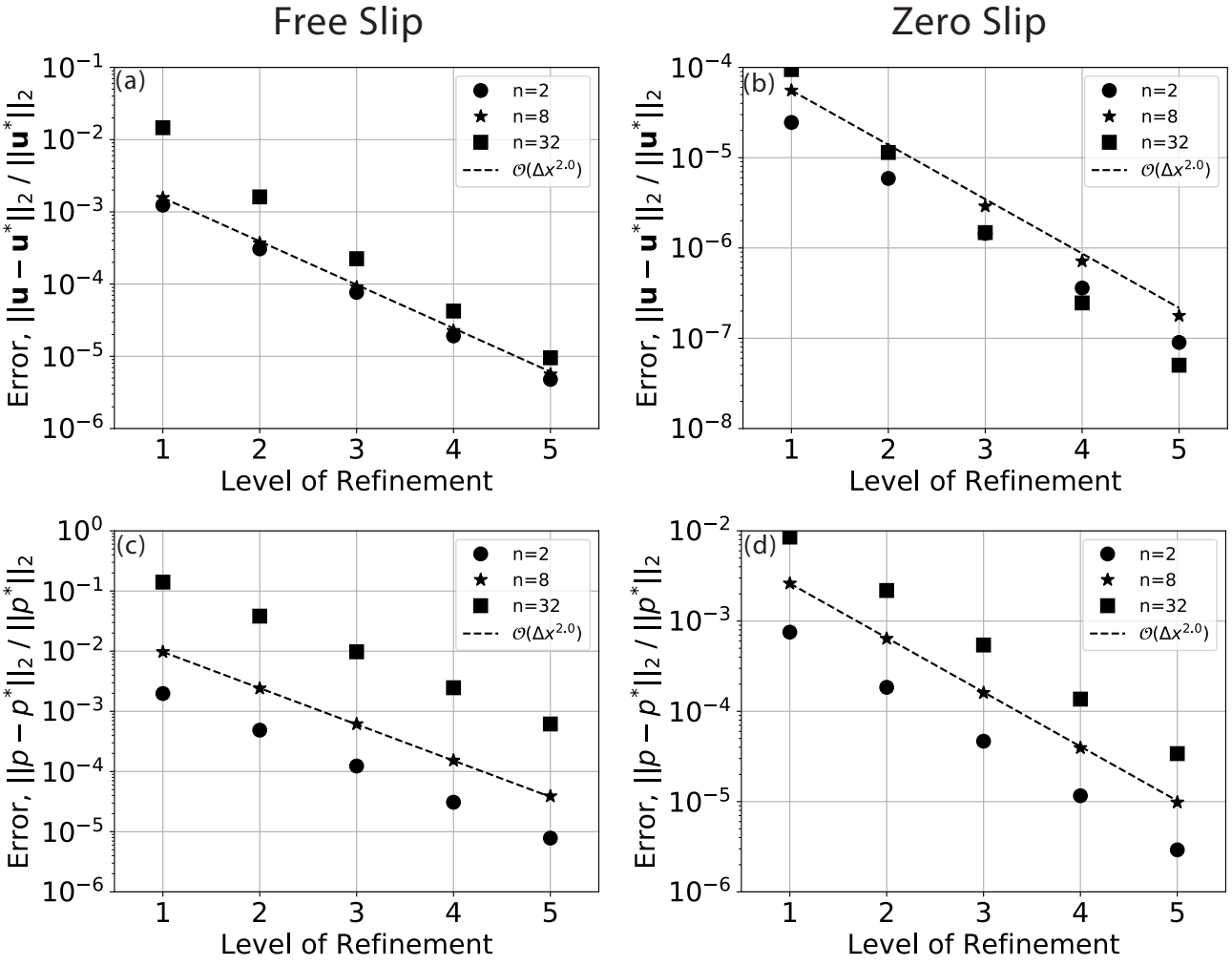


Figure 3.5: Convergence of velocity (a, b) and pressure (c, d), respectively, for smooth ($k = 2$) 2-D cylindrical cases with free-slip and zero-slip boundary conditions. Note that these cases do not incorporate an isoparametric approximation of the domain, hence the reduced convergence relative to comparable cases in Fig. 3.3.

levels. In all cases non-dimensionalised coordinates were used with $R_- = 1.22$ and $R_+ = 2.22$, and the delta-function cases used $r' = (R_- + R_+)/2$. This choice of r' ensures the density anomaly coincides with a grid layer at all mesh resolutions considered herein.

In all figures, errors are given as relative errors, comparing the numerical solution, $\boldsymbol{u}$ and p', with the analytical solutions, $\boldsymbol{u}^*$ and p'^* (interpolated node-wise into the P2 and P1 function spaces respectively) in the L_2-norm

$$\frac{\|\boldsymbol{u} - \boldsymbol{u}^*\|_2}{\|\boldsymbol{u}^*\|_2} = \frac{\sqrt{\int_{\Omega_h} |\boldsymbol{u} - \boldsymbol{u}^*|^2}}{\sqrt{\int_{\Omega_h} |\boldsymbol{u}^*|^2}}, \quad \frac{\|p' - p'^*\|_2}{\|p'^*\|_2} = \frac{\sqrt{\int_{\Omega_h} (p' - p'^*)^2}}{\sqrt{\int_{\Omega_h} (p'^*)^2}}. \tag{3.65}$$

Convergence plots for the 2-D cylindrical cases are presented in Fig. 3.3. With a smooth density profile we see optimal convergence for the P2-P1 element pair at third and second order for velocity and pressure respectively, with both free-slip and zero-slip boundary conditions. Cases with lower wave-number n show smaller relative error than those at higher n, as expected. The same observation holds for lower and higher polynomial order, $k = 2$ and $k = 8$, for the radial density profile. For the free-slip and zero-slip delta-function cases however, convergence drops to 1.5 and 0.5 for velocity and pressure respectively. Furthermore, cases with lower n do not consistently show smaller relative error than those at higher n.

We see similar results for the spherical results illustrated in Fig. 3.4: third and second order for velocity and pressure for the cases with a smooth density profile, with smaller relative errors for lower wave numbers l and m. Note that here, the smooth vertical profile for density uses $k = l + 1$ in all cases. Again, for cases with a delta-function density anomaly, we observe a reduced order of convergence of 1.5 and 0.5 for velocity and pressure, respectively.

To examine the importance of an isoparametric approximation of the domain by a quadratic mesh, we ran the same cases with a linear mesh. The results are shown in Fig. 3.5 which demonstrates that the order of convergence of velocity in the smooth cylindrical cases is indeed limited to second order. The convergence of pressure remains at second order.

3.5 Discussion

3.5.1 Existing analytical benchmarks in shell domains

As indicated in the introduction, spherical delta-function cases, like those presented herein, have previously been used to validate global mantle convection codes (e.g. Zhong et al., 2008a; Burstedde et al., 2013; Davies et al., 2013; Liu et al., 2019). These will be discussed in more detail in the following section.

The derivation for all 3-D cases in this paper rely on the Mie representation that decomposes the velocity solution into poloidal and toroidal components, through which, under the assumption of purely poloidal flow, the Stokes equations can be reduced to a biharmonic equation (3.10). Any solution to the inhomogeneous solution can then be combined with four linearly independent homogeneous solutions to this equation, the coefficients of which can be derived through the imposition of boundary conditions. For the smooth case with a generic monomial forcing term, the same decomposition (i.e. (3.45) and (3.44)), was used in Tosi et al. (2007) to derive the analytical solution for Stokes flow in two eccentrically nested spheres.

In Horbach et al. (2020) similar techniques were employed to derive benchmarks in spherical-shell domains that satisfy zero-slip and free-slip conditions and, in addition, a mixed zero-slip/free-slip case. Here the derivation starts by simply selecting four, in principle arbitrary, linearly independent solutions for the radially-dependent part of the poloidal scalar function. Again the imposition of boundary conditions fixes the coefficients of this linear combination. The corresponding right-hand side forcing term is then obtained by substitution.

The number of published benchmarks for 2-D cylindrical shell domains is more limited (e.g. Buffa et al., 2011; Blinova et al., 2016; Hoang et al., 2017). The derivation of the equivalent cases in 2-D cylindrical shell domains is somewhat simpler, but also ultimately relies on combining four independent homogeneous solutions and one inhomogeneous solution to a biharmonic equation.

In Blinova et al. (2016) analytical solutions in both cylindrical and spherical domains are pre-

sented for the Stokes equations with a radially-dependent viscosity. Because these are solutions in cylindrical or spherical coordinates without reference to any specific domain, they do not satisfy no-normal flow conditions on the boundary of a shell domain. They can be used in such domains as a numerical benchmark by specifying all velocity components of the analytical solution as a Dirichlet condition for the model. Analytical solutions for radially-dependent viscosity were also presented in Thieulot (2017). Their solutions (in 3-D only) do satisfy no-normal flow conditions in a spherical-shell domain, but the tangential components are non-zero at the boundary, and thus still require inhomogeneous Dirichlet conditions. Spatially varying viscosity is of course an important aspect of mantle convection models for which these are effective benchmarks. The isoviscous solutions presented here, and those in Horbach et al. (2020), however, allow for the testing of zero-slip and free-slip conditions, where in particular free-slip conditions may pose various numerical challenges such as rotational modes, and, depending on the discretisation used, the (non-)alignment of velocity components with normal and tangential directions at the boundary.

3.5.2 Reduced order of convergence with discontinuous pressures

At first sight, the reduced order of convergence for the delta-function cases seems at odds with those expected for the P2-P1 element pair. However the mathematical proofs for the ideal order of convergence to solutions of the Stokes equations rely on certain regularity assumptions of the right-hand side forcing term and, related to that, on the regularity of the velocity and pressure solutions. The regularity of the delta function can be classified as being a member of the Sobolev space $H^{-1}(\Omega)$ the dual of the Sobolev space $H^1(\Omega)$, where for the sake of simplicity we assume $\Omega = \Omega_h$ in this section. This means that the delta function can be thought of as a continuous function

$$\delta_{r'} : v \mapsto \int_\Omega \delta(r - r')v(r, \varphi) r dr d\varphi = \int_\Omega v(r')r' d\varphi, \tag{3.66}$$

which maps functions $v \in H^1(\Omega)$, the space of square integrable functions with square integrable weak derivatives, to $\mathbb{R}$. Girault et al. (2012) demonstrate that even with the very loose regularity

condition that the right-hand side f is in $H^m(\Omega)$ with $m \geq -1$, the Stokes equations in the weak form have a unique solution (given sufficient integral constraints) with velocity in $H^{m+2}(\Omega)$ and pressure in $H^{m+1}(\Omega)$. The analytical solutions derived here for the delta-case with $m = -1$, indeed have a discontinuous pressure in $H^0(\Omega) = L_2(\Omega)$, and a velocity with discontinuous normal derivative in $H^1(\Omega)$.

For velocity-pressure finite element pairs that satisfy the standard inf-sup, or Ladyzhenskaya-Babuška-Brezzi (LBB) condition (e.g. Boffi et al., 2013)

$$\sup_{\boldsymbol{v} \in V} \frac{\int_\Omega \boldsymbol{v} \cdot \nabla q}{\|\boldsymbol{v}\|_1} \geq \beta \|q\|_2 \text{ for all } q \in W, \tag{3.67}$$

where V and W are the discrete vector and scalar function spaces respectively, and β is a constant, it can be shown that the method converges and in fact

$$|\boldsymbol{u}^* - \boldsymbol{u}|_1 + \|p'^* - p'\|_2 \leq C_1 \left\{ \inf_{\boldsymbol{v} \in V} |\boldsymbol{u}^* - \boldsymbol{v}|_1 + \inf_{q \in W} \|p'^* - q\|_2 \right\}, \tag{3.68}$$

where C_1 is a constant independent of h, $\boldsymbol{u}^*$ and p'^* are the exact solutions, $\boldsymbol{u}$ and p' the numerical solutions in the discrete function spaces V and W based on a mesh with mesh distance h, and $|\cdot|_1$ is the semi-norm

$$|\boldsymbol{u}|_1 = \sqrt{\sum_{i=1}^{\dim} \int_\Omega \|\partial_i \boldsymbol{u}\|^2}. \tag{3.69}$$

In other words, the convergence of $\boldsymbol{u}$ and p' to $\boldsymbol{u}^*$ and p'^* is bounded by the best possible approximation of $\boldsymbol{u}^*$ and p'^* in the discrete spaces V and W. For bounded functions with a discontinuity along a smooth interface, such as our analytical pressure solution p'^*, the best approximation by continuous, piecewise-linear polynomials, i.e. $W = \mathrm{P1}$, is bounded by

$$\inf_{q \in W} \|p'^* - q\|_2 \leq C_2 h^{\frac{1}{2}} \|p'^*\|_2, \tag{3.70}$$

(this bound can be derived from the order of convergence results in Bernardi, 1989). This

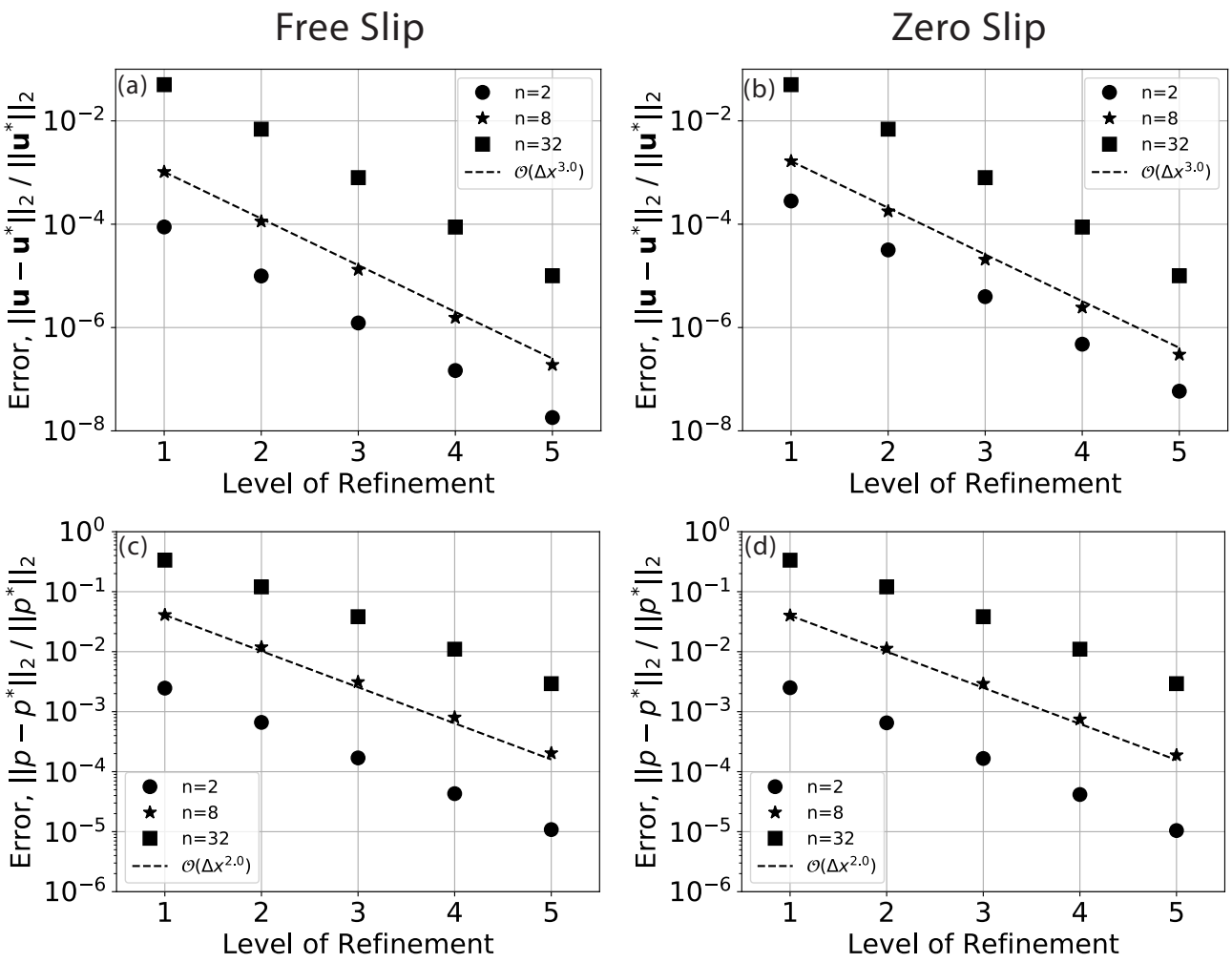


Figure 3.6: Convergence of velocity (a, b) and pressure (c, d), respectively, for delta-function 2-D cylindrical cases with free-slip and zero-slip boundary conditions with the $\mathrm{P2_{bubble}}$-$\mathrm{P1_{DG}}$ element pair.

therefore limits the convergence of the method.

A solution to this problem is found by allowing for discontinuities in the discrete pressure space. We demonstrate this here by considering $W = \mathrm{P1_{DG}}$ the space of piecewise linear but discontinuous functions. To satisfy the inf-sup condition this requires enriching the quadratic function space P_2 for velocity with a cubic bubble (Ern et al., 2004; Boffi et al., 2013). Convergence results for this element pair are shown in Fig. 3.6. For the 2-D cylindrical delta-function cases, we observe the expected orders of convergence: third order for velocity and second order for pressure.

Finally, we compare our results with those presented in Zhong et al. (2008a), Davies et al. (2013), Burstedde et al. (2013) and Liu et al. (2019), who ran the same spherical cases with

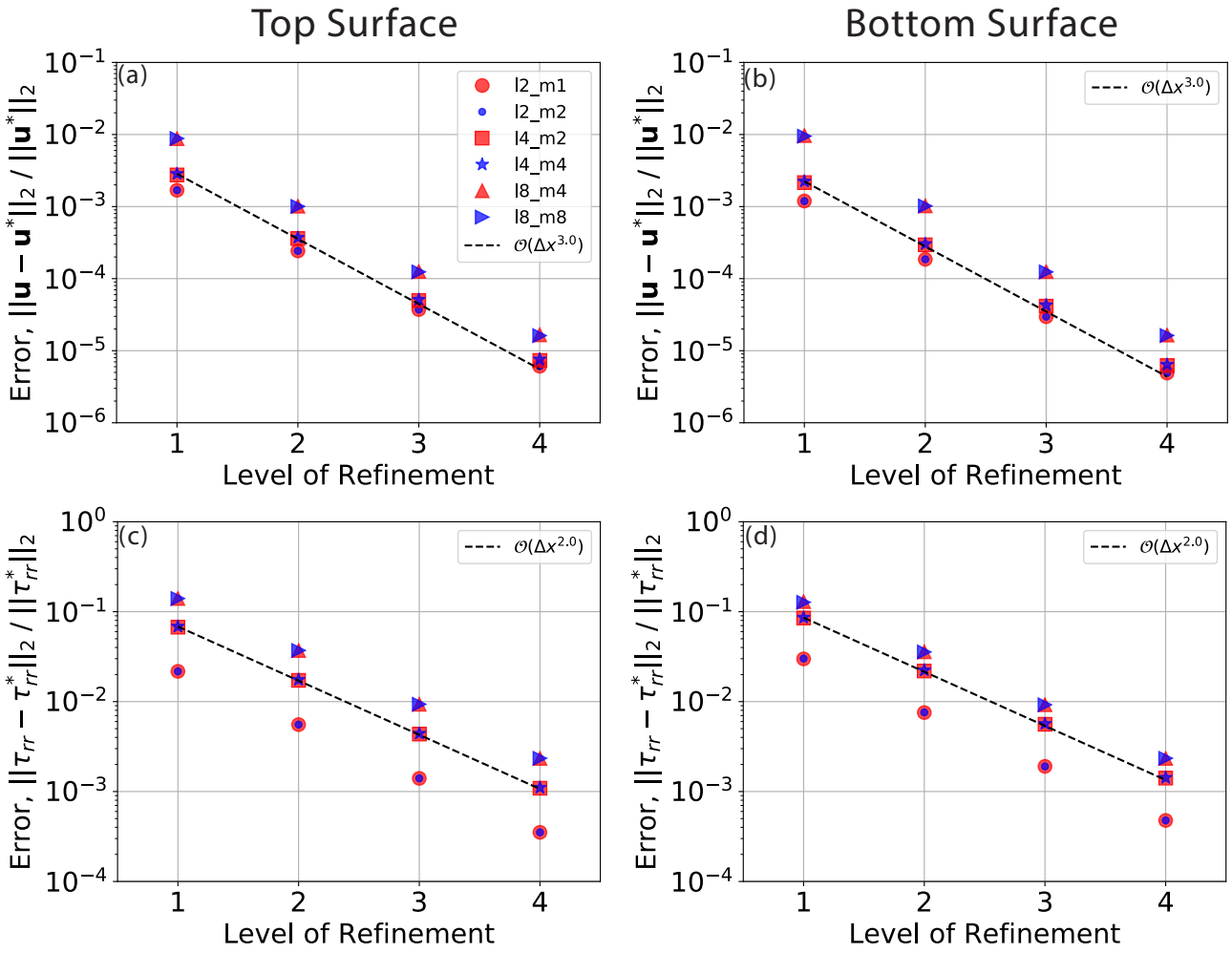


Figure 3.7: Convergence of velocity and radial stresses at top (a, c) top and (b, d) bottom surfaces ($r = R_{\pm}$), respectively, for delta-function 3-D spherical cases with free-slip boundary conditions.

a delta function forcing, and found second order convergence for velocity and second order convergence for pressure related diagnostics. It should be noted, however, that these studies only examined surface diagnostics, such as the velocity divergence and the normal stress. When we examine comparable diagnostics, specifically, the relative error in velocity at the boundary and the boundary normal stress (illustrated in Fig. 3.7), we find velocity convergence at third order and normal stress at second order. It therefore appears that the reduced order of accuracy in the interior of the domain does not affect the surface response which still converges at the same order as for the smooth case.

The results of Zhong et al. (2008a) (using CitcomS) and Davies et al. (2013) (using TERRA) were based on a Q1-P0 discretisation with a continuous piecewise trilinear velocity and piecewise constant, discontinuous pressure. Although our analysis above limits the convergence of $\|p' - p'^*\|_2$ for a P0 pressure p' to first order, second order super-convergence can be obtained in some cases by evaluating the analytical solution only in the cell centre. In other words, by comparing to a filtered piecewise constant analytical approximation $\bar{p}'^*$, second order convergence can sometimes be observed in $\|p' - \bar{p}'^*\|_2$. For continuous pressure approximations, such as the P2-P1 results in this thesis, the Q1-Q1 discretisation of the Rhea model in Burstedde et al. (2013), and the Q2-Q1 discretisation of ASPECT in Liu et al. (2019), reduced convergence in the interior of the domain is to be expected.

3.6 Conclusions

We have presented a series of 2-D cylindrical and 3-D spherical analytical solutions for the purpose of verifying mantle dynamics codes. These solutions are based upon either a delta-function density perturbation or a smooth forcing term, and we provide solutions for both free-slip and zero-slip boundary conditions. The combinations of dimension, forcing and boundary conditions, provide a series of eight analytical solutions that can be used as a basis for validating existing and future numerical codes, in cylindrical and spherical geometries. To facilitate this, we provide solutions in the form of a python package, Assess (*Analytical Solutions for the Stokes*

Equations in Spherical Shells; Kramer, 2020).

We verify the convergence of the P2-P1 (Taylor Hood) finite element discretisation using Fluidity (Davies et al., 2011; Kramer et al., 2012). The continuous approximation of pressure can lead to a reduced order of convergence in the presence of discontinuities, which can be overcome using a discontinuous numerical approximation of pressure. It is important to note that this reduced order of convergence was only observed by comparing the numerical solution with the entire analytical solution in the interior of the domain. A comparison based on surface response only failed to highlight this issue.

3.7 Equations in polar coordinates

For completeness, in this final section we work out the incompressible Stokes equations in polar coordinates in terms of a streamfunction ψ, where the components of velocity are given by

$$u_r = -\frac{1}{r}\frac{\partial \psi}{\partial \varphi}, \quad u_\varphi = \frac{\partial \psi}{\partial r}, \tag{3.71}$$

We make use of the following expressions for the derivatives of the unit vectors $\hat{\boldsymbol{r}}$ and $\hat{\boldsymbol{\varphi}}$ with respect to r and φ

$$\hat{\boldsymbol{r}} \cdot \nabla \hat{\boldsymbol{r}} = \frac{\partial \hat{\boldsymbol{r}}}{\partial r} = 0, \qquad \hat{\boldsymbol{\varphi}} \cdot \nabla \hat{\boldsymbol{r}} = \frac{1}{r}\frac{\partial \hat{\boldsymbol{r}}}{\partial \varphi} = \frac{1}{r}\hat{\boldsymbol{\varphi}}, \tag{3.72}$$

$$\hat{\boldsymbol{r}} \cdot \nabla \hat{\boldsymbol{\varphi}} = \frac{\partial \hat{\boldsymbol{\varphi}}}{\partial r} = 0, \qquad \hat{\boldsymbol{\varphi}} \cdot \nabla \hat{\boldsymbol{\varphi}} = \frac{1}{r}\frac{\partial \hat{\boldsymbol{\varphi}}}{\partial \varphi} = -\frac{1}{r}\hat{\boldsymbol{r}}. \tag{3.73}$$

Using these we can work out the different components of stress

$$\tau_{rr} = 2\mu\hat{\boldsymbol{r}} \cdot [\nabla \boldsymbol{u}] \cdot \hat{\boldsymbol{r}} = 2\mu\hat{\boldsymbol{r}} \cdot \nabla (\hat{\boldsymbol{r}} \cdot \boldsymbol{u}) - 2\mu (\hat{\boldsymbol{r}} \cdot \nabla\hat{\boldsymbol{r}}) \cdot \boldsymbol{u} = 2\mu\frac{\partial u_r}{\partial r} - 0 = -2\mu\frac{\partial}{\partial r}\left(\frac{1}{r}\frac{\partial\psi}{\partial\varphi}\right), \tag{3.74}$$

$$\begin{aligned}\tau_{\varphi\varphi} = 2\mu\hat{\boldsymbol{\varphi}} \cdot [\nabla \boldsymbol{u}] \cdot \hat{\boldsymbol{\varphi}} = 2\mu\hat{\boldsymbol{\varphi}} \cdot \nabla (\hat{\boldsymbol{\varphi}} \cdot \boldsymbol{u}) - 2\mu (\hat{\boldsymbol{\varphi}} \cdot \nabla\hat{\boldsymbol{\varphi}})\, \boldsymbol{u} &= \frac{2\mu}{r}\frac{\partial u_\varphi}{\partial\varphi} + \frac{2\mu}{r}\hat{\boldsymbol{r}} \cdot \boldsymbol{u} \\ &= \frac{2\mu}{r}\frac{\partial^2\psi}{\partial r\partial\varphi} - \frac{2\mu}{r^2}\frac{\partial\psi}{\partial\varphi} = 2\mu\frac{\partial}{\partial r}\left(\frac{1}{r}\frac{\partial\psi}{\partial\varphi}\right),\end{aligned} \tag{3.75}$$

$$\begin{aligned}\tau_{r\varphi} = \mu\hat{\boldsymbol{r}} \cdot [\nabla \boldsymbol{u}] \cdot \hat{\boldsymbol{\varphi}} + \mu\hat{\boldsymbol{\varphi}} \cdot [\nabla \boldsymbol{u}] \cdot \hat{\boldsymbol{r}} &= \mu\hat{\boldsymbol{r}} \cdot \nabla (\boldsymbol{u} \cdot \hat{\boldsymbol{\varphi}}) - \mu (\hat{r} \cdot \nabla\hat{\boldsymbol{\varphi}}) \cdot \boldsymbol{u} + \mu\hat{\boldsymbol{\varphi}} \cdot \nabla (\boldsymbol{u} \cdot \hat{\boldsymbol{r}}) - \mu (\hat{\varphi} \cdot \nabla\hat{\boldsymbol{r}}) \cdot \boldsymbol{u} \\ &= \mu\frac{\partial}{\partial r}\left(\frac{\partial\psi}{\partial r}\right) - 0 + \frac{\mu}{r}\frac{\partial u_r}{\partial\varphi} - \frac{\mu}{r}\hat{\boldsymbol{\varphi}} \cdot \boldsymbol{u} \\ &= \mu\left(\frac{\partial^2\psi}{\partial r^2} - \frac{1}{r}\frac{\partial}{\partial\varphi}\left(\frac{1}{r}\frac{\partial\psi}{\partial\varphi}\right) - \frac{1}{r}\frac{\partial\psi}{\partial r}\right).\end{aligned} \tag{3.76}$$

Note that as expected $\tau_{rr} + \tau_{\varphi\varphi} = 0$. In the same way, we derive the following expression for the vorticity, or curl of the velocity

$$\operatorname{curl} \boldsymbol{u} = \hat{\boldsymbol{r}} \cdot [\nabla \boldsymbol{u}] \cdot \hat{\boldsymbol{\varphi}} - \hat{\boldsymbol{\varphi}} \cdot [\nabla \boldsymbol{u}] \cdot \hat{\boldsymbol{r}} = \frac{\partial^2\psi}{\partial r^2} + \frac{1}{r}\frac{\partial}{\partial\varphi}\left(\frac{1}{r}\frac{\partial\psi}{\partial\varphi}\right) + \frac{1}{r}\frac{\partial\psi}{\partial r} = \nabla^2\psi. \tag{3.77}$$

The viscosity term in the Stokes equations can be written as

$$\nabla \cdot \tau = \nabla \cdot (\hat{\boldsymbol{r}}\tau_{rr}\hat{\boldsymbol{r}} + \hat{\boldsymbol{r}}\tau_{r\varphi}\hat{\boldsymbol{\varphi}} + \hat{\boldsymbol{\varphi}}\tau_{\varphi r}\hat{\boldsymbol{r}} + \hat{\boldsymbol{\varphi}}\tau_{\varphi\varphi}\hat{\boldsymbol{\varphi}}) \tag{3.78}$$

$$= (\nabla \cdot \hat{\boldsymbol{r}})\,(\tau_{rr}\hat{\boldsymbol{r}} + \tau_{r\varphi}\hat{\boldsymbol{\varphi}}) + \hat{\boldsymbol{r}} \cdot \nabla\,(\tau_{rr}\hat{\boldsymbol{r}} + \tau_{r\varphi}\hat{\boldsymbol{\varphi}}) + (\nabla \cdot \hat{\boldsymbol{\varphi}})\,(\tau_{\varphi r}\hat{\boldsymbol{r}} + \tau_{\varphi\varphi}\hat{\boldsymbol{\varphi}}) + \hat{\boldsymbol{\varphi}} \cdot \nabla\,(\tau_{\varphi r}\hat{\boldsymbol{r}} + \tau_{\varphi\varphi}\hat{\boldsymbol{\varphi}})\,. \tag{3.79}$$

In addition to (3.73), we use the following identities

$$\nabla \cdot \hat{\boldsymbol{r}} = \frac{1}{r}, \quad \nabla \cdot \hat{\boldsymbol{\varphi}} = 0, \tag{3.80}$$

and the fact that $\tau_{\varphi\varphi} = -\tau_{rr}$. After reordering to group the radial and transverse components this leads to

$$\nabla \cdot \tau = \left[\frac{2}{r}\tau_{rr} + \frac{\partial \tau_{rr}}{\partial r} + \frac{1}{r}\frac{\partial}{\partial \varphi}\tau_{\varphi r}\right]\hat{\boldsymbol{r}} + \left[\frac{2}{r}\tau_{r\varphi} + \frac{\partial \tau_{r\varphi}}{\partial r} - \frac{1}{r}\frac{\partial \tau_{rr}}{\partial \varphi}\right]\hat{\boldsymbol{\varphi}} \tag{3.81}$$

$$= \left[-\frac{2\mu}{r}\frac{\partial}{\partial \varphi}\frac{\partial^2 \psi}{\partial r^2} + \frac{1}{r}\frac{\partial}{\partial \varphi}\tau_{\varphi r}\right]\hat{\boldsymbol{r}} + \left[\mu\frac{\partial^3 \psi}{\partial r^3} + \frac{\mu}{r}\frac{\partial^2 \psi}{\partial r^2} - \frac{\mu}{r^2}\frac{\partial \psi}{\partial r} + \frac{\mu}{r^2}\frac{\partial^3 \psi}{\partial \varphi^2 \partial r} - \frac{2\mu}{r^3}\frac{\partial^2 \psi}{\partial \varphi^2}\right]\hat{\boldsymbol{\varphi}} \tag{3.82}$$

$$= -\frac{\mu}{r}\left[\frac{\partial}{\partial \varphi}\nabla^2 \psi\right]\hat{\boldsymbol{r}} + \mu\left[\frac{\partial}{\partial r}\nabla^2 \psi\right]\hat{\boldsymbol{\varphi}}. \tag{3.83}$$

In combination with the pressure gradient term in polar coordinates

$$\nabla p' = \frac{\partial p'}{\partial r}\hat{\boldsymbol{r}} + \frac{1}{r}\frac{\partial p'}{\partial \varphi}\hat{\boldsymbol{\varphi}}, \tag{3.84}$$

we obtain the radial and transverse components of the Stokes momentum equation in (3.7) and (3.8).

Chapter 4

Mesh Adaptivity for Mantle Convection in Spherical Shell Domains

This chapter discusses the use of mesh adaptivity for geodynamical models in spherical shell domains. The efficacy of mesh adaptivity, in particular anisotropic mesh adaptivity, was already demonstrated in Davies et al. (2011) for Cartesian domains. Here we discuss some of the issues to make this technique available in curved spherical or cylindrical domains, and a relatively simple approach to overcome these. As before, we demonstrate the functionality and efficiency of the method using a number of relevant benchmarks. This chapter is a paper in preparation that has not yet been published. The methods have already been applied, enabling the modelling of subduction zones in spherical shell geometries in Chen et al. (2022a) and Chen et al. (2022b).

4.1 Introduction

Numerical models play an invaluable role in improving our understanding of the structure and dynamics of Earth's mantle. Global mantle convection modelling involves the resolution of a broad range of length scales with some relatively short length scale features, e.g. in subduction zones near the surface or mantle plumes that rise from the core-mantle boundary, interacting

with and driving the global solution. Efficient computational solution therefore requires the ability to focus mesh resolution, and as some of these features evolve dynamically, the ability to dynamically adapt the mesh (May et al., 2013). For this reason a number of mantle convection codes have been developed (Burstedde et al., 2008; Leng et al., 2011; Kronbichler et al., 2012; Burstedde et al., 2013) that implement adaptive mesh refinement (AMR) techniques which allow variable mesh resolution through a series of quadtree (or octree in 3D) refinement steps with respect to a uniform base mesh. A more flexible approach is found in fully unstructured *adaptive remeshing* or *mesh optimisation* techniques, in which a completely new mesh is generated that is optimised to conform to a quality metric based on an a-posteriori error estimate. It allows for mesh alignment with lower dimensional features, such as material interfaces and upwelling plumes, and is able to produce anisotropic meshes that are only refined in the direction of strong curvature, e.g. across an interface or orthogonal to a plume, and coarse in other directions, thus being able to significantly further reduce the required number of degrees of freedom over AMR methods.(Davies et al., 2011)

There are, however, a number of clear advantages of AMR methods: the underlying hierarchy facilitates efficient interpolation in a straightforward manner, and the construction of highly effective geometric multigrid methods. In uniform, Cartesian aligned flow, quadrilateral or hexahedral based finite element discretisations can be more efficient than fully unstructured, triangular or tetrahedral mesh-based methods. The implementation of fully unstructured adaptive remeshing on large scale problems, in particular when run in parallel, brings with it a number of challenges, that are more easily handled in AMR methods, such as dynamic load (re)balancing and mesh adaptation across local domains. It also requires more complex solution strategies such as algebraic multigrid (AMG) methods. However, many of these challenges can be overcome through the use of modern libraries, e.g load balancing in Zoltan (Boman et al., 2012), and AMG preconditioning techniques in PETSc (Balay et al., 2022). As shown in Davies et al. (2011) the increased flexibility to put resolution where needed, and only in those directions required by the anisotropy of the flow solution, leads to a significant reduction in the number of degrees of freedom, motivating efforts to overcome these challenges.

Some additional challenges arise when moving from problems in Cartesian domains, such at

those in Davies et al. (2011), to mantle convection modelling in an Earth-like, spherical domain. Without access to a grid-independent description of the geometry, as in e.g CAD-based geometries, the remeshing library will try to preserve the geometry as it was approximated by the previous mesh. This means that upon refinement at the surface, the approximation of the sphere will not actually improve but maintain the same piecewise approximation. Conversely, when coarsening the mesh, the options are to either strictly maintain the geometry, which effectively disallows coarsening at the surface, or to allow some modification of the geometry by taking away surface nodes. The latter will inevitably lead to a gradual deterioration of the spherical approximation, as once coarsened the more accurate description of the domain is lost and thus can not be restored again through subsequent refinement. Related to this problem is the fact that generic unstructured interpolation algorithms require the mesh before and after the mesh adaptation to conform to exactly the same geometry: if the geometry is allowed to evolve, nodes in the new mesh may end up outside the previous mesh and it becomes unclear how values should then be extrapolated.

AMR methods in spherical domains (Burstedde et al., 2013) deal with this issue using the fact that there is a natural coordinate transformation from cells before and after the adapt through the unchanging underlying cubed-sphere structure. In this chapter, we demonstrate how, for fully unstructured meshes in combination with adaptive mesh optimisation techniques, a similar remapping can be applied such that the mesh adaptation and interpolation steps take place in a common, unchanging geometry, before mapping back to a geometry that most accurately describes the geometry of the sphere. As discussed in section 4.3.5 however, with highly anisotropic meshes care must be taken that such remappings do not lead to the inversion of elements and we therefore have to ensure that the unchanging geometry in which the mesh is adapted does not deviate too much from the most accurate description of the sphere.

4.2 Metric-based Anisotropic Mesh Adaptivity

In this section we first give a brief overview of anisotropic mesh adaptivity, which in contrast with hierarchical Adaptive Mesh Refinement (AMR) approaches, allows for variable resolution with different mesh lengths in different directions not necessarily aligned with the main Cartesian directions, or with radial or azimuthal directions in spherical domains. More details can be found in Davies et al. (2011) and Pain et al. (2001b).

4.2.1 The Metric

The anisotropic mesh adaptivity process is controlled by the choice of a metric tensor: a tensor field $\mathcal{M}_{ij}(\boldsymbol{x})$ which provides a symmetric positive definite matrix for all locations $\boldsymbol{x}$ in the domain Ω incorporating the locally required mesh resolution in different directions. The metric $\mathcal{M}_{ij}$ defines a norm that provides a measure of the length of any candidate edge, represented by a vector $\boldsymbol{v}_i = \boldsymbol{x}_i^a - \boldsymbol{x}_i^b$ between its vertices $\boldsymbol{x}_i^a$ and $\boldsymbol{x}_i^b$, through:

$$\|\boldsymbol{v}\|_{\mathcal{M}} = \sum_{i,j} \boldsymbol{v}_i \mathcal{M}_{ij} \boldsymbol{v}_j \tag{4.1}$$

The edge is said to be of ideal length if $\|\boldsymbol{v}\|_{\mathcal{M}} = 1$.

There are many different methods of selecting an appropriate metric. Here, we use a Hessian based metric derived from an estimate of the quadratic interpolation error for piecewise linear polynomials on the mesh. Consider the standard Taylor series approximation:

$$f(\boldsymbol{x} + \boldsymbol{v}) = f(\boldsymbol{x}) + \frac{\partial f(x)}{\partial \boldsymbol{x}} \boldsymbol{v} + \tfrac{1}{2} \boldsymbol{v}^T \frac{\partial^2 f(\boldsymbol{x})}{\partial \boldsymbol{x}^2} \boldsymbol{v} + \mathcal{O}(\|\boldsymbol{v}\|^3) \tag{4.2}$$

As the first two terms on the right-hand side can be represented exactly by linear polynomials, the quadratic error is given by the third term. Thus if we want to bound this error by a user selected error bound ϵ

$$|\boldsymbol{v}^T \frac{\partial^2 f(\boldsymbol{x})}{\partial \boldsymbol{x}^2} \boldsymbol{v}| \leq \epsilon, \tag{4.3}$$

we choose the metric

$$\mathcal{M}(\boldsymbol{x}) = \frac{1}{\epsilon}\left|\frac{\partial^2 f(\boldsymbol{x})}{\partial \boldsymbol{x}^2}\right| \tag{4.4}$$

Since the Hessian matrix $\frac{\partial^2 f(\boldsymbol{x})}{\partial \boldsymbol{x}^2}$ is not necessarily positive, we construct a positive semi-definite version (indicated by $|.|$) by replacing its eigenvalues in its eigendecomposition by their absolute values. A positive definite version is achieved by imposing a maximum edge length to avoid arbitrary large edge lengths in directions of zero curvature. This makes the metric a majorant of the Hessian (Chen et al., 2007). Similarly, by bounding the eigenvalues from above, minimum edge lengths can be imposed. Finally, the metrics associated with multiple solution fields can be combined such that the chosen interpolation bound is satisfied for all fields. Through so called gradation of the metric, we also impose a constraint on how fast the resolution can change from one element to another.

Through Céa's lemma it is possible to relate the upper bound for interpolation error to the discretisation error between the discrete and exact solution of the PDE (see e.g. Frey et al., 2005). The Hessian-based metric is however by no means the only way to efficiently distribute mesh resolution whilst controlling the discretisation error, and there are other choices of metric that may achieve this more accurately, for instance based on higher order reconstructions of the residual in the equations (e.g. Yano et al., 2012; Ceze et al., 2013). It has been found, however, that the Hessian based metric provides a simple and inexpensive method that gives a good indication of where to place resolution for an accurate representation of the solution field. This is confirmed in the analytical test cases in section 4.4.

Scaled Metric

The error bound in (4.3) requires the estimated interpolation error to be smaller than a user chosen ϵ everywhere in the domain, and in that sense can be interpreted as a bound on the infinity norm of the estimated error. In solutions with large variations and discontinuities, the Hessian can become arbitrarily large locally which leads to very small edge lengths and thus to a large number of simplices (triangles or tetrahedrons) in that area. If, more generally, we

consider the L_p error norm

$$\|u - u_I\|_p = \sqrt[p]{\int_\Omega |u - u_I|^p},$$

the equidistribution of error, i.e. using the same bound on the local interpolation error $|u-u_I| \leq \epsilon$ everywhere, may not be the most optimal way to reduce this L_p-error: allowing for larger errors in limited areas where the curvature is large and tightening the error bound elsewhere could lead to a more efficient distribution of simplices through the domain. If we allow ϵ to vary through the domain, we need to balance its contribution to the integrated interpolation error

$$\|u - u_I\|_p^p \approx \int_\Omega \epsilon^p dx \tag{4.5}$$

and to the required number of simplices. This number can be estimated for a given varying ϵ using the fact that locally we can relate the metric to a coordinate transformation where in the transformed coordinates ξ the standard Euclidean metric measures the same distances as the metric $\mathcal{M}$ in physical space $x \in \Omega$. A simplex whose edges all have ideal length $\|x^a - x^b\|_\mathcal{M} = 1$ is therefore a regular tetrahedron in ξ coordinates, with volume $\frac{1}{12}\sqrt{2}$. The same volume can however be computed in physical space using the Riemannian volume form

$$\tfrac{1}{12}\sqrt{2} = \int_T d\xi = \int_T \sqrt{\det \mathcal{M}} dx. \tag{4.6}$$

Assuming all simplices in our mesh closely approximate this ideal shape to some degree (for details see Chen et al., 2007) we can then estimate the number of required simplices N through

$$\int_\Omega \sqrt{\det \mathcal{M}} dx = \sum_T \int_T \sqrt{\det \mathcal{M}} dx \approx \sum_T \tfrac{1}{12}\sqrt{2} = N \tfrac{1}{12}\sqrt{2} \tag{4.7}$$

which depends on the local error bound ϵ through (cf. (4.4))

$$\sqrt{\det \mathcal{M}} = \epsilon^{-n/2} \sqrt{\det \left| \frac{\partial^2 u}{\partial x^2} \right|}, \tag{4.8}$$

where n is the dimension of the domain.

Considering the multi-objective minimisation of both (4.5) and (4.7), an optimal choice for ϵ

can then be found in

$$\epsilon = \lambda \left(\det \left| \frac{\partial^2 u}{\partial x^2} \right| \right)^{\frac{1}{2p+n}} \tag{4.9}$$

where λ is a user chosen constant. This choice is optimal in the sense that it minimises the error in the chosen L_p-norm for a given number of simplices, or vice versa minimises the number of simplices required to achieve a certain value for the L_p error.

4.2.2 Mesh Adaptivity Process

The goal of the mesh adaptivity process is to produce an unstructured mesh in which the edges adhere to the ideal lengths expressed in the metric as closely as possible. This is done through iterative local improvements of an existing mesh, the same mesh also used to discretise the metric tensor field. However this existing mesh merely functions as a starting point in the mesh optimisation process, and the final optimised mesh no longer bears any relation to the original mesh.

To guide the mesh optimisation process we define a mesh functional that expresses the mesh quality on an element-by-element basis. For mesh adaptivity in three dimensions, we use the Pain functional (Pain et al., 2001b).

$$F_{e|\mathcal{M}} = \frac{1}{2} \sum_{l \in \mathcal{L}_e} \frac{1}{2} \left(\|l\|_{\mathcal{M}} - 1 \right)^2 + \left(\frac{\frac{1}{12}\sqrt{6}}{r_{e|\mathcal{M}}} - 1 \right)^2 \tag{4.10}$$

where $\mathcal{L}_e$ is the set of edges l of the tetrahedral element e, and $r_{e|\mathcal{M}}$ is the inner radius of the element (radius of the inner circle/sphere within a triangle/tetrahedron) measured with respect to the metric $\mathcal{M}$. The second term, which promotes the inner radius to be close to that of a regular tetrahedron, is to deal with the fact that even with small deviations of the edges from an ideal length of one, the resulting tetrahedron may still be excessively flat. In the two-dimensional adaptivity we use the Lipnikov functional(Vasilevskii et al., 1999).

The mesh optimisation process iterates through elements and edges of the mesh and considers one of the following local operations if it reduces either the maximum or the average of the

functional evaluated in those elements affected by the operation. The operations considered are (cf. figure 4.1):

1. In an *edge split* a new node is placed in the middle of an existing edge, doubling the number of elements adjacent to the original edge.

2. In an *edge collapse* an edge is collapsed by moving one of its vertices on top of the other, thus deleting all elements adjacent to it.

3. In an *edge-edge swap* an existing edge is replaced by another without adding or deleting any nodes. In two dimensions the edge shared between two adjacent triangles can be replaced by connecting the opposite): vertices. In three dimensions, an edge shared by four elements can be replaced by one of two other possible edge internal to the combined four elements.

4. A *edge-face swap* is a three dimensional operation in which the face between two adjacent tetrahedrons is removed and replaced by an edge between the two vertices opposite the face, which will the divide the combined original two elements, into three new elements. Or, vice versa, three elements sharing an edge are combined into two elements by replacing the edge with a face.

5. In a *node movement* operation, a single node is moved to a new location within the combined adjacent elements. This new location is chosen in a local optimisation process that minimises the functional of the combined elements.

4.2.3 Curved Surfaces and Geometry Preservation

In order for the overall geometry of the domain covered by the mesh not to change, a number of restrictions have to be put in place on the operations in the previous section. The surface of the mesh, which forms the boundary of the numerical domain, can be divided in a number of planes each of which consists of the triangles in the surface mesh that are adjacent and coplanar.

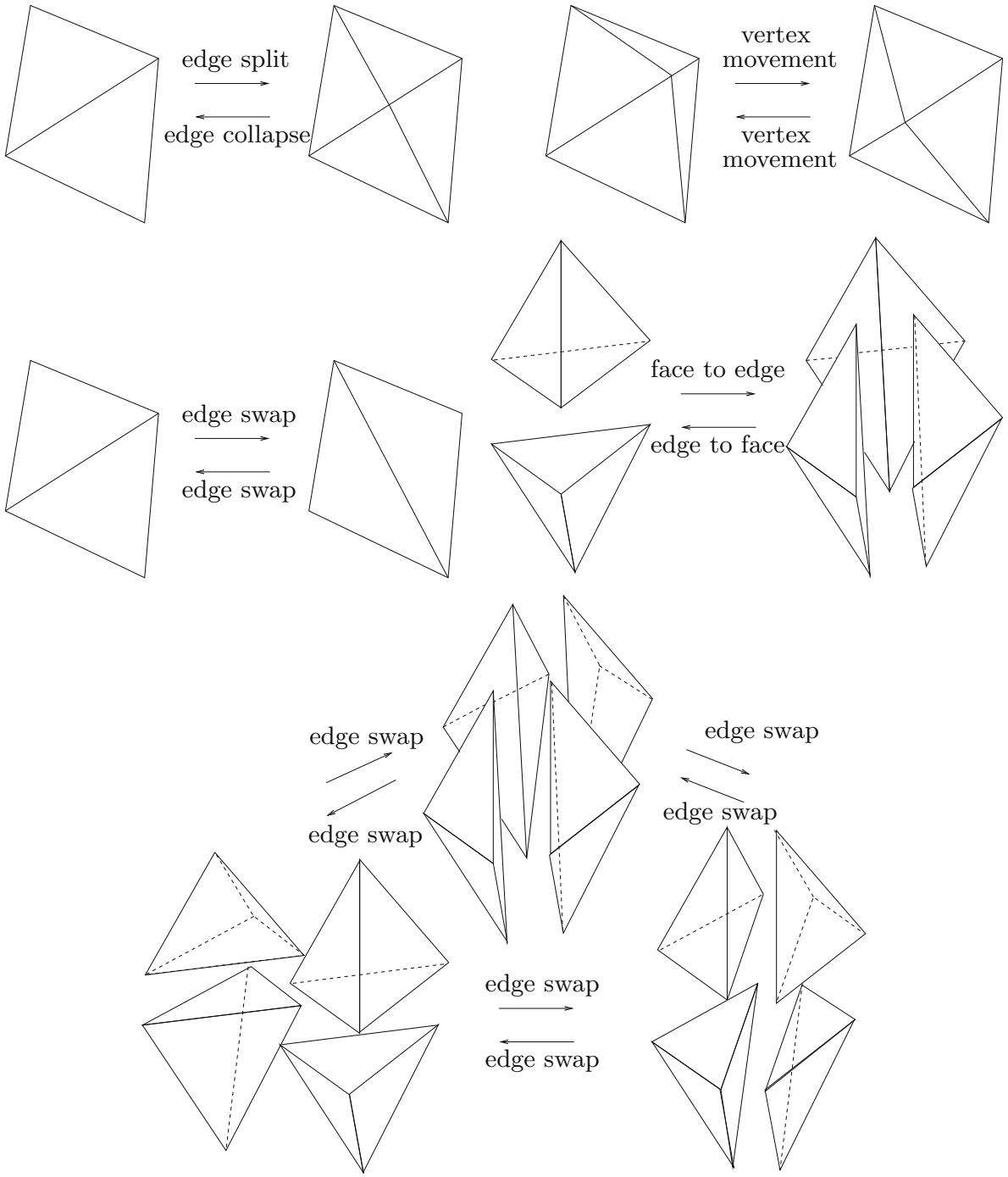


Figure 4.1: Mesh optimisation operations. This figure previously appeared in Davies et al. (2011)

Within those planes mesh adaptivity should be free to adapt the mesh at will, but the straight edges separating the planes, so called geometry edges, each consisting of a (variable) number of triangle edges, should be maintained. This also means that the geometry vertices, in which the geometry edges coincide, should not be moved.

In particular this means that in an edge collapse operation, if one of the two mesh vertices is interior and the other on the surface, the collapse should move the interior vertex on top of the surface vertex. If both vertices in an edge collapse are on the surface, but one is located on a geometry edge, the move should be towards that vertex, and if one of the two vertices coincides with a geometry vertex the move should be towards that location. Moreover, if a geometry edge consists of just a single mesh edge, that edge can not be collapsed. Similarly, when a node at the surface is moved, it may only move along the same plane it was originally on, or if it is on a geometry edge only along that edge. A geometry vertex can not be moved.

These restrictions ensure that the computational domain as covered by the mesh remains exactly the same before and after the mesh adaptation. As we will see in the following section this is not necessarily desirable if the computational domain is an approximation of a physical domain with curved boundaries.

4.3 Mesh Adaptivity in Spherical Shell Domains

4.3.1 Adapting the Geometry

In an accurate approximation of the spherical shell domain with a linear simplicial mesh the surface vertices of top and bottom boundaries are located exactly on the inner and outer sphere bounding the domain. The mesh geometry is thus bounded by a piecewise planar approximation of these spheres, formed by triangles none of which are coplanar with any of its neighbours.

If we impose the rules of section 4.2.3 which enforce a strict conservation of that geometry, refinement of the mesh will lead to a further subdivision of the surface triangles, but newly added surface vertices will be located on the plane formed by the original triangles rather

than on the exact sphere. Thus, despite the increased resolution, we do not obtain a more accurate representation of the spherical domain. Conversely, if we want to coarsen the mesh, the geometry constraints do not permit the removal of any edges from the surface mesh (as they are all geometry edges). Although the algorithm is free to coarsen in the interior, we can not coarsen beyond the original resolution of the surface mesh, creating bad elements near the surface.

Relaxing those rules creates its own problems. If we allow the surface mesh to be coarsened locally beyond the original mesh, we obtain a less accurate description of the geometry. However in a dynamic simulation the coarsening at one stage might be followed by the subsequent need for refinement in that same area, say because of a flow feature passing through. When we refine the mesh we then have to somehow re-introduce this more accurate description of the sphere that has been lost. One way to achieve this, is to use the fact that we have an analytical description of the physical domain boundaries in the form of spheres, and so we can place any new surface vertices directly on the sphere, rather than on the triangular planes of the previous mesh. More general approaches exist in which more complex domains are described through a series of analytical curves and surfaces that are maintained throughout the simulation and, at each mesh adaptivity stage, a surface mesh of the required mesh resolution is dynamically regenerated (see e.g. Beaufort et al., 2020).

Allowing the computational geometry to change, further complicates both the mesh adaptivity process itself but also has consequences for a model that dynamically adapts the mesh and solves the equations on a sequence of meshes in time, where it will need to interpolate the solution fields between subsequent meshes. Already during the mesh adaptivity process, the metric field needs to continuously be interpolated from the previous mesh on which it was formed, to the current iterative mesh approximation. New nodes on the surface may find themselves outside the previous computational geometry and thus can not be interpolated by using straightforward linear interpolation. This situation can be improved by locally transforming either the previous mesh to more accurately follow the domain boundary, or by warping back the new geometry to conform to the old. Such local coordinate transformations however easily lead to inversion of elements.

4.3.2 Base Geometry

To avoid the issues described in the previous section, we propose a relatively simple strategy to deal with curved boundaries that requires no significant modifications to the mesh adaptivity library. The strategy involves the specification of a base geometry, which is a relatively coarse approximation of the spherical shell domain bounded by a surface mesh that remains the same throughout subsequent adapts in a simulation. This surface mesh provides the minimal resolution for a sufficiently accurate representation of the sphere. The mesh adaptivity process is allowed to further refine, but as new nodes are added on the surface, subdividing the triangles of the base geometry surface mesh, the new nodes are not moved outward, thus maintaining the original base geometry as formed by the original, larger surface mesh triangles. Only once the entire process has completed the final adapted mesh is warped, moving all vertices in the surface mesh outward to lie exactly on the inner or outer sphere and thus better fit the actual spherical shell domain. It is this warped mesh that is then used to discretise and solve the equations for a specified number of timesteps. After which, in the next adaptation stage, the domain is warped back to coincide with the original base geometry but maintaining the increased resolution of the first adaptivity stage. The next adaptivity stage is then allowed to coarsen in places where less resolution is now required and add resolution elsewhere, as long as it does not change this warped-back geometry (i.e. it can not coarsen beyond the resolution of the base geometry). At the end of this stage the final mesh is again warped outwards to better match the spherical shell domain, in particular where resolution has increased. This mesh is then again used in a subsequent number of timesteps, after which the whole process repeats.

This strategy also avoids the problem of having to interpolate between geometries that are not exactly the same: the interpolation of solution fields is done immediately afterwards, between the before- and after mesh that both conform to the same base geometry.

In our 3D simulations we use an icosahedral mesh, an icosahedron in which the original 20 triangles are iteratively each divided into four for a number of times, according to the specified refinement level. This defines the unchanged base geometry that is used in the mesh adaptivity stages throughout the simulation. The resolution of this base geometry mesh defines a minimal

resolution at the surface. It should be noted however that although the edges of this mesh need to be maintained as geometry edges in all mesh adaptivity stages, this is only a (minor) restriction at the surface of the mesh and the mesh adaptivity library is still free to place resolution where it wants in the interior of the domain. In 2D, the base geometry is bound by a uniform interval mesh of prescribed coarse resolution that approximates the inner and outer circular boundaries of the domain.

4.3.3 Coordinate Transformation

To avoid inversion of elements, the coordinate transformation at the end of each mesh adaptivity stage, which warps the base geometry to a more accurate representation of the exact spherical shell geometry, moves not only the surface vertices but also the interior vertices outward. It can be described as follows: For any point $\boldsymbol{x}$ in the interior of the domain we can find a point $\boldsymbol{x}_B$ right below and $\boldsymbol{x}_T$ above it on respectively the inner and outer boundary of the base geometry by ray tracing in the radial direction. The warped coordinate $\hat{\boldsymbol{x}}$ after transformation is then given by:

$$\hat{\boldsymbol{x}} = \frac{(1-\alpha)R_- + \alpha R_+}{\|\boldsymbol{x}\|}\boldsymbol{x}, \quad \text{where } \alpha = \frac{\|\boldsymbol{x}-\boldsymbol{x}_B\|}{\|\boldsymbol{x}_T-\boldsymbol{x}_B\|} \text{ such that } \boldsymbol{x} = (1-\alpha)\boldsymbol{x}_B + \alpha\boldsymbol{x}_T. \quad (4.11)$$

Here R_+ and R_- are the radii of the inner and outer spheres respectively. Note that points which are already on one of the base geometry boundaries, i.e. $\boldsymbol{x} = \boldsymbol{x}_B$ or $\boldsymbol{x} = \boldsymbol{x}_T$ with $\|\boldsymbol{x}_B\| \leq R_-$ and $\|\boldsymbol{x}_T\| \leq R_+$, are moved radially outward to be exactly on the spheres with radius R_-, respectively R_+, so that this transformation indeed maps the geometry to the exact spherical shell geometry.

The transformation is illustrated in figure 4.2. Note that in a linear mesh the transformation is only applied to the vertices, and thus the surface is still approximated piecewise by linear edges, or triangles in 3D, but the approximation is more accurate in regions with high resolution. When using higher order, curved mesh cells (e.g. using quadratic tetrahedrons or triangles in an isoparametric P2-P1 discretisation) the shape of which is determined by the location of a

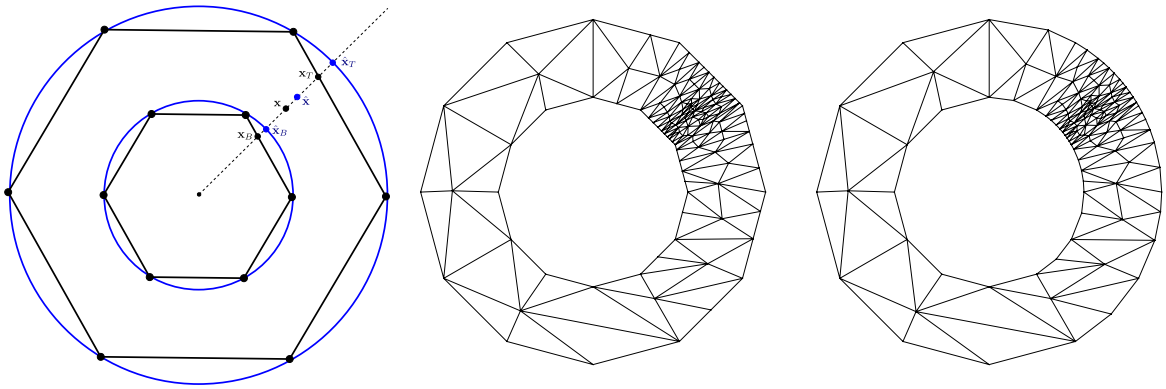


Figure 4.2: Left: Transformation of the point $\boldsymbol{x}$ in the interior of the base geometry bounded by two hexagons to $\hat{\boldsymbol{x}}$ through interpolation of its radius between the points $\boldsymbol{x}_B$ and $\boldsymbol{x}_T$. The points $\boldsymbol{x}_B$ and $\boldsymbol{x}_T$ themselves are moved to $\hat{\boldsymbol{x}}_B$ and $\hat{\boldsymbol{x}}_T$ respectively on the inner and outer circular boundary of the analytical cylindrical shell domain. Middle and Right: Cylindrical shell approximated with 12-sided polygon as the base geometry (middle figure) with adapted mesh that in places of higher resolution better approximates the cylinder after transformation (right figure).

number of extra Lagrangian nodes in addition to the vertices, we apply the same transformation to these nodes, thus bending the cells to more accurately follow the curved surface.

4.3.4 Gnomonic Projection

To find the top and bottom locations $\boldsymbol{x}_T$ and $\boldsymbol{x}_B$, we need to find the surface triangle that intersects the "radial" ray through x and the origin. To simplify this process, we define a horizontal coordinate system that is invariant under radial rescaling, in other words, all points on a radial ray are mapped to the same horizontal coordinate. For this we use the gnomonic projection (e.g. Palache, 1920) obtained by projecting all locations on a hemi-sphere onto a tangent plane by computing the intersection with this plane of the ray through the point and the origin. As an example, for a unit sphere the gnomonic projection on the tangent plane at its North Pole is given by

$$\boldsymbol{x}_{H,i} = \boldsymbol{x}_i / \boldsymbol{x}_3 \text{ for } i = 1, 2 \tag{4.12}$$

This maps all points on the Northern hemisphere onto the plane, with the North Pole mapped to the origin, and the equator mapped to infinity.

The reason for choosing this gnomonic projection is that it projects great circles on a sphere,

as well as straight 3D line segments to a straight line (segment) in the plane. In particular this means that a triangular mesh on a sphere, consisting of straight 3D edges between vertices of equal radius, will be mapped to a triangular mesh with straight edges in the plane. Using projections that do not have this property, a point on the surface that is inside one of the triangles of the surface mesh, may not be inside that same triangle after projection due to the curvature of the edges.

Although in principle the entire sphere can be mapped using two opposite projection planes at the North and South pole, this would give complications for triangles that straddle the equator which is mapped to infinity in both projections. Instead we use six tangent planes, two in each Cartesian direction, where we project each point on a sphere to its nearest plane, thus mapping the entire sphere to the sides of a unit-cube. Note that this projection is the same as used in a cubed-sphere approximation of the Earth, in the form of a quadrilateral mesh approximating the sphere which is divided in six regions that can be mapped to the sides of a cube. The horizontal coordinates correspond to the X, Y coordinates in the notation of Ronchi et al., 1996. In the cubed-sphere mesh the boundaries between these regions are exactly coincident with edges in the mesh. In our approach triangles in a non-uniform triangular spherical mesh can straddle multiple regions, in which case these triangles are simply duplicated on the different projection planes.

Finally, to find the location of $\boldsymbol{x}_T$ at the the top surface, straight above a point $\boldsymbol{x}$ in the interior of the shell, we can simply compute its horizontal coordinate through the gnomonic projection, and find that location in one of the six parts of the top surface mesh projected onto the six planes. This is then a straightforward query of finding a 2D location in a 2D mesh that can be implemented efficiently using a R-tree spatial index approach (Guttman, 1984). Note that we only use the gnomonic projection to locate the surface triangle that $\boldsymbol{x}_T$ is located in, we do not use the horizontal coordinates for interpolation. The exact 3D location of $\boldsymbol{x}_T$ is then found by intersecting the ray through $\boldsymbol{x}$ with the plane through the triangle in 3D.

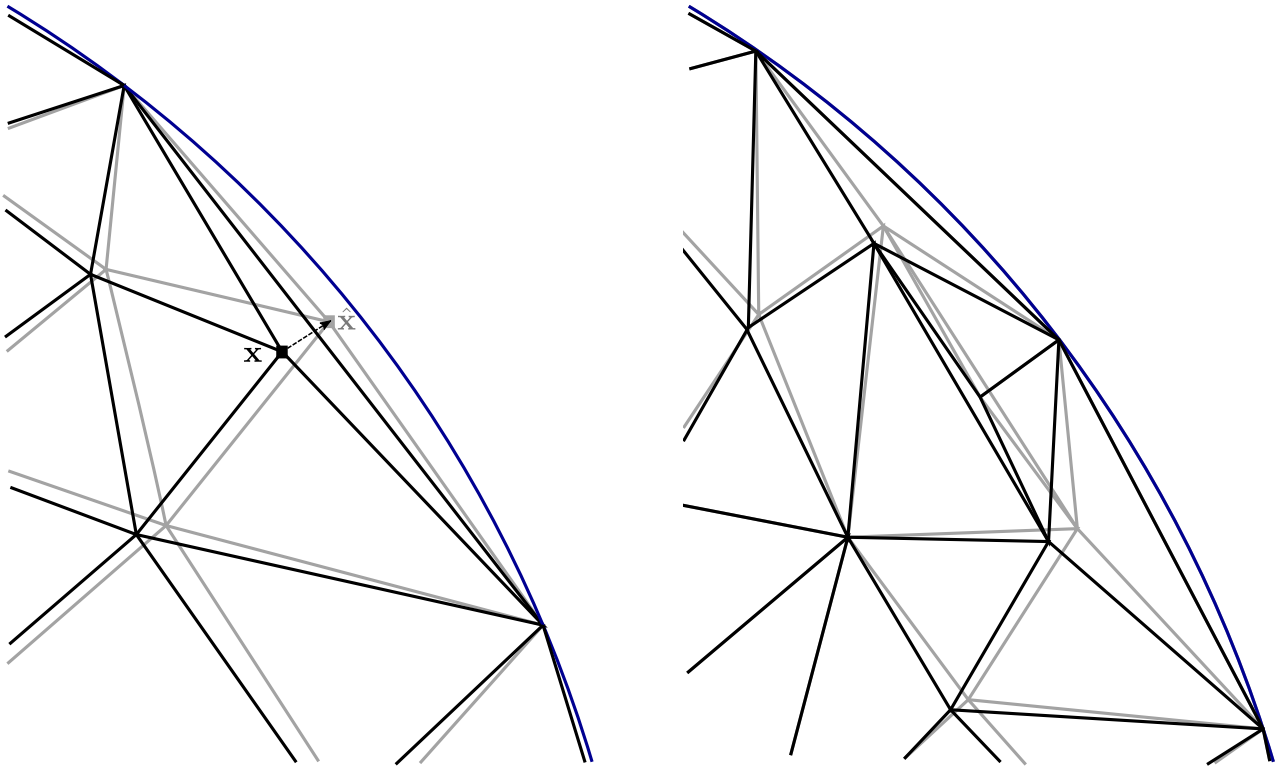


Figure 4.3: Inversion of large aspect ratio triangles. Left: the vertex $\boldsymbol{x}$ of the mesh in black that conforms to the base geometry, is transformed to $\hat{\boldsymbol{x}}$ in the warped mesh in grey, and ends up on the other side of the long boundary edge of the flat triangle thus inverting it. Right: the top vertex of the flat triangle is below a surface node, and therefore does not move under the transformation, whereas the two vertices at the base of the flat triangle are moved further out such that the triangle is inverted.

4.3.5 Avoiding Element Inversion

Although we avoid most cases of element inversion by moving interior vertices by the same amount as those exactly above and below it on the surface, the amount of radial scaling does vary in the lateral direction: vertices located below a geometry vertex do not move at all, whereas vertices below the interior of a base geometry plane are pushed outwards. This difference can still cause inversion of very flat (large aspect ratio) cells. Figure 4.3 shows two cases of this in 2D. Such cases can be avoided, however, by enforcing a maximum aspect ratio bound. This is a standard procedure in metric-based mesh adaptivity, where the aspect ratio can be limited by limiting the smallest eigenvalue of the metric, associated with the largest allowable edge length in any direction, with respect to the largest eigenvalue (smallest edge length).

It can be shown that the inversion cases in 2D shown in figure 4.3 can be avoided altogether by imposing a maximum aspect ratio, here defined as maximum ratio of edge length over height, of

$$\tan(\alpha)\frac{1}{1-\cos(\alpha)}, \tag{4.13}$$

where $\alpha = 2\pi/n$ is the angle of the base geometry approximating the inner and outer circle, which is divided in n equal intervals. For $n = 32$ this means we need to impose a maximum aspect ratio of 10, the same as the typical aspect ratio applied for numerical reasons (e.g. Davies et al., 2011), so that for $n \geq 32$ this does not really impose a further constraint.

In 3D however, we found the mesh adaptivity library sometimes unable to satisfy the imposed aspect bound, encoded in the metric, for flat tetrahedrons located just below a base geometry edge. The library considers all operations described in section 4.2.2 one by one, and only if an operation on its own improves the functional, it is selected. Because of the constraints of the geometry however, for these flat triangles it found that none of the individual operations immediately led to an improvement, thus leaving these tetrahedrons untouched and violating the aspect ratio bound. We found that we needed to modify the algorithm to allow it to combine the operations of splitting an edge with a vertex, with an immediate moving of that new vertex to a locally optimal location (see figure 4.4). Only when the algorithm is then

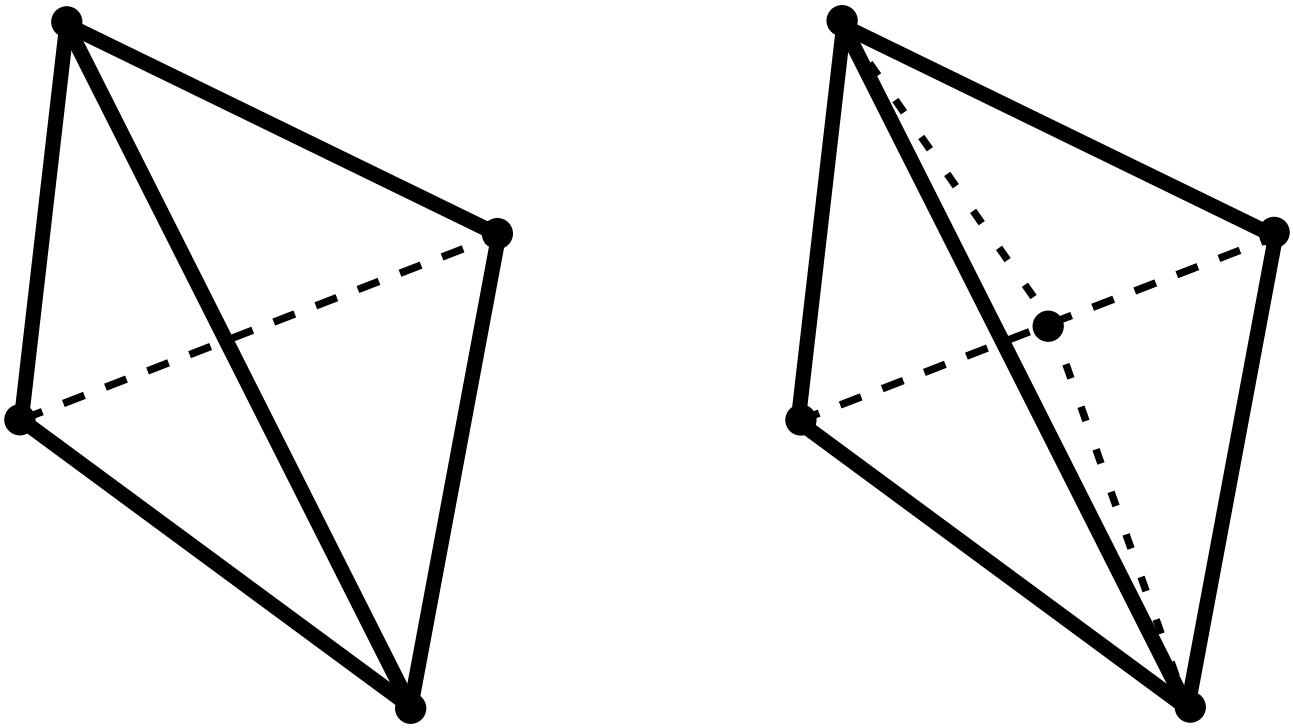


Figure 4.4: Flat tetrahedron just below the surface of the base geometry with two of its triangles being part of the surface mesh, joined at a large interior angle along an edge that forms part of a base geometry edge. The edge opposite, indicated by a dashed line, is the only interior edge of the triangle. Two interior triangles meet at this interior edge, also at large angle. All vertices are on the surface. This situation is resolved by splitting the interior edge with a vertex in its middle, which subdivides the tetrahedron (and all other tetrahedrons adjacent to this edge) in two, and thus splits the large interior angle below the geometry edge. To deal with the large angle at the original interior edge, this operation needs to be combined with a moving of the node downwards into the interior of the domain.

allowed to consider the combined effect of these two operations on the functional, it was able to successfully eliminate these cases.

4.3.6 Metric Transformation

Since the partial differential equations are solved in the warped domain, the metric should be based on the interpolation error, and thus the Hessian of the solution fields, in the transformed $\hat{\boldsymbol{x}}$-coordinates. Following the procedure in section 4.2.1, it would then provide a metric for the optimal edge length in $\hat{\boldsymbol{x}}$-coordinates. During the mesh adaptivity stage however we need to measure the edge lengths in the base geometry $\boldsymbol{x}$ coordinates. We therefore transform the metric $\hat{\mathcal{M}}$, which is assembled in $\hat{\boldsymbol{x}}$-coordinates, according to

$$\mathcal{M} = \frac{\partial \Phi}{\partial \boldsymbol{x}}^T \hat{\mathcal{M}} \frac{\partial \Phi}{\partial \boldsymbol{x}} \tag{4.14}$$

where $\hat{\boldsymbol{x}} = \Phi(\boldsymbol{x})$ is the coordinate transformation, before passing it onto the mesh adaptivity library.

4.4 Test Cases

4.4.1 Steady State

To demonstrate the capability of anisotropic mesh adaptivity to drastically reduce the number of degrees of freedom required to achieve a certain level of accuracy, we study a case with a prescribed temperature/density distribution for which an analytical solution is known. The analytical solution, with a free slip condition at both boundaries, has been worked out in chapter 3, specifically section 3.2.3. It employs a prescribed density perturbation of

$$\rho'(r, \theta, \varphi) = \frac{r^k}{R_+^k} Y_{lm}(\theta, \varphi) \tag{4.15}$$

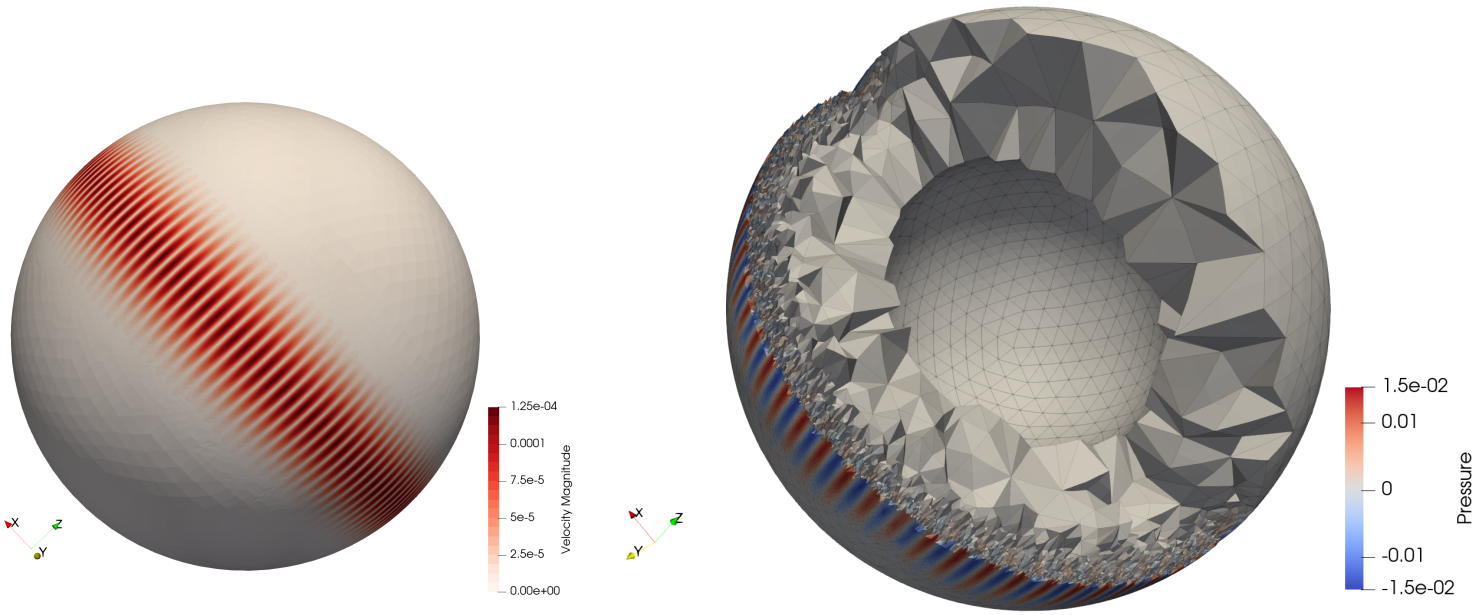


Figure 4.5: Numerical result on adaptive mesh for the free-slip spherical benchmark case (see section 3.2.3) with $k = l = m = 64$. The solution contains a band of anisotropic features around the equator in velocity (left) and pressure (right) which are concentrated near the surface. The right figure shows the interior adaptive mesh through a cut-out of the $y > 0, z > 0$ quadrant. Thin long elements are visible providing high resolution resolving the anisotropic features, with much larger elements in the rest of the domain.

where Y_{lm} is Laplace's spherical harmonic function of degree l and order m, and R_+ is the radius of the Earth.

We choose relatively high values for the radial degree k and harmonic degree and order, $k = l = m = 64$, which leads to a series of highly anisotropic features near the surface in the solution as can be seen from figure 4.5. The adapted mesh resolves these features through thin and long tetrahedrons. In the rest of the domain, the mesh resolves the much coarser base geometry, as described in the previous sections, to maintain the approximate outline of the spherical shell domain, whilst still allowing large elements in the interior.

Figure 4.6 shows the discretisation error, calculated as the L2-norm difference between the numerical and analytical solutions (left for velocity and right for pressure), against number of elements used for fixed mesh runs at various resolutions, and mesh-adaptive runs with various values for the target interpolation error. The horizontal mesh for the non-adaptive, fixed mesh cases was created from an icosahedral approximation of the sphere refined 3, 4, 5, or 6 times, where each level of refinement subdivides all triangles into four, resulting in resp. 20×4^3,

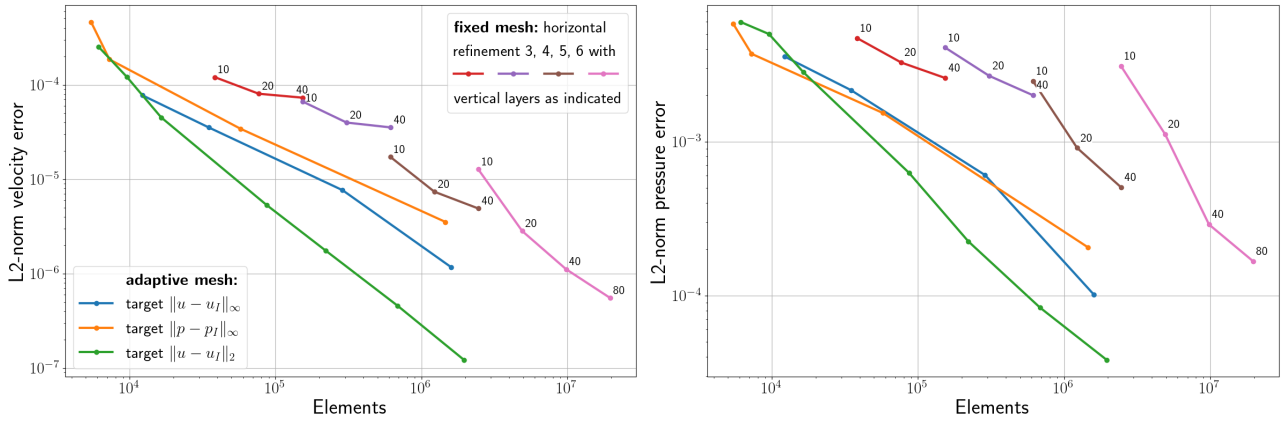


Figure 4.6: Elements vs. numerical error in velocity (left) and pressure (right) measured as the L2-norm difference between numerical and analytical solution. Fixed mesh results using a icosahedral mesh with 3, 4, 5, and 6 levels of refinement in the horizontal, and 10, 20, 40, and 80 layers in the vertical. Adaptive mesh results using different target interpolation error to determine the distribution of edge lengths via the metric. Blue and orange results use an unscaled Hessian metric in velocity and pressure respectively, resulting in a maximum interpolation error everywhere. Green uses a scaled Hessian metric that optimally distributes resolution to minimise the L2 interpolation error.

$20{\times}4^4$, $20{\times}4^5$, and $20{\times}4^6$ triangles. This mesh is then extruded in the vertical, creating prisms that are each divided in three tetrahedrons, using a varying number of vertical layers for each horizontal refinement level to determine the optimal aspect ratio.

We compare the fixed mesh errors with mesh-adaptive results obtained using three different ways of specifying the target interpolation error. The blue and orange lines indicate the resulting discretisation error with a mesh resolution such that the interpolation error estimate in either velocity (blue) or pressure (orange) remains below a chosen target value (cf. equation (4.3)). Not unexpectedly, specifying a maximum *interpolation* error in velocity rather than pressure leads to a lower *discretisation* error in velocity for the same number of elements. Conversely however, using the maximum interpolation error in pressure as the basis of the metric only gives a marginally better result in pressure discretisation error in most cases. This indicates velocity is the more important component of the solution when using its interpolation error to guide the distribution of resolution.

The green line in figure 4.6 indicates the results when the metric is based on a rescaled Hessian, as described in section 4.2.1, in order to minimise the estimated L2 interpolation error in velocity. This leads to a more efficient distribution of resolution, resulting in a significantly

lower discretisation error (also in the L2 norm) for the same number of elements, in all cases.

When comparing the fixed mesh results with the adaptive mesh results, it becomes clear that the adaptive results are much more accurate when using the same number of elements. Or, to look at it the other way around, to achieve the same level of accuracy the adaptive mesh runs require significantly less degrees of freedom. For instance to achieve an L2 norm error of 1×10^{-6} a fixed mesh of $\approx 10^7$ elements is required. The adaptive result with a target infinity norm interpolation error only uses $\approx 2 \times 10^6$ elements. Using a target L2 norm interpolation error only $\approx 3 \times 10^5$ elements are needed.

4.4.2 Rising Plume in Spherical Domain

In the modelling of mantle convection, thermal plumes are a prime example of features that can be efficiently resolved using mesh adaptivity, in particular anisotropic mesh adaptivity as was demonstrated in a Cartesian domain in Davies et al. (2011). Here we present a test case based on Burstedde et al. (2013) in a $45^o \times 45^o$ section of a spherical shell domain. Vertically the domain extends $R_- = 1.22 \leq r \leq R_+ = 2.22$. In this domain we solve for velocity $\boldsymbol{u}$ and pressure p using the incompressible Stokes equations

$$-\nabla \cdot \left(\mu \left(\nabla \boldsymbol{u} + (\nabla \boldsymbol{u})^T\right)\right) + \nabla p = \mathbf{Ra}\ T\ \hat{\boldsymbol{r}}, \tag{4.16}$$

$$\nabla \cdot \boldsymbol{u} = 0 \tag{4.17}$$

with radial unit vector $\hat{\boldsymbol{r}}$ and Rayleigh number $\mathbf{Ra}$, coupled to a advection diffusion equation for temperature T

$$\frac{\partial T}{\partial t} + \boldsymbol{u} \cdot \nabla T + \nabla^2 T = 0 \tag{4.18}$$

The rheology of the problem is given by a temperature dependent viscosity

$$\mu(T) = \exp(-ET) \tag{4.19}$$

where $E = \ln(100)$. The initial condition for temperature consists of a background, which for $r \leq R_- + w_{\text{tbl}}$ is given by

$$T_0 = 1.0 - erf\left(\frac{r - R_-}{\frac{1}{2}w_{\text{tbl}}}\right), \tag{4.20}$$

where $w_{\text{tbl}} = 0.15$ is the width of the thermal boundary layer. For $r > R_- + w_{\text{tbl}}$ we use a background temperature of $T_0 = 0$. To this background we add an anomaly

$$T_{\text{ic}}(\boldsymbol{x}) = T_0 + \exp\left(\frac{-\|\boldsymbol{x} - \boldsymbol{x_0}\|}{2\sigma^2}\right) \tag{4.21}$$

which is centred at $\boldsymbol{x_0}$ located $D/10$ ($D = R_+ - R_-$) below the bottom boundary, and $\sigma = D/15$. Boundary conditions for temperature are $T = 0.5$ at the surface, $T = T_{\text{ic}}$ at the bottom boundary, and zero flux at the sides. These are combined with free slip conditions for the Stokes velocity, pressure system on all boundaries.

In the previous test cases, the number, size, and spatial distribution of the elements in the adapted mesh were chosen to meet an a-priori specified bound on an estimate of the interpolation error. For a dynamically evolving simulation however, it can be hard to predict how many elements this will result in. In particular with an infinity-norm based error metric, the required resolution near a jump in the solution can, in principle, become infinite. Although the rescaled metric based on integrated error estimates, such as the L2 norm, more efficiently distributes the resolution in the presence of such jumps, the overall number of required elements can still be hard to control.

In practice, the error based metric is often combined with a minimum element size. This avoids excessively small elements and allows some control over the number of elements. In places that would require smaller edge lengths than the specified minimum to meet the error estimate, this edge length is capped at the minimum, but elsewhere the mesh is adapted as usual according to the error metric. Thus the user chooses a minimal resolution, often combining considerations based on the physical processes to be resolved and computational cost, but allows the model to coarsen where appropriate. From this perspective it makes sense to compare the cost of a uniform mesh model when applying the same minimal resolution everywhere, and that of an

adaptive mesh model. If the error metric is chosen such that the accuracy of the model does not significantly degrade, the coarsening effectively eliminates degrees of freedom that contribute little to the accuracy of the model.

The uniform meshes L4, L5, L6, L7, L8 are constructed by taking a $45^o \times 45^o$ slice from a cubed sphere mesh with the same number of elements in all three directions, resulting in respectively $16^3, 32^3, 64^3, 128^3$, and 256^3 cubes, with each cube divided in six tetrahedral elements. In the corresponding adaptive runs, the minimum edge length is chosen as the uniform edge length at the bottom boundary: $\frac{45}{180}\pi/2^n$ for the Ln mesh. The adaptive runs are allowed to coarsen in accordance with the target error metric with larger edge lengths, but, as described previously, need to maintain a minimal representation of the geometry in the form of a base geometry. The base geometry is chosen as the 8×8 surface mesh at the top and the bottom (with each of the 64 squares divided into two triangles) for the L4 and L5 cases, and the 16×16 surface mesh for L6, L7, and L8. In the interior a maximum edge length of 0.1 is maintained. In figure 4.7 a cut-through slice of the L5 adaptive plume model is shown at three time levels: $t = 0.0015, t = 0.003$, and $t = 0.0045$.

In figure 4.8 the uniform mesh runs are compared with their adaptive mesh counterparts, in terms of the number of mesh nodes (vertices), and the following three diagnostics: Nusselt number at the bottom and top of the domain (cf. Zhong et al., 2008a), and the root-mean squared velocity

$$\mathrm{Nu}_B = \frac{R_-}{R_+(R_+ - R_-)} \frac{\int_{r=R_-} -\frac{\partial T}{\partial r}\, \mathrm{d}S}{\int_{r=R_-} \mathrm{d}S} \tag{4.22}$$

$$\mathrm{Nu}_T = \frac{R_+}{R_-(R_+ - R_-)} \frac{\int_{r=R_+} -\frac{\partial T}{\partial r}\, \mathrm{d}S}{\int_{r=R_+} \mathrm{d}S} \tag{4.23}$$

$$\langle \mathrm{V}_{\mathrm{RMS}} \rangle = \sqrt{\frac{\int_\Omega \|\boldsymbol{u}\|^2 \mathrm{d}V}{\int_\Omega \mathrm{d}V}} \tag{4.24}$$

For each uniform/adaptive pair at each increased level of resolution, the adaptive result is closer than the uniform result to the result of either the uniform or adaptive results at the next level of resolution. This suggests that the mesh adaptive results using the same minimal resolution are in fact more accurate than their uniform counterpart. This can partially be explained from

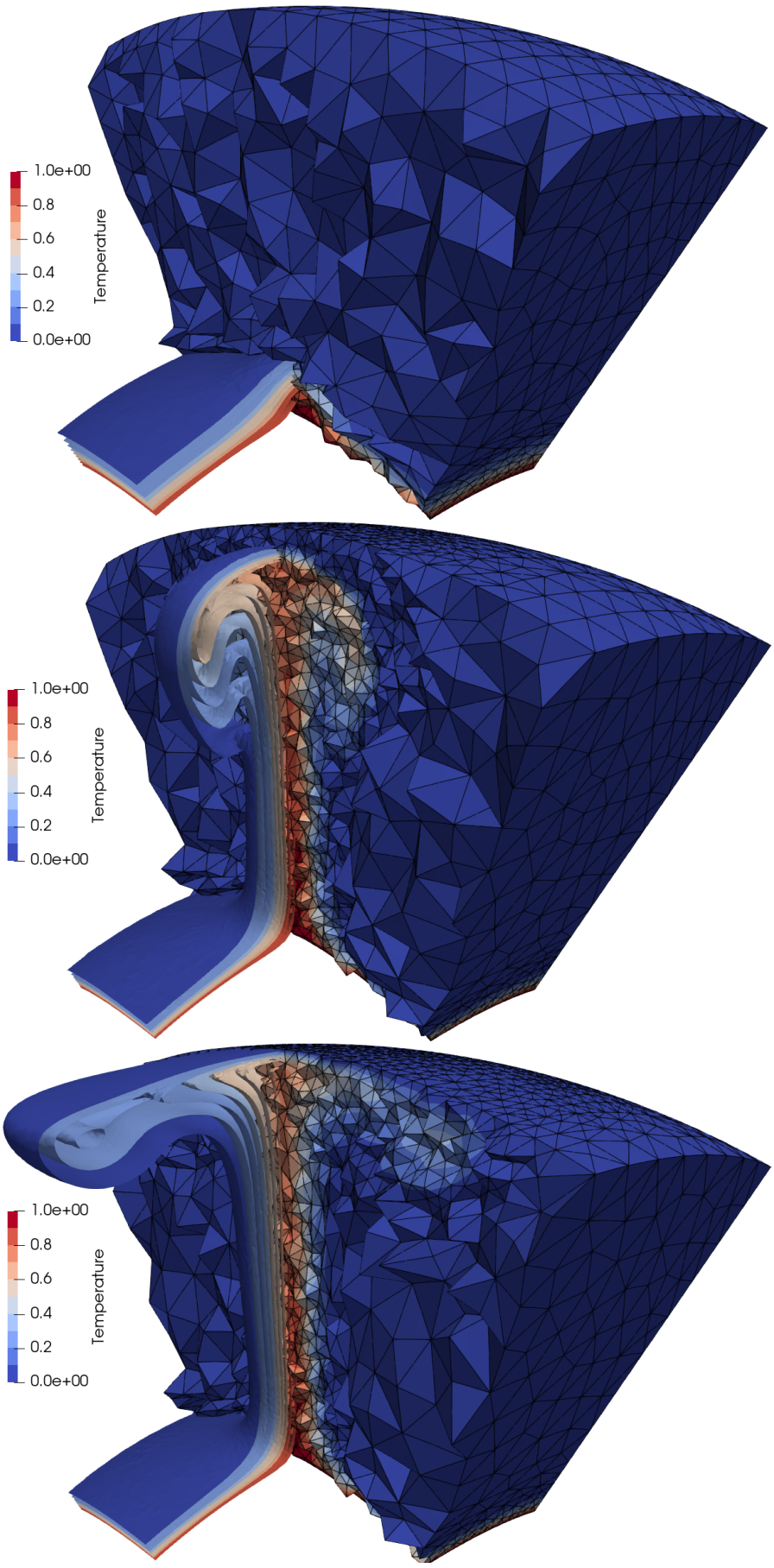


Figure 4.7: Cut-through slices of the adaptive mesh plume model with minimum edge length corresponding to L5 (see main text at page 143 for a description of cases), at time levels $t = 0.0015, t = 0.003$, and $t = 0.0045$. Shown is the outline of the cut-through adapted mesh in half the domain ($x > 0$), and temperature contours in a quarter of the domain ($x < 0$ and $y > 0$) at $T = 0.1, 0.2, \ldots 0.9$.

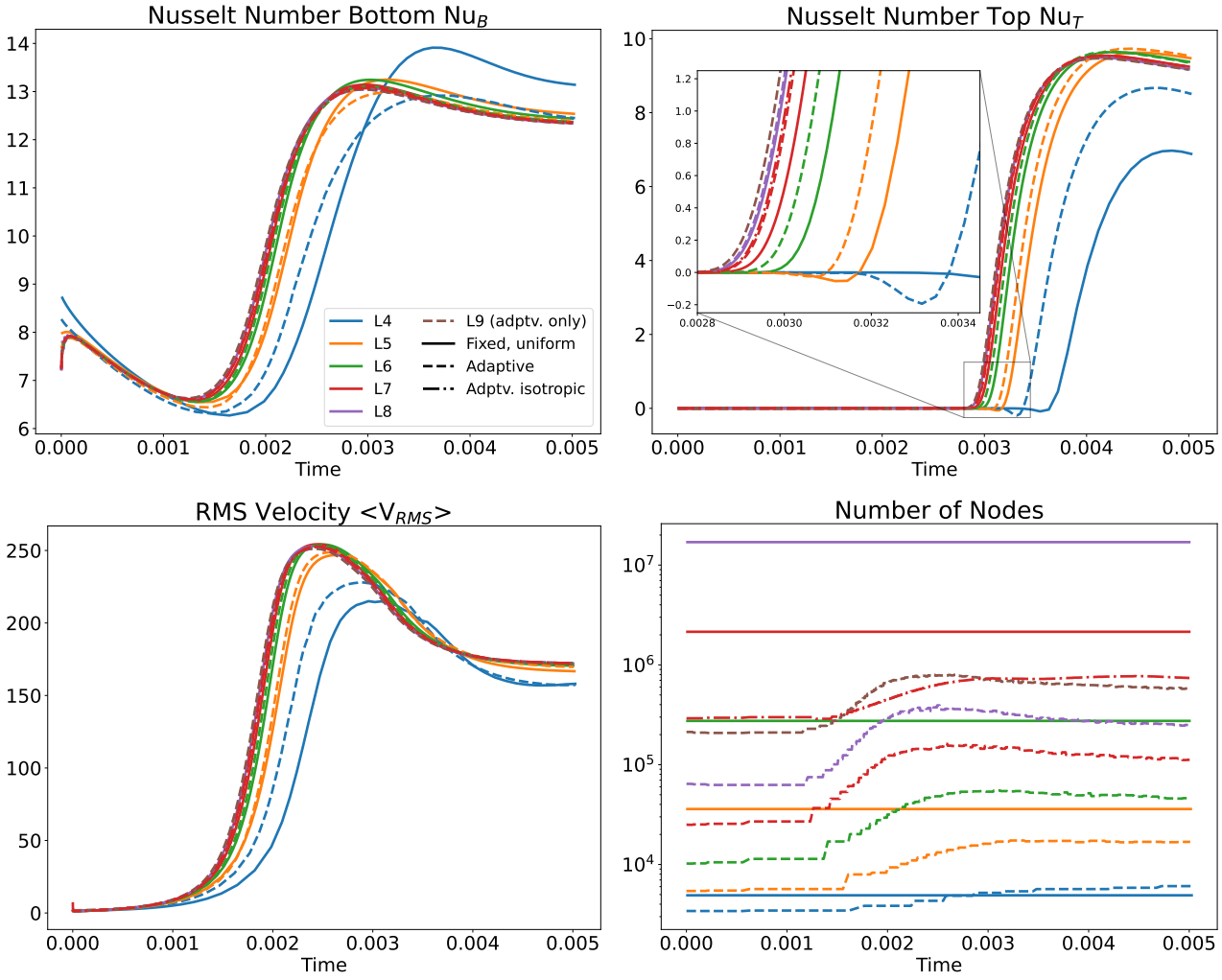

Nusselt Number Bottom Nu_B
Nusselt Number Top Nu_T
RMS Velocity <V_{RMS}>
Number of Nodes
Time
L4
L5
L6
L7
L8
L9 (adptv. only)
Fixed, uniform
Adaptive
Adptv. isotropic

Figure 4.8:

	Uniform					Adaptive				
level	vertices	timesteps	cores	walltime (hr)	total time (hr)	vertices	timesteps	cores	walltime (hr)	total time (hr)
L4	4913	71	14	0.09	1.3	4539	137	8	0.28	2.3
L5	35937	149	28	0.9	25.7	13066	298	8	2.18	17.5
L6	274625	296	224	2.3	511	42246	550	56	5.67	317.
L7	2146689	587	840	10.7	8991	120314	886	112	11.4	1276
L8	16974593	1158	840	179	150023	279064	1143	168	25.8	4328
L9						620581	1361	336	38.0	12759

Table 4.1: Computational costs for the uniform and adaptive mesh cases: number of vertices (average for adaptive cases), number of timesteps, number of CPU cores employed, the walltime for each run, and the total compute hours calculated as the product of the previous two.

the fact that the minimum edge length, which is based on the edge length at the bottom of the domain, allows for edge lengths at the top of the domain that are smaller in the adaptive case than in the uniform case. A further explanation (also observed in Davies et al., 2011) is that although the adaptive mesh model can not use a higher resolution to resolve the front of the plume, the model has more freedom to optimally align the mesh with the front than in the uniform mesh.

Apart from the L4 case, in which the adaptive minimum edge and maximum edge length are close (0.06 vs. 0.1), in all subsequent pairs the adaptive mesh requires significantly fewer nodes than the uniform mesh. Given the fact that the mesh adaptive results are at least as accurate, the significant reduction in the number of nodes, displayed in the bottom right of figure 4.8, again highlight the significant savings that can be made using mesh adaptivity. To investigate the contribution of anisotropy, we have also included an adaptive version of L7 in which the metric is modified such that in each location the minimum is taken of the desired local edge lengths in different directions, generating an isotropic mesh, in which the edge length is varied throughout the domain but always the same in all directions. The isotropic version of the L7 adaptive case (indicated by red, dash-dot line graphs in figure 4.8) uses substantially more vertices than the anisotropic case (red, dashed), but does not appear to be any more accurate, thus demonstrating the additional saving that can be made by allowing for anisotropy in the mesh.

These savings are also reflected in table 4.1 in which the number of CPU cores and walltime for the different runs are given. Note that the increase in total compute time for the uniform meshes

converges to a factor of slightly more than 16, which corresponds to a factor of $2 \times 2 \times 2$ in the degrees of freedom and a doubling of the number of the number of timesteps to maintain the CFL condition. A factor of exactly 16 therefore would correspond to ideal strong scaling, which can be challenging to achieve due to the fact that the increased condition number typically leads to an increase in the number of iterations required in the iterative solvers unless well tuned multigrid methods are employed. Here, we employ algebraic multigrid multigrid preconditioning for both the uniform and adaptive cases (see Davies et al., 2022, for more details)) which indeed appears to provide good strong scaling.

For the adaptive cases, the number of vertices (averaged over all timesteps) increases much slower when halving the minimum edge length. The number timesteps required to satisfy the CFL condition also increases slower. This can be explained through the fact that the minimum edge lengths are not necessarily employed in the same direction as the highest velocity: the anisotropic resolution enables the resolution of the gradients, in the lateral direction of the plume, whereas the highest velocities are measured in the direction along the plume. At L4 the adaptive mesh run is more expensive, but more accurate (in the sense of being closer to higher resolution runs), due to a higher timestep count. For higher resolution runs the adaptive cases rapidly become much cheaper than the uniform cases, leading to a speed up by a factor of 34 in the L8 case. The L9 case, whilst still being run in reasonable time with an adaptive set up, becomes unfeasible in the uniform case.

4.5 Conclusions

It has been recognised in the mantle convection modelling community that mesh adaptation techniques can bring significant computational savings over models with uniform mesh resolution (Burstedde et al., 2008; Davies et al., 2008; Kronbichler et al., 2012; Leng et al., 2011). As demonstrated in Davies et al. (2011) and in the test cases in this paper, anisotropic mesh optimisation can bring additional savings over hierarchical Adaptive Mesh Refinement (AMR) techniques. During each stage of anisotropic mesh optimisation, a completely new mesh is gen-

erated with complete freedom to optimally focus resolution and apply different mesh lengths in different directions without any constraints from an underlying mesh hierarchy. This allows for the generation of an optimally efficient mesh, but adds some complexity in the implementation: interpolation between unrelated meshes, dynamic reload balancing, and the need for more generic algebraic multigrid methods.

Although the presence of curved domain boundaries introduces some additional challenges, in this paper we describe a simple approach, for the case of spherical shell domains, to overcome issues associated with resolution-dependent geometry changes. We demonstrate that similar savings in terms of degrees of freedom and computational cost as in Davies et al. (2011) can be obtained in spherical shell domains of global mantle convection models. In particular this opens up the possibility of modelling localised phenomena, like the mantle flow in a subduction zone and its interaction with the geometric constraints of the entire global mantle. In Cartesian models we choose a limited-size domain around the region of interest, but the presence and relative closeness of boundary conditions may affect the results, as was demonstrated in Chen et al. (2022a), as well as the reduction of space with depth and variation of the radial gravitational direction in spherical models which is absent in Cartesian models. In fact it is the adaptive mesh functionality for spherical shell domains described here, that has made tractable the modelling in Chen et al. (2022a) which investigates this influence of sphericity in subduction zone models, as well as the models in Chen et al. (2022b) which investigates the influence of slab width and age on the dynamics of subduction. We further expect these techniques to be vital in global scale models in which the interaction, on a global scale, between multiple localised phenomena is investigated, and in more detailed, realistic global mantle models in which features at various length scales may interact.

Chapter 5

Summary of Conclusions and Achievements

This final chapter summarises the main achievements from this thesis work and conclusions that can be drawn.

5.1 Free Surface Methods

- Implicit time integration can be effectively used to stabilise the movement of the free surface in geodynamical models with large timesteps.

- Rather than actually moving the free surface mesh nodes as in Lagrangian models, the modelling can be simplified by assuming a fixed Eulerian reference frame and applying the free surface-induced hydrostatic pressure variation as a normal stress boundary condition.

- This method, as presented in Kramer et al. (2012) can be further simplified by eliminating the free surface degrees of freedom, and shown to be equivalent, under simplified conditions (see section 2.6.2) to the stabilisation of Kaus et al. (2010) for Lagrangian models, now applied in the Eulerian frame.

- Through this equivalence, the stabilisation method of Kaus et al. (2010) can also be interpreted as a θ-scheme implicit time integration.

- For cases where the simplified conditions are not met, e.g. in spherical domains or with lateral variations in density at the surface, care must be taken to maintain symmetry in the stabilisation term, keeping it in the form of equation (2.65), in which case the relation between the original implicit method with additional free surface degrees of freedom, and the reduced system with a stabilisation term, can be maintained.

- The method is formally unconditionally stable for $\theta \geq \frac{1}{2}$.

- At $\theta = \frac{1}{2}$ its temporal convergence is second order.

- The method has been tested using a set of analytical solutions based on Zhong et al. (1996), which have been derived in section 2.3. These have already proven useful in further publications (Furuichi et al., 2015; Rose et al., 2017; Wilson et al., 2017) to verify, analyse and compare free surface methods.

- A number of free surface methods have now been published which can be categorised as follows:

    1. The "Sticky Air" approach (Crameri et al., 2012)
    2. Lagrangian models with nonlinear convergence of the mesh movement (Furuichi et al., 2015)
    3. Lagrangian models with a stabilisation term as in Kaus et al. (2010)
    4. Eulerian models with implicit time integration (this thesis and Kramer et al., 2012)
    5. Exponential or "Nonstandard Finite Difference" time integration of the free surface (Rose et al., 2017)

- Further testing is required to compare the different methods in particular in more challenging cases with a large variety of spatial and temporal scales.

5.2 Analytical Solutions in Cylindrical and Spherical Shell Domains

- The derivation of analytical solutions in cylindrical and spherical shell domains with suitable boundary conditions is not straightforward. Although techniques to derive these, such as the Mie representation splitting the solution in poloidal and toroidal parts, are well known, working out the solution coefficients is cumbersome and error prone.

- To facilitate verification, analysis and comparison of geodynamical models in these domains a suite of analytical solutions has been derived, rigorously tested for correctness, and implemented in a python package. The eight cases are all combinations of the following choices:

  1. Cylindrical vs. spherical shell domain,
  2. A generic monomial smooth forcing vs. a delta-function,
  3. Free slip vs. no slip boundary conditions.

- Numerical discretisations with a continuous representation for the pressure solution, such as the popular Taylor-Hood element pair, struggle with convergence in the presence of discontinuities in pressure.

- This issue has not been previously noted in 3D benchmark studies (Zhong et al., 2008a), used in, amongst others, (Davies et al., 2013; Burstedde et al., 2013; Liu et al., 2019), as the calculated diagnostics were all based on integrated surface response which does converge at the right rate.

5.3 Mesh Adaptivity in Spherical Shell Domains

- Mesh adaptivity, and in particular, metric-based anisotropic mesh optimisation can bring substantial savings in computational cost for geodynamical models, as shown already in Davies et al. (2011) for Cartesian domains.

- Applying these techniques in cylindrical and spherical shell domains introduces a number of challenges related to the fact that as the mesh is refined or coarsened near the boundary, the computational geometry approximating the domain changes. This has an effect on both the mesh optimisation process itself, and the interpolation of solution fields between subsequent meshes.

- These challenges can be overcome with a relatively simple to implement approach, in which the mesh adaptivity process and the interpolation always takes places in the same unchanged base geometry, a coarse description of the shell domain. Only when the mesh is used to solve the equations for the solution fields, does it get transformed (popped out) to more accurately follow the exact spherical geometry in regions of high resolution.

- Care must be taken to prevent inversion of elements in such coordinate transformations. These can be prevented if a reasonable aspect ratio bound is maintained.

- In 3D, the mesh adaptivity library can fail to maintain this aspect ratio bound in all cases if it is not given the freedom to combine edge splitting and node movement operations.

- Additional savings can be made if the resolution is spread more efficiently to satisfy L_p bounds by rescaling the metric appropriately, rather than enforcing the same maximum interpolation error estimate everywhere.

- The analytical cases of chapter three also proved useful in evaluating the mesh adaptivity techniques in chapter four.

- A test case of a mantle plume in a spherical shell segment confirms the method scales up to very large, high-resolution models on a large number of cores. It is shown that significant savings in computational time of more than one order in magnitude can be made, with the adaptive cases making tractable resolutions that are no longer feasible with uniform meshes. Furthermore, we confirm that the fact that the mesh can be adapted anisotropically, unlike in Adaptive Mesh Refinement (AMR) methods, leads to significant additional efficiency savings.

5.4 Future directions

In this thesis I have analysed a number of numerical techniques for geodynamical models, more specifically, free surface time-integration methods (chapter two) and mesh adaptivity techniques for cylindrical and spherical shell domains (chapter four). Following on from the achievements and conclusions summarised in the previous sections, a variety of open questions and avenues for further research remain.

Two recent publications (Furuichi et al., 2015; Rose et al., 2017) have suggested potential alternatives to the implicit time integration method advocated in Kramer et al. (2012) and chapter two. Moreover, at the end of this chapter we discussed connections between the implicit method and the stabilisation method of (Kaus et al., 2010). Although the analytical benchmark cases of Kramer et al. (2012) were already used in Furuichi et al. (2015) and Rose et al. (2017) to make some preliminary comparisons between the methods, I believe a broader comparison of the various free surface methods is warranted. In particular, in less idealised cases, including curvature of the free surface, lateral density variations at the surface, and a wider range of temporal and spatial scales, more significant differences between the methods may become apparent. For consistency of such comparisons, it would be preferable to implement all the different approaches in a single model code base, e.g. Fluidity, such that all other discretisation details can be kept the same.

Analysing the efficacy of anisotropic mesh adaptivity in cylindrical and spherical domains, we have shown that significant savings can be made over uniform mesh cases. As we have discussed in chapter four, anisotropic mesh adaptivity does put some limitations on the available options for discretisation and solver algorithms when compared with hierarchical AMR methods, and in particular when compared with structured mesh models. Solving the Stokes system, we are restricted to algebraic instead of geometric multigrid solution methods, and we need to use tetrahedral mesh discretisations rather than hexahedral. It is therefore a valid concern that, since we have used the same discretisation and solution methods in the adaptive and uniform cases, these are not necessarily the most efficient for the uniform cases. To run the uniform cases, which are based on hexahedral structured meshes, with the same discretisation we have

to divide all hexahedrons into six tetrahedrons. Using discretisations and multigrid solver techniques that would potentially be more favourable on these uniform meshes, would require a complete reimplementation of the associated finite element code in Fluidity, or running it in a completely different model, which in turn may bring other inconsistencies in the comparison with the adaptive runs.

The challenges in such comparisons motivate the use of some more modern code development approaches that offer more flexibility in changing discretisation and solver techniques. For the large code bases underlying contemporary geodynamical models, such as, e.g., Fluidity (Davies et al., 2011) and ASPECT (Liu et al., 2019), the desired properties of efficiency, flexibility and code maintainability are often at conflict with each other. Choices made in the early development stages of such models tend to limit the flexibility to change these assumptions later on without extensive rewrites. The modern finite element frameworks FEniCS (**Logg˙2012**) and Firedrake (Rathgeber et al., 2016), overcome some of these issues, by allowing the user (in this case the developer of a new geodynamical model) to specify the finite element discretisation in the usual weak form in a dedicated ("Domain Specific") symbolic language (UFL, see Alnes et al., 2014). The framework automatically derives (compiles) highly optimised low level code for the assembly of these equations "just in time" for the specific case that is being run. The high level of abstraction in the description of the numerics in a concise mathematical format allows for easy alteration and experimentation in the details of the chosen discretisation without having to worry about implementing this particular combination of choices in an efficient way, as the entire process is automated.

As part of the G-ADOPT project, and in collaboration with a team at the Australian National University lead by Rhodri Davies, we are developing a new geodynamical framework implemented in Firedrake. In Davies et al. (2022), we demonstrated its flexibility through a series of geodynamical benchmarks of increasing complexity ranging from relative simple incompressible problems in Cartesian domains to highly-nonlinear, compressible Stokes flow in spherical shell domains, showing good parallel scaling up to 12288 compute cores.

A number of people in the Firedrake community have been involved in some recent advances

in preconditioning techniques to efficiently solve the Stokes equations (Farrell et al., 2019; Shih et al., 2022) with the associated discretisations and preconditioner implementations directly available in Firedrake. I therefore believe that Firedrake would be the ideal environment to compare these approaches with the approach in Fluidity based on Taylor-Hood elements and a AMG-preconditioned Schur complement approach. To facilitate a more balanced comparison between anisotropic adaptive mesh approaches as advocated in this thesis with the optimal configuration of a uniform resolution mantle convection model, the same anisotropic mesh adaptivity technology would need to be made available in Firedrake. Recently I have been working with Joe Wallwork, Nicholas Barral, and Matt Knepley towards this end. For comparisons between the various free surface approaches, the approach of eliminating the additional free surface variables introduced by our scheme, as introduced in section 2.6.2, will simplify the implementation of this method in Firedrake.

Next to the flexibility in changing the discretisation, the physical equations that are being solved, and solver strategies, the main motivation for the G-ADOPT project is the model's ability to efficiently compute sensitivities, gradients of model outcomes with respect to arbitrary input parameters, through an automatically derived adjoint - which again is flexible under changes made to the equations and discretisation. This ability further enables powerful strategies to use the model in an inversion context.

As mentioned in the introduction, observations of the mantle flow structure are relatively sparse and difficult to obtain, motivating the use of numerical models to better understand the fundamental processes involved. A recent surge in observational data sets however has provided increasing constraints on the dynamics and evolution of mantle flow. Numerical models of the temporal evolution of this flow fundamentally rely on initial conditions and boundary conditions, in addition to a good understanding of the properties of the materials involved. Observational data sets however, such as those obtained from seismic inversion, are either only available for the present day structure, or, even where historical reconstructions are possible, typically more focused on the near-surface. This naturally leads to the formulation of an inversion problem in which unknown inputs to the forward model, such as initial or boundary conditions, or rheological properties, are improved, or potentially completely reconstructed, by

the constraints imposed trying to match the outputs of the model with the available data. A key ingredient to efficiently solve such inversion problems is the availability of gradient information through the adjoint. The availability of an automated, efficient adjoint in the Firedrake based G-ADOPT models including complex nonlinear extensions, will therefore open up unprecedented capabilities to integrate these data sets and improve our models of the mantle convection process.

Bibliography

Alnes, M. S., A. Logg, K. B. Olgaard, M. E. Rognes, and G. N. Wells (2014). "Unified Form Language: A domain-specific language for weak formulations of partial differential equations." In: *ACM Transactions on Mathematical Software* 40, pp. 2–9.

Andrés-Martínez, Miguel, Jason P. Morgan, Marta Pérez-Gussinyé, and Lars Rüpke (2015). "A new free-surface stabilization algorithm for geodynamical modelling: Theory and numerical tests". In: *Physics of the Earth and Planetary Interiors* 246, pp. 41–51. ISSN: 0031-9201. DOI: 10.1016/j.pepi.2015.07.003.

Aristodemou, Elsa, Luz Maria Boganegra, Laetitia Mottet, Dimitrios Pavlidis, Achilleas Constantinou, Christopher Pain, Alan Robins, and Helen ApSimon (2018). "How tall buildings affect turbulent air flows and dispersion of pollution within a neighbourhood". In: *Environmental Pollution* 233, pp. 782–796. ISSN: 0269-7491. DOI: 10.1016/j.envpol.2017.10.041.

Backus, George (1986). "Poloidal and toroidal fields in geomagnetic field modeling". In: *Reviews of Geophysics* 24.1, pp. 75–109.

Balay, Satish, Shrirang Abhyankar, Mark F. Adams, Steven Benson, Jed Brown, Peter Brune, Kris Buschelman, Emil Constantinescu, Lisandro Dalcin, Alp Dener, Victor Eijkhout, Jacob Faibussowitsch, William D. Gropp, Václav Hapla, Tobin Isaac, Pierre Jolivet, Dmitry Karpeev, Dinesh Kaushik, Matthew G. Knepley, Fande Kong, Scott Kruger, Dave A. May, Lois Curfman McInnes, Richard Tran Mills, Lawrence Mitchell, Todd Munson, Jose E. Roman, Karl Rupp, Patrick Sanan, Jason Sarich, Barry F. Smith, Stefano Zampini, Hong Zhang, Hong Zhang, and Junchao Zhang (2022). *PETSc/TAO Users Manual*. Tech. rep. ANL-21/39 - Revision 3.18. Argonne National Laboratory.

Balay, Satish, William D. Gropp, Lois Curfman McInnes, and Barry F. Smith (1997). "Efficient management of parallelism in object-oriented numerical software libraries". In: *Modern software tools for scientific computing*. Birkhauser Boston Inc., pp. 163–202. ISBN: 0-8176-3974-8.

Baumgardner, J. R. (1985). "Three-dimensional treatment of convective flow in the Earth's mantle". In: *J. Stat. Phys.* 39, pp. 501–511. DOI: 10.1007/BF01008348.

Beaufort, Pierre-Alexandre, Christophe Geuzaine, and Jean-François Remacle (2020). "Automatic surface mesh generation for discrete models - A complete and automatic pipeline based on reparametrization". In: *Journal of Computational Physics* 417, p. 109575. ISSN: 0021-9991. DOI: 10.1016/j.jcp.2020.109575.

Beaumont, C., R. A. Jamieson, M. H. Nguyen, and B. Lee (2001). "Himalayan tectonics explained by extrusion of a low-viscosity crustal channel coupled to focused surface denudation". In: *Nature* 414, pp. 738–742. DOI: 10.1038/414738a.

Beaumont, C., P. Kamp, J. Hamilton, and P. Fullsack (1996). "The continental collision zone, South Island, New Zealand: comparison of geodynamical models and observations." In: *J. Geophys. Res.* 101, pp. 3333–3359.

Bernardi, Christine (1989). "Optimal finite-element interpolation on curved domains". In: *SIAM Journal on Numerical Analysis* 26.5, pp. 1212–1240.

Blankenbach, B., F. Busse, U. Christensen, L. Cserepes, D. Gunkel, U. Hansen, H. Harder, G. Jarvis, M. Koch, G. Marquart, D. Moore, P. Olson, H. Schmeling, and T. Schnaubelt (1989). "A benchmark comparison for mantle convection codes". In: *Geophys. J. Int.* 98, pp. 23–38. DOI: 10.1111/j.1365-246X.1989.tb05511.x.

Blinova, Irina, Ilya Makeev, and Igor Popov (2016). "Benchmark solutions for stokes flows in cylindrical and spherical geometry". In: *Bulletin of the Transilvania University of Brasov. Mathematics, Informatics, Physics. Series III* 9.1, p. 11.

Boffi, D., F. Brezzi, and M. Fortin (2013). "Incompressible Materials and Flow Problems". In: *Mixed Finite Element Methods and Applications*. Springer Series in Computational Mathematics. Springer. Chap. 8, pp. 459–538.

Boman, E. G., U. V. Catalyurek, C. Chevalier, and K. D. Devine (2012). "The Zoltan and Isorropia Parallel Toolkits for Combinatorial Scientific Computing: Partitioning, Ordering, and Coloring". In: *Scientific Programming* 20.2, pp. 129–150.

Braun, J. (2006). "Recent advances and current problems in modelling surface processes and their interactions with tectonics and crustal deformation. *In*: Buiter, S. J. H., and Schreurs G. (Eds.), Analog and Numerical modelling of crustal-scale processes." In: *Spec. Pub. Geol. Soc. London*, pp. 307–325.

Braun, J. (2010). "The many surface expressions of mantle dynamics". In: *Nature Geoscience* 3, pp. 826–833. DOI: 10.1038/ngeo1020.

Buchan, A. G., C. C. Pain, F. Fang, and I. M. Navon (2013). "A POD reduced-order model for eigenvalue problems with application to reactor physics". In: *International Journal for Numerical Methods in Engineering* 95.12, pp. 1011–1032.

Buffa, Annalisa, Carlo De Falco, and G. Sangalli (2011). "Isogeometric analysis: stable elements for the 2D Stokes equation". In: *International Journal for Numerical Methods in Fluids* 65.11-12, pp. 1407–1422.

Bunge, H.-P., M. A. Richards, and J. R. Baumgardner (2002). "Mantle circulation models with sequential data-assimilation: inferring present-day mantle structure from plate motion histories". In: *Phil. Trans. R. Soc. London, Set. A* 360, pp. 2545–2567. DOI: 10.1098/rsta.2002.1080..

Burstedde, C., O. Ghattas, M. Gurnis, G. Stadler, E. Tan, T. Tu, L. C. Wilcox, and S. Zhong (2008). "Scalable adaptive mantle convection simulation on petascale supercomputers". In: *Proceedings of the 2008 ACM/IEEE conference on Supercomputing*. IEEE Press, pp. 1–15. ISBN: 978-1-4244-2835-9.

Burstedde, C., G. Stadler, L. Alisic, L. C. Wilcox, E. Tan, M. Gurnis, and O. Ghattas (2013). "Large-scale adaptive mantle convection simulation". In: *Geophys. J. Int.* 192, pp. 889–906. DOI: 10.1093/gji/ggs070.

Busse, F. H., U. Christensen, R. Clever, L. Cserepes, C. Gable, E. Giannandrea, L. Guillou, G. Houseman, H. C. Nataf, M. Ogawa, M. Parmentier, C. Sotin, and B. Travis (1994). "3D convection at infinite Prandtl number in Cartesian geometry - a benchmark compar-

ison". In: *Geophys. Astrophys. Fluid Dyn.* 75, pp. 39–59. ISSN: 0309-1929. DOI: 10.1080/03091929408203646.

Ceze, Marco and Krzysztof J. Fidkowski (2013). "Anisotropic hp-adaptation framework for functional prediction". In: *AIAA journal* 51.2, pp. 492–509.

Chen, Fangqin, D. Rhodri Davies, Saskia Goes, Lior Suchoy, and Stephan C. Kramer (2022a). "Comparing the Dynamics of Free Subduction in Cartesian and Spherical Domains". In: *Geochemistry, Geophysics, Geosystems* 23 (12), e2022GC010757. DOI: 10.1029/2022GC010757.

Chen, Fangqin, D. Rhodri Davies, Saskia Goes, Lior Suchoy, and Stephan C. Kramer (2022b). "How slab age and width combine to dictate the dynamics and evolution of subduction systems: A 3-D spherical study". In: *Geochemistry, Geophysics, Geosystems* 23 (11), e2022GC010597. DOI: 10.1029/2022GC010597.

Chen, Long, Pengtao Sun, and Jinchao Xu (2007). "Optimal anisotropic meshes for minimizing interpolation errors in L^p-norm". In: *Mathematics of Computation* 76.257, pp. 179–204.

Choblet, G., O. Cadek, F. Couturier, and C. Dumoulin (2007). "OEDIPUS: a new tool to study the dynamics of planetary interiors". In: *Geophys. J. Int.* 170, pp. 9–30. DOI: 10.1111/j.1365-246X.2007.03419.x.

Crameri, F., H. Schmeling, G. J. Golabek, T. Duretz, R. Orendt, S. J. H. Buiter, D. A. May, B. J. P. Kaus, T. V. Gerya, and P. J. Tackley (2012). "A comparison of numerical surface topography calculations in geodynamic modelling: an evaluation of the 'sticky air' method". In: *Geophysical Journal International* 189.1, pp. 38–54.

Davies, D. R. and J. H. Davies (2009). "Thermally–driven mantle plumes reconcile multiple hotspot observations". In: *Earth Planet. Sci. Lett.* 278, pp. 50–54. DOI: 10.1016/j.epsl.2008.11.027.

Davies, D. R., J. H. Davies, P. C. Bollada, O. Hassan, K. Morgan, and P. Nithiarasu (2013). "A hierarchical mesh refinement technique for global 3D spherical mantle convection modelling". In: *Geosci. Mod. Dev.* 6, pp. 1095–1107. DOI: 10.5194/gmd-6-1095-2013.

Davies, D. R., J. H. Davies, O. Hassan, K. Morgan, and P. Nithiarasu (2008). "Adaptive finite element methods in geodynamics: convection dominated mid-ocean ridge and subduction

zone simulations". In: *International Journal of Numerical Methods for Heat & Fluid Flow* 18, pp. 1015–1035. DOI: 10.1108/09615530810899079.

Davies, D. R., S. C. Kramer, S. Ghelichkhan, and A. Gibson (2022). "towards automatic finite-element methods for geodynamics via Firedrake". In: *Geoscientific Model Development* 15.13, pp. 5127–5166. DOI: 10.5194/gmd-15-5127-2022.

Davies, D. R., G. Le Voci, S. Goes, S. C. Kramer, and C. R. Wilson (2015). "The mantle wedge's transient 3-D flow regime and thermal structure". In: *Geochem. Geophys. Geosys.* 17, pp. 78–100. DOI: 10.1002/2015GC006125.

Davies, D. R., A. P. Valentine, S. C. Kramer, N. Rawlinson, M. J. Hoggard, C. Eakin, and C. Wilson (2019). "Earth's multi-scale topographic response to global mantle flow". In: *Nature Geo.* 12, pp. 845–850. DOI: 10.1038/s41561-019-0441-4.

Davies, D. R., C. R. Wilson, and S. C. Kramer (2011). "Fluidity: a fully unstructured anisotropic adaptive mesh computational modeling framework for geodynamics". In: *Geochem. Geophys. Geosys.* 120, Q06001. DOI: 10.1029/2011GC003551.

Davies, Geoffrey F. (2001). *Dynamic Earth: plates, plumes and mantle convection*. American Association of Physics Teachers.

Duretz, Thibault, David Alexander May, T. V. Gerya, and P. J. Tackley (2011). "Discretization errors and free surface stabilization in the finite difference and marker-in-cell method for applied geodynamics: A numerical study". In: *Geochemistry, Geophysics, Geosystems* 12.7.

Duvernay, Thomas, D. Rhodri Davies, Christopher R. Mathews, Angus H. Gibson, and Stephan C. Kramer (2021). "Linking intraplate volcanism to lithospheric structure and asthenospheric flow". In: *Geochemistry, Geophysics, Geosystems* 22.8, e2021GC009953. DOI: 10.1029/2021GC009953.

Duvernay, Thomas, D. Rhodri Davies, Christopher R. Mathews, Angus H. Gibson, and Stephan C. Kramer (2022). "Continental Magmatism: The Surface Manifestation of Dynamic Interactions Between Cratonic Lithosphere, Mantle Plumes and Edge-Driven Convection". In: *Geochemistry, Geophysics, Geosystems* 23.7, e2022GC010363. DOI: 10.1029/2022GC010363.

Ern, A. and J.-L. Guermond (2004). *Theory and Practice of Finite Elements*. Princeton: Springer.

Farrell, Patrick E., Lawrence Mitchell, and Florian Wechsung (2019). "An augmented Lagrangian preconditioner for the 3D stationary incompressible Navier–Stokes equations at high Reynolds number". In: *SIAM Journal on Scientific Computing* 41.5, A3073–A3096.

Farrell, Patrick E., Matthew D. Piggott, Christopher C. Pain, Gerard J. Gorman, and Cian R. Wilson (2009). "Conservative interpolation between unstructured meshes via supermesh construction". In: *Computer methods in applied mechanics and engineering* 198.33-36, pp. 2632–2642.

Farrell, PE, MD Piggott, GJ Gorman, DA Ham, CR Wilson, and TM Bond (2011). "Automated continuous verification for numerical simulation". In: *Geoscientific Model Development* 4.2, pp. 435–449.

Flament, Nicolas, Michael Gurnis, and R. Dietmar Müller (Apr. 2013). "A review of observations and models of dynamic topography". In: *Lithosphere* 5.2, pp. 189–210. ISSN: 1941-8264. DOI: 10.1130/L245.1.

Frey, Pascal-Jean and Frédéric Alauzet (2005). "Anisotropic mesh adaptation for CFD computations". In: *Computer methods in applied mechanics and engineering* 194.48-49, pp. 5068–5082.

Fuchs, L., H. Schmeling, and H. Koyi (2011). "Numerical models of salt diapir formation by down-building: the role of sedimentation rate, viscosity contrast, initial amplitude and wavelength". In: *Geophys. J. Int.* 186, pp. 390–400. DOI: 10.1111/j.1365-246X.2011.05058.x.

Fullsack, P. (1995). "An arbitrary Lagrangian-Eulerian formulation for creeping flows and its application in tectonic models". In: *Geophys. J. Int.* 120, pp. 1–23.

Furuichi, Mikito and Dave A. May (2015). "Implicit solution of the material transport in Stokes flow simulation: Toward thermal convection simulation surrounded by free surface". In: *Computer Physics Communications* 192, pp. 1–11. ISSN: 0010-4655. DOI: 10.1016/j.cpc.2015.02.011.

Garel, Fanny, Saskia Goes, D. Rhodri Davies, J. Huw Davies, Stephan C. Kramer, and Cian R. Wilson (2014). "Interaction of subducted slabs with the mantle transition-zone: A regime diagram from 2-D thermo-mechanical models with a mobile trench and an overriding plate". In: *Geochemistry, Geophysics, Geosystems* 15. DOI: 10.1002/2014GC005257.

Girault, Vivette and Pierre-Arnaud Raviart (2012). *Finite element methods for Navier-Stokes equations: theory and algorithms*. Vol. 5. Springer Science & Business Media.

Gurnis, M., C. Eloy, and S. Zhong (1996). "Free-surface formulation of mantle convection: II. Implication for subduction-zone observables." In: *Geophys. J. Int* 127, pp. 719–727.

Guttman, Antonin (1984). "R-trees: A dynamic index structure for spatial searching". In: *Proceedings of the 1984 ACM SIGMOD international conference on Management of data*, pp. 47–57.

Hager, B. H., R. W. Clayton, M. A. Richards, R. P. Comer, and A. M. Dziewonski (1985). "Lower mantle heterogeneity, dynamic topography and the geoid". In: *Nature* 313, pp. 541–545. DOI: 10.1038/313541a0.

Hager, B. H. and A. M. Richards (1989). "Long–wavelength variations in Earth's geoid: Physical models and dynamical implications". In: *Phil. Trans. Roy. Soc. London, Ser. A.* 328, pp. 309–327.

Ham, D. A., P. E. Farrell, G. J. Gorman, J. R Maddison, C. R. Wilson, S. C. Kramer, J. Shipton, G. S. Collins, C. J. Cotter, and M. D. Piggott (2009). "Spud 1.0: generalising and automating the user interfaces of scientific computer models". In: *Geoscientific Model Development* 2.1, pp. 33–42.

Harlow, F. H. and J. E. Welch (1965). "Numerical calculation of time-dependent viscous incompressible flow of fluid with free surface". In: *Phys. Fluids* 8, pp. 2182–2189.

Heister, T., J. Dannberg, R. Gassmoller, and W. Bangerth (2017). "High accuracy mantle convection simulation through modern numerical methods: II: realistic models and problems". In: *Geophys. J. Int.* 210, pp. 833–851. DOI: 10.1093/gji/ggx195.

Hoang, Tuong, Clemens V. Verhoosel, Ferdinando Auricchio, E. Harald van Brummelen, and Alessandro Reali (2017). "Mixed isogeometric finite cell methods for the stokes problem". In: *Computer Methods in Applied Mechanics and Engineering* 316, pp. 400–423.

Horbach, André, Marcus Mohr, and Hans-Peter Bunge (2020). "A semi-analytic accuracy benchmark for Stokes flow in 3-D spherical mantle convection codes". In: *GEM-International Journal on Geomathematics* 11.1, pp. 1–35.

Iaffaldano, G., H.-P. Bunge, and T. Dixon (2006). "Feedback between mountain belt growth and plate convergence". In: *Geology* 34, pp. 893–896. DOI: 10.1130/G22661.1.

Iaffaldano, G., L. Husson, and H.-P. Bunge (2011). "Monsoon speeds up Indian plate motion". In: *Earth Planet. Sci. Lett.* 304, pp. 503–510. DOI: 10.1016/j.epsl.2011.02.026.

Jackson, M. D., J. R. Percival, P. Mostaghimi, B. S. Tollit, D. Pavlidis, C. C. C. Pain, J. L. M. A. Gomes, A. H. El-Sheikh, P.. Salinas, A. H. Muggeridge, and M. J. Blunt (May 2015). "Reservoir Modeling for Flow Simulation by Use of Surfaces, Adaptive Unstructured Meshes, and an Overlapping-Control-Volume Finite-Element Method". In: *SPE Reservoir Evaluation & Engineering* 18.02, pp. 115–132. ISSN: 1094-6470. DOI: 10.2118/163633-PA.

Jimack, P. K. and A. J. Wathen (1991). "Temporal derivatives in the finite-element method on continuously deforming grids". In: *SIAM J. Numer. Anal.* 28, pp. 990–1003. DOI: 10.1137/0728052.

Jones, T. D., D. R. Davies, I. H. Campbell, G. Iaffaldano, G. Yaxley, S. C. Kramer, and C. R. Wilson (2017). "The concurrent emergence and causes of double volcanic hotspot tracks on the Pacific plate". In: *Nature* 545, pp. 472–476. DOI: 10.1038/nature22054.

Jones, T. D., D. R. Davies, I. H. Campbell, C. R. Wilson, and S. C. Kramer (2016). "Do mantle plumes preserve the heterogeneous structure of their deep-mantle source?" In: *Earth Planet. Sci. Lett.* 434, pp. 10–17. DOI: 10.1016/j.epsl.2015.11.016.

Kaus, B. J. P., H. Muhlhaus, and D. A. May (2010). "A stabilization algorithm for geodynamic numerical simulations with a free surface". In: *Phys. Earth Planet. Int.* 181, pp. 12–20. DOI: 10.1016/j.pepi.2010.04.007.

Kaus, B. J. P., C. Steedman, and T. W. Becker (2008). "From passive continental margin to mountain belt: insights from analytical and numerical models and application to Taiwan". In: *Phys. Earth Planet. Int.* 171, pp. 235–251. DOI: 10.1016/j.pepi.2008.06.015.

King, S. D., C. Lee, P. E. van Keken, W. Leng, S. Zhong, E. Tan, N. Tosi, and M. C. Kameyama (2009). "A community benchmark for 2-D Cartesian compressible convection in Earth's mantle". In: *Geophys. J. Int.* 179, pp. 1–11.

Koons, P. (1990). "Two-sided orogen: collision and erosion from the sandbox to the Southern Alps, New Zealand". In: *Geology* 18, pp. 679–682.

Kramer, S. C., D. R. Davies, and C. R. Wilson (2021). "Analytical solutions for mantle flow in cylindrical and spherical shells". In: *Geoscientific Model Development* 14.4, pp. 1899–1919. DOI: 10.5194/gmd-14-1899-2021.

Kramer, S. C., C. R. Wilson, and D. R. Davies (2012). "An implicit free-surface algorithm for geodynamical simulations". In: *Phys. Earth Planet. Int.* 194, pp. 25–37. DOI: 10.1016/j.pepi.2012.01.001.

Kramer, Stephan C. (2020). *Assess (v1.0), Analytical Solutions for the Stokes Equations in Spherical Shells in python.* DOI: 10.5281/zenodo.3891545.

Kronbichler, M., T. Heister, and W. Bangerth (2012). "High accuracy mantle convection simulation through modern numerical methods". In: *Geophys. J. Int.* 191, pp. 12–29. DOI: 10.1111/j.1365-246X.2012.05609.x.

Lavier, L. L., W. Buck, and A. Poliakov (2000). "Factors controlling normal fault offset in an ideal brittle layer". In: *J. Geophys. Res.* 105, pp. 23431–23442.

Le Voci, G., D. R. Davies, S. Goes, S. C. Kramer, and C. R. Wilson (2014). "A systematic 2-D investigation into the mantle wedge's transient flow regime and thermal structure: complexities arising from a hydrated rheology and thermal buoyancy". In: *Geochem. Geophys. Geosys.* 15, pp. 28–51. DOI: 10.1002/2013GC005022.

Lee, Cin-Ty A., Peter Luffi, Terry Plank, Heather Dalton, and William P. Leeman (2009). "Constraints on the depths and temperatures of basaltic magma generation on Earth and other terrestrial planets using new thermobarometers for mafic magmas". In: *Earth and Planetary Science Letters* 279.1-2, pp. 20–33.

Leng, W. and S. Zhong (2011). "Implementation and application of adaptive mesh refinement for thermo–chemical mantle convection studies". In: *Geochem. Geophys. Geosys.* 12, Q04006. DOI: 10.1029/2010GC003425.

Leonard, B. P. (June 1991). "The ULTIMATE conservative difference scheme applied to unsteady one-dimensional advection". In: *Computer Methods in Applied Mechanics and Engineering* 88.1, pp. 17–74. DOI: 10.1016/0045-7825(91)90232-U.

Liu, L., S. Spasojevic, and M. Gurnis (2008). "Reconstructing Farallon Plate Subduction Beneath North America Back to the Late Cretaceous". In: *Science* 322, pp. 934–938. DOI: 10.1126/science.1162921.

Liu, Shangxin and Scott D King (2019). "A benchmark study of incompressible Stokes flow in a 3-D spherical shell using ASPECT". In: *Geophysical Journal International* 217.1, pp. 650–667.

Logg, A., K.-A. Mardal, and G. Wells (2012). *Automated Solution of Differential Equations by the Finite Element Method: The FEniCS Book, Lecture Notes in Computational Science and Engineering vol. 84*. Springer, Berlin. DOI: 10.1007/978-3-642-23099-8.

Mathews, Christopher (2021). "Methods for tracking material properties within an unstructured, adaptive mesh computational modelling framework, with application to simulating the development of seismic anisotropy at spreading centres and transform faults". PhD thesis. The Australian National University (Australia).

May, D. and L. Moresi (2008). "Preconditioned iterative methods for Stokes flow problems arising in computational geodynamics". In: *Physics of the Earth and Planetary Interiors* 171, pp. 33–47. DOI: 10.1016/j.pepi.2008.07.036.

May, D. A., L. Le Pourhiet, and J. Brown (2011). *Tightly coupled geodynamic systems: Software, implicit solvers, and application*. Presentation at AGU 2011.

May, D. A., Wouter Pieter Schellart, and L. Moresi (2013). "Overview of adaptive finite element analysis in computational geodynamics". In: *Journal of Geodynamics* 70, pp. 1–20.

McKenzie, D. (1977). "Surface deformation, gravity anomalies and convection". In: *Geophys. J. Int.* 48, pp. 211–238. DOI: 10.1111/j.1365-246X.1977.tb01297.x.

Melosh, H. J. and A. Raefsky (1980). "Dynamical origin of subduction zone topography". In: *Geophys. J. Roy. Astr. Soc.* 60, pp. 333–354.

Meurer, Aaron, Christopher P. Smith, Mateusz Paprocki, Ondřej Čertík, Sergey B. Kirpichev, Matthew Rocklin, AMiT Kumar, Sergiu Ivanov, Jason K. Moore, Sartaj Singh, Thilina Rathnayake, Sean Vig, Brian E. Granger, Richard P. Muller, Francesco Bonazzi, Harsh Gupta, Shivam Vats, Fredrik Johansson, Fabian Pedregosa, Matthew J. Curry, Andy R. Terrel, Štěpán Roučka, Ashutosh Saboo, Isuru Fernando, Sumith Kulal, Robert Cimrman,

and Anthony Scopatz (Jan. 2017). "SymPy: symbolic computing in Python". In: *PeerJ Computer Science* 3, e103. ISSN: 2376-5992. DOI: 10.7717/peerj-cs.103.

Molnar, P. and P. England (1990). "Late Cenozoic uplift of mountain ranges and global climate change: chicken and egg?" In: *Nature* 346, pp. 29–34.

Moresi, L. N. and V. S. Solomatov (1995). "Numerical investigations of 2D convection with extremely large viscosity variations". In: *Phys. Fluid* 7, pp. 2154–2162. DOI: 10.1063/1.868465.

Mostaghimi, Peyman, James R. Percival, Dimitrios Pavlidis, Richard J. Ferrier, Jefferson L. M. A. Gomes, Gerard J. Gorman, Matthew D. Jackson, Stephen J. Neethling, and Christopher C. Pain (2015). "Anisotropic mesh adaptivity and control volume finite element methods for numerical simulation of multiphase flow in porous media". In: *Mathematical Geosciences* 47.4, pp. 417–440.

Muhlhaus, H. (2007). "Free surface modeling based on level sets". In: *ICCEES* 3, pp. 225–232.

Pain, C. C. (2000). "Brief description and capabilities of the General Purpose CFD Code: FLUIDITY". In: *Imperial College of Science, Technology and Medicine, Internal Rep.*

Pain, C. C., M. D. Eaton, R. P. Smedley-Stevenson, A. J. H. Goddard, M. D. Piggott, and C. R. E. de Oliveira (2006). "Streamline upwind Petrov–Galerkin methods for the steady-state Boltzmann transport equation". In: *Computer Methods in Applied Mechanics and Engineering* 195.33, pp. 4448–4472. ISSN: 0045-7825. DOI: 10.1016/j.cma.2005.09.004.

Pain, C. C., S. Mansoorzadeh, and C. R. E. de Oliveira (2001a). "A study of bubbling and slugging fluidised beds using the two-fluid granular temperature model". In: *International Journal of Multiphase Flow* 27.3, pp. 527–551. ISSN: 0301-9322. DOI: 10.1016/S0301-9322(00)00035-5.

Pain, C. C., M. D. Piggott, A. J. H. Goddard, F. Fang, G. J. Gorman, D. P. Marshall, M. D. Eaton, P. W. Power, and C. R. E. De Oliveira (2005). "Three-dimensional unstructured mesh ocean modelling". In: *Ocean Modelling* 10.1-2, pp. 5–33.

Pain, C. C., A. P. Umpleby, C. R. E. de Oliveira, and A. J. H. Goddard (2001b). "Tetrahedral mesh optimisation and adaptivity for steady-state and transient finite element calculations".

In: *Computer Methods in Applied Mechanics and Engineering* 190.29, pp. 3771–3796. ISSN: 0045-7825. DOI: 10.1016/S0045-7825(00)00294-2.

Palache, Charles (1920). "The gnomonic projection". In: *American Mineralogist: Journal of Earth and Planetary Materials* 5.4, pp. 67–80.

Parsons, B. and S. Daly (1983). "The relationship between surface topography, gravity anomalies, and temperature structure of convection". In: *J. Geophys. Res.* 88, pp. 1129–1144. DOI: 10.1029/JB088iB02p01129.

Patočka, Vojtech, Hana Čížková, and P. J. Tackley (2019). "Do elasticity and a free surface affect lithospheric stresses caused by upper-mantle convection?" In: *Geophysical Journal International* 216.3, pp. 1740–1760.

Perrin, Alexander, Saskia Goes, Julie Prytulak, D. Rhodri Davies, Cian Wilson, and Stephan C. Kramer (2016). "Reconciling mantle wedge thermal structure with arc lava thermobarometric determinations in oceanic subduction zones". In: *Geochemistry, Geophysics, Geosystems* 10, pp. 4105–4127. DOI: 10.1002/2016GC006527.

Piggott, Matthew D., Christopher C. Pain, Gerard J. Gorman, David P. Marshall, and Peter D. Killworth (2008). "Unstructured adaptive meshes for ocean modeling". In: *Ocean modeling in an eddying regime* 177, pp. 383–408.

Poore, H. R., N. White, and S. Jones (2009). "A Neogene chronology of Iceland plume activity from V-shaped ridges". In: *Earth Planet. Sci. Lett* 283, pp. 1–13. DOI: 10.1016/j.epsl.2009.02.028.

Popov, I. Yu, Igor S. Lobanov, Sergey I. Popov, Anton I. Popov, and Taras V. Gerya (2014). "Practical analytical solutions for benchmarking of 2-D and 3-D geodynamic Stokes problems with variable viscosity". In: *Solid Earth* 5.1, pp. 461–476.

Ramberg, H. (1967). *Gravity, Deformation and the Earth's Crust: In Theory, Experiments and Geological Application.* Academic Press, London and New York, p. 214.

Rathgeber, F., D. A. Ham, L. Mitchell, M. Lange, F. Luporini, A. T. T. Mcrae, G.-T. Bercea, G. R. Markall, and P. H. J. Kelly (2016). "Firedrake: Automating the Finite Element Method by Composing Abstractions". In: *ACT Trans. Math. Softw.* 43, pp. 1–24. DOI: 10.1145/2998441.

Ribe, N. M. (2009). "Analytical Approaches to Mantle Dynamics". In: *Mantle Dynamics*. Ed. by D. Bercovici and G. Schubert. Vol. 7. Treatise on Geophysics. Elsevier. Chap. 4, pp. 167–226.

Roache, P. J. (2002). "Code Verification by the Method of Manufactured Solutions". In: *Journal of Fluids Engineering* 124.1, pp. 4–10. DOI: 10.1115/1.1436090.

Ronchi, Corrado, Roberto Iacono, and Pier S. Paolucci (1996). "The "cubed sphere": A new method for the solution of partial differential equations in spherical geometry". In: *Journal of computational physics* 124.1, pp. 93–114.

Rose, Ian, Bruce Buffett, and Timo Heister (2017). "Stability and accuracy of free surface time integration in viscous flows". In: *Physics of the Earth and Planetary Interiors* 262, pp. 90–100. DOI: doi.org/10.1016/j.pepi.2016.11.007.

Schmeling, H., A. Y. Babeyko, A. Enns, C. Faccenna, F. Funiciello, T. Gerya, G. J. Golabek, S. Grigulla, B. J. P. Kaus, G. Morra, S. M. Schmalholz, and J. van Hunen (2008). "A benchmark comparison of spontaneous subduction models — Towards a free surface". In: *Phys. Earth Planet. Int.* 171, pp. 198–223. DOI: 10.1016/j.pepi.2008.06.028.

Schubert, G., D. L. Turcotte, and P. Olson (2001). *Mantle convection in the Earth and planets*. Cambridge University Press, p. 940. ISBN: 0521798361.

Shephard, G. E., R. D. Muller, L. Liu, and M. Gurnis (2010). "Miocene drainage reversal of the Amazon River driven by plate–mantle interaction". In: *Nature Geoscience* 3, pp. 870–875. DOI: 10.1038/NGEO1017.

Shih, Yu-hsuan, Georg Stadler, and Florian Wechsung (2022). "Robust multigrid techniques for augmented Lagrangian preconditioning of incompressible Stokes equations with extreme viscosity variations". In: *SIAM Journal on Scientific Computing* 0, S27–S53.

Solomon, S. C., R. P. Comer, and J. W. Head (1982). "The evolution of impact basins — Viscous relaxation of topographic relief". In: *J. Geophys. Res.* 87, pp. 3975–3992. DOI: 10.1029/JB087iB05p03975.

Spasojevic, S., L. Liu, and M. Gurnis (2009). "Adjoint models of mantle convection with seismic, plate motion, and stratigraphic constraints: North America since the Late Cretaceous". In: *Geochem. Geophys. Geosys.* 10, 24 PP. DOI: 10.1029/2008GC002345.

Stadler, G., M. Gurnis, C. Burstedde, L. C. Wilcox, L. Alisic, and O. Ghattas (2010). "The dynamics of plate tectonics and mantle flow: from local to global scales". In: *Science* 329, pp. 1033–1038. DOI: 10.1126/science.1191223.

Styles, E., D. R. Davies, and S. Goes (2011). "Mapping spherical seismic into physical structure: biases from 3-D phase-transition and thermal boundary-layer heterogeneity". In: *Geophys. J. Int.* 184, pp. 1371–1378. DOI: 10.1111/j.1365-246X.2010.04914.x.

Tackley, P. J. (1996). "Effects of strongly variable viscosity on three–dimensional compressible convection in planetary mantles". In: *J. Geophys. Res.* 101, pp. 3311–3332. DOI: 10.1029/95JB03211.

Tackley, P. J. (2008). "Modelling compressible mantle convection with large viscosity contrasts in a three-dimensional spherical shell using the Yin-Yang grid". In: *Phys. Earth Planet. Int.* 171, pp. 7–18. DOI: 10.1016/j.pepi.2008.08.005.

The Sage Developers (2019). *SageMath, the Sage Mathematics Software System (Version 8.6)*. URL: https://www.sagemath.org.

Thieulot, Cedric (2017). "Analytical solution for viscous incompressible Stokes flow in a spherical shell". In: *Solid Earth* 8.6, pp. 1181–1191.

Tosi, N., C. Stein, L. Noack, C. Hüttig, P. Maierová, H. Samuel, D. R. Davies, C. R. Wilson, S. C. Kramer, C. Thieulot, A. Glerum, M. Fraters, W. Spakman, A. Rozel, and P. J. Tackley (2015). "A community benchmark for viscoplastic thermal convection in a 2-D square box". In: *Geochemistry, Geophysics, Geosystems* 16.7, pp. 2175–2196. DOI: 10.1002/2015GC005807.

Tosi, Nicola and Zdeněk Martinec (2007). "Semi-analytical solution for viscous Stokes flow in two eccentrically nested spheres". In: *Geophysical Journal International* 170.3, pp. 1015–1030.

Travis, B. J., C. Anderson, J. R. Baumgardner, C. W. Gable, B. H. Hager, R. J. O'Connell, P. Olson, A. Raefsky, and G. Schubert (1990). "A benchmark comparison of numerical methods for infinite Prandtl number thermal convection in two–dimensional Cartesian geometry". In: *Geophys. Astrophys. Fluid Dyn.* 55, pp. 137–160.

van Keken, P. E., C. Currie, S. D. King, M. D. Behn, A. Cagnioncle, J. He, R. F. Katz, S.-C. Lin, E. M. Parmentier, M. Spiegelman, and K. Wang (2008). "A community benchmark for subduction zone modeling". In: *Phys. Earth Planet. Int.* 171, pp. 187–197. DOI: 10.1016/j.pepi.2008.04.015.

van Keken, P. E., S. D. King, H. Schmeling, U. R. Christensen, D. Neumeister, and M. P. Doin (1997). "A comparison of methods for the modeling of thermo–chemical convection". In: *J. Geophys. Res.* 102, pp. 22477–22495.

Vasilevskii, Yu V. and KN Lipnikov (1999). "An adaptive algorithm for quasioptimal mesh generation". In: *Computational mathematics and mathematical physics* 39.9, pp. 1468–1486.

Willett, S. D. (1999). "Orogeny and orography: the effects of erosion on the structure of mountain belts". In: *J. Geophys. Res.* 104, pp. 28957–28982. DOI: 10.1029/1999JB900248.

Wilson, C. R. (2009). *Modelling multiple-material flows on adaptive unstructured meshes*. PhD Thesis, Imperial College London, UK.

Wilson, Cian (2010). "Modelling multiple-material flows on adaptive unstructured meshes". PhD thesis. Imperial College London.

Wilson, Cian R., Marc Spiegelman, and Peter E. van Keken (2017). "TerraFERMA: The Transparent Finite Element Rapid Model Assembler for multiphysics problems in Earth sciences". In: *Geochemistry, Geophysics, Geosystems* 18.2, pp. 769–810. DOI: 10.1002/2016GC006702.

Wolstencroft, M., J. H. Davies, and D. R. Davies (2009). "Nusselt-Rayleigh number scaling for spherical shell Earth mantle simulation up to a Rayleigh number of 10^9". In: *Phys. Earth Planet. Int.* 176, pp. 132–141. DOI: 10.1016/j.pepi.2009.05.002.

Wright, J. D. and K. G. Miller (1996). "Control of North Atlantic deep water circulation by the Greenland-Scotland Ridge". In: *Paleoceanography* 11, pp. 157–170.

Xiao, D., P. Yang, F. Fang, J. Xiang, C. C. Pain, and I. M. Navon (2016). "Non-intrusive reduced order modelling of fluid–structure interactions". In: *Computer Methods in Applied Mechanics and Engineering* 303, pp. 35–54. ISSN: 0045-7825. DOI: 10.1016/j.cma.2015.12.029.

Yang, Pan, Jiansheng Xiang, Fangxin Fang, Dimitris Pavlidis, John-Paul Latham, and Christopher C. Pain (2016). "Modelling of fluid–structure interaction with multiphase viscous flows using an immersed-body method". In: *Journal of Computational Physics* 321, pp. 571–592.

Yano, Masayuki and David L. Darmofal (2012). "An optimization-based framework for anisotropic simplex mesh adaptation". In: *Journal of Computational Physics* 231.22, pp. 7626–7649.

Zhong, S., M. Gurnis, and G. Hulbert (1993). "Accurate determination of surface normal stress in viscous flow from a consistent boundary flux method". In: *Phys. Earth Planet. Int.* 78, pp. 1–8. DOI: 10.1016/0031-9201(93)90078-N.

Zhong, S., M. Gurnis, and L. Moresi (1996). "Free-surface formulation of mantle convection: I. Basic theory and application to plumes". In: *Geophys. J. Int* 127, pp. 708–718.

Zhong, S., A. McNamara, E. Tan, L. Moresi, and M. Gurnis (2008a). "A benchmark study on mantle convection in a 3-D spherical shell using CitcomS". In: *Geochem. Geophys. Geosys.* 9, Q10017. DOI: 10.1029/2008GC002048.

Zhong, S., M. T. Zuber, L. Moresi, and M. Gurnis (2000). "Role of temperature-dependent viscosity and surface plates in spherical shell models of mantle convection". In: *J. Geophys. Res.* 105, PP. 11, 063–11, 082. DOI: 10.1029/2000JB900003.

Zhong, Shijie, Allen McNamara, Eh Tan, Louis Moresi, and Michael Gurnis (2008b). "A benchmark study on mantle convection in a 3-D spherical shell using CitcomS". In: *Geochemistry Geophysics Geosystems* 9, 32 PP. DOI: 10.1029/2008GC002048.

Zimmerman, Robert W., Azzan Al-Yaarubi, Chris C. Pain, and Carlos A. Grattoni (2004). "Non-linear regimes of fluid flow in rock fractures". In: *International Journal of Rock Mechanics and Mining Sciences* 41. Proceedings of the ISRM SINOROCK 2004 Symposium, pp. 163–169. ISSN: 1365-1609. DOI: 10.1016/j.ijrmms.2004.03.036.

Publications by Stephan Kramer on Geodynamical Modelling

Davies, D. R., C. R. Wilson, and S. C. Kramer (2011). "Fluidity: a fully unstructured anisotropic adaptive mesh computational modeling framework for geodynamics". In: *Geochem. Geophys. Geosys.* 120, Q06001. DOI: 10.1029/2011GC003551.

Kramer, S. C., C. R. Wilson, and D. R. Davies (2012). "An implicit free-surface algorithm for geodynamical simulations". In: *Phys. Earth Planet. Int.* 194, pp. 25–37. DOI: 10.1016/j.pepi.2012.01.001.

Garel, Fanny, Saskia Goes, D. Rhodri Davies, J. Huw Davies, Stephan C. Kramer, and Cian R. Wilson (2014). "Interaction of subducted slabs with the mantle transition-zone: A regime diagram from 2-D thermo-mechanical models with a mobile trench and an overriding plate". In: *Geochemistry, Geophysics, Geosystems* 15. DOI: 10.1002/2014GC005257.

Le Voci, G., D. R. Davies, S. Goes, S. C. Kramer, and C. R. Wilson (2014). "A systematic 2-D investigation into the mantle wedge's transient flow regime and thermal structure: complexities arising from a hydrated rheology and thermal buoyancy". In: *Geochem. Geophys. Geosys.* 15, pp. 28–51. DOI: 10.1002/2013GC005022.

Davies, D. R., G. Le Voci, S. Goes, S. C. Kramer, and C. R. Wilson (2015c). "The mantle wedge's transient 3-D flow regime and thermal structure". In: *Geochem. Geophys. Geosys.* 17, pp. 78–100. DOI: 10.1002/2015GC006125.

Tosi, N., C. Stein, L. Noack, C. Hüttig, P. Maierová, H. Samuel, D. R. Davies, C. R. Wilson, S. C. Kramer, C. Thieulot, A. Glerum, M. Fraters, W. Spakman, A. Rozel, and P. J. Tackley (2015). "A community benchmark for viscoplastic thermal convection in a 2-D

square box". In: *Geochemistry, Geophysics, Geosystems* 16.7, pp. 2175–2196. DOI: 10.1002/2015GC005807.

Jones, T. D., D. R. Davies, I. H. Campbell, C. R. Wilson, and S. C. Kramer (2016). "Do mantle plumes preserve the heterogeneous structure of their deep-mantle source?" In: *Earth Planet. Sci. Lett.* 434, pp. 10–17. DOI: 10.1016/j.epsl.2015.11.016.

Perrin, Alexander, Saskia Goes, Julie Prytulak, D. Rhodri Davies, Cian Wilson, and Stephan C. Kramer (2016). "Reconciling mantle wedge thermal structure with arc lava thermobarometric determinations in oceanic subduction zones". In: *Geochemistry, Geophysics, Geosystems* 10, pp. 4105–4127. DOI: 10.1002/2016GC006527.

Jones, T. D., D. R. Davies, I. H. Campbell, G. Iaffaldano, G. Yaxley, S. C. Kramer, and C. R. Wilson (2017b). "The concurrent emergence and causes of double volcanic hotspot tracks on the Pacific plate". In: *Nature* 545, pp. 472–476. DOI: 10.1038/nature22054.

Davies, D. R., A. P. Valentine, S. C. Kramer, N. Rawlinson, M. J. Hoggard, C. Eakin, and C. Wilson (2019). "Earth's multi-scale topographic response to global mantle flow". In: *Nature Geo.* 12, pp. 845–850. DOI: 10.1038/s41561-019-0441-4.

Duvernay, Thomas, D. Rhodri Davies, Christopher R. Mathews, Angus H. Gibson, and Stephan C. Kramer (2021). "Linking intraplate volcanism to lithospheric structure and asthenospheric flow". In: *Geochemistry, Geophysics, Geosystems* 22.8, e2021GC009953. DOI: 10.1029/2021GC009953.

Kramer, S. C., D. R. Davies, and C. R. Wilson (2021). "Analytical solutions for mantle flow in cylindrical and spherical shells". In: *Geoscientific Model Development* 14.4, pp. 1899–1919. DOI: 10.5194/gmd-14-1899-2021.

Chen, Fangqin, D. Rhodri Davies, Saskia Goes, Lior Suchoy, and Stephan C. Kramer (2022a). "Comparing the Dynamics of Free Subduction in Cartesian and Spherical Domains". In: *Geochemistry, Geophysics, Geosystems* 23 (12), e2022GC010757. DOI: 10.1029/2022GC010757.

Chen, Fangqin, D. Rhodri Davies, Saskia Goes, Lior Suchoy, and Stephan C. Kramer (2022b). "How slab age and width combine to dictate the dynamics and evolution of subduction systems: A 3-D spherical study". In: *Geochemistry, Geophysics, Geosystems* 23 (11), e2022GC010597. DOI: 10.1029/2022GC010597.

Davies, D. R., S. C. Kramer, S. Ghelichkhan, and A. Gibson (2022). "towards automatic finite-element methods for geodynamics via Firedrake". In: *Geoscientific Model Development* 15.13, pp. 5127–5166. DOI: 10.5194/gmd-15-5127-2022.

Duvernay, Thomas, D. Rhodri Davies, Christopher R. Mathews, Angus H. Gibson, and Stephan C. Kramer (2022). "Continental Magmatism: The Surface Manifestation of Dynamic Interactions Between Cratonic Lithosphere, Mantle Plumes and Edge-Driven Convection". In: *Geochemistry, Geophysics, Geosystems* 23.7, e2022GC010363. DOI: 10.1029/2022GC010363.

Other Publications by Stephan Kramer

Ham, David A., Guus S. Stelling Stephan C. Kramer, and Julie Pietrzak (2007). "The symmetry and stability of unstructured mesh C grid shallow water models under the influence of Coriolis". In: *Ocean Modelling* 16, pp. 47–60. DOI: 10.1016/j.ocemod.2006.05.008.

Kramer, Stephan C. and Guus S. Stelling (2008). "A conservative unstructured scheme for rapidly varied flows". In: *International Journal for Numerical Methods in Fluids* 58, pp. 183–212. DOI: 10.1002/fld.1722.

Ham, D. A., P. E. Farrell, G. J. Gorman, J. R Maddison, C. R. Wilson, S. C. Kramer, J. Shipton, G. S. Collins, C. J. Cotter, and M. D. Piggott (2009). "Spud 1.0: generalising and automating the user interfaces of scientific computer models". In: *Geoscientific Model Development* 2.1, pp. 33–42.

Kramer, S. C., C. J. Cotter, and C. C. Pain (2010). "Solving the Poisson equation on small aspect ratio domains using unstructured meshes". In: *Ocean Mod.* 35, pp. 253–263. DOI: 10.1016/j.ocemod.2010.08.001.

Brito-Parada, Pablo R., Stephan C. Kramer, Cian R. Wilson, Chris C. Pain, Steven J. Neethling, and Jan J. Cilliers (2011). "A finite element formulation to model the flow of flotation foams". In: *Chemical Engineering Science* 69, pp. 279–286. DOI: 10.1016/j.ces.2011.10.047.

Funke, Simon W., Chris C. Pain, Stephan C. Kramer, and Matthew D. Piggott (2011). "A wetting and drying algorithm with a combined pressure/free-surface formulation for non-hydrostatic models". In: *Advances in Water Resources* 34, pp. 1483–1495. DOI: 10.1016/j.advwatres.2011.08.007.

Jacobs, Christian T., Gareth S. Collins G. S., Matthew D. Piggott, Stephan C. Kramer, and Cian R. G. Wilson (2013). "Multiphase flow modelling of volcanic ash particle settling in water using adaptive unstructured meshes". In: *Geophysical Journal International* 192, pp. 647–665. DOI: 10.1093/gji/ggs059.

Oishi, Yusuke, Matthew D. Piggott, Takuto Maeda, Stephan C. Kramer, Gareth S. Collins, Hiroaki Tsushima, and Takashi Furumura (2013). "Three-dimensional tsunami propagation simulations using an unstructured mesh finite element model". In: *Journal of Geophysical Research: Solid Earth* 118, pp. 2998–3018. DOI: 10.1002/jgrb.50225.

Hill, Jon, Gareth S. Collins, Alexandros Avdis, Stephan C. Kramer, and Matthew D. Piggott (2014). "How does multiscale modelling and inclusion of realistic palaeobathymetry affect numerical simulation of the Storegga Slide tsunami?" In: *Ocean Modelling* 83, pp. 11–25. DOI: 10.1016/j.ocemod.2014.08.007.

Jacobs, Christian T., Tamara J. Goldin, Gareth S. Collins, Matthew D. Piggott, Stephan C. Kramer, H. Jay Melosh, Cian R. G. Wilson, and Peter A. Allison (2015). "An improved quantitative measure of the tendency for volcanic ash plumes to form in water: implications for the deposition of marine ash beds". In: *Journal of Volcanology and Geothermal Research* 290, pp. 114–224. DOI: 10.1016/j.jvolgeores.2014.10.015.

Martin-Short, Robert, Jon Hill, Stephan C. Kramer, Alexandros Avdis, and Matthew D. Piggott (2015). "Tidal resource extraction in the Pentland Firth, UK: potential impacts on flow regime and sediment transport in the Inner Sound of Stroma". In: *Renewable Energy* 76, pp. 596–607. DOI: 10.1016/j.renene.2014.11.079.

Culley, David M., Simon W. Funke, Stephan C. Kramer, and Matthew D. Piggott (2016). "Integration of cost modelling within the micro-siting design optimisation of tidal turbine arrays". In: *Renewable Energy* 85, pp. 215–227. DOI: 10.1016/j.renene.2015.06.013.

Funke, Simon W., Stephan C. Kramer, and Matthew D. Piggott (2016). "Design optimisation and resource assessment for tidal-stream renewable energy farms using a new continuous turbine approach". In: *Renewable Energy* 99, pp. 1046–1061. DOI: 10.1016/j.renene.2016.07.039.

Kramer, Stephan C. and Matthew D. Piggott (2016). "A correction to the enhanced bottom drag parameterisation of tidal turbines". In: *Renewable Energy* 92, pp. 385–396. DOI: 10.1016/j.renene.2016.02.022.

Smith, Rebecca C., Jon Hill, Gareth S. Collins, Matthew D. Piggott, Stephan C. Kramer, Samuel D. Parkinson, and Cian R. Wilson (2016). "Comparing approaches for numerical modelling of tsunami generation by deformable submarine slides". In: *Ocean Modelling* 100, pp. 125–140. DOI: 10.1016/j.ocemod.2016.02.007.

Viré, Axelle, Johannes Spinneken, Matthew D. Piggott, Chris C. Pain, and Stephan C. Kramer (2016). "Application of the immersed-body method to simulate wave-structure interactions". In: *European Journal of Mechanics-B/Fluids* 55, pp. 330–339. DOI: 10.1016/j.euromechflu.2015.10.001.

Culley, David M., Simon W. Funke, Stephan C. Kramer, and Matthew D. Piggott (2017). "A surrogate-model assisted approach for optimising the size of tidal turbine arrays". In: *International Journal of Marine Energy* 19, pp. 357–373. DOI: 10.1016/j.ijome.2017.05.001.

du Feu, Roan J., Simon W. Funke, Stephan C. Kramer, David M. Culley, Jon Hill, Benjamin S. Halpern, and Matthew D. Piggott (2017). "The trade-off between tidal-turbine array yield and impact on flow: A multi-objective optimisation problem". In: *Renewable Energy* 114, pp. 1247–1257. DOI: 10.1016/j.renene.2017.07.081.

Angeloudis, Athanasios, Stephan C. Kramer, Alexandros Avdis, and Matthew D. Piggott (2018). "Optimising tidal range power plant operation". In: *Applied Energy* 212, pp. 680–690. DOI: 10.1016/j.apenergy.2017.12.052.

Avdis, Alexandros, Adam S. Candy, Jon Hill, Stephan C. Kramer, and Matthew D. Piggott (2018). "Efficient unstructured mesh generation for marine renewable energy applications". In: *Renewable Energy* 116, pp. 842–856. DOI: 10.1016/j.renene.2017.09.058.

Kärnä, Tuomas, Stephan C. Kramer, Lawrence Mitchell, David A. Ham, Matthew D. Piggott, and António Baptista (2018). "Thetis coastal ocean model: discontinuous Galerkin discretization for the three-dimensional hydrostatic equations". In: *Geoscientific Model Development* 11, pp. 4359–4382. DOI: 10.5194/gmd-11-4359-2018.

du Feu, R. J., S. W. Funke, S. C. Kramer, J. Hill, and M. D. Piggott (2019). "The trade-off between tidal-turbine array yield and environmental impact: A habitat suitability modelling approach". In: *Renewable Energy* 143, pp. 390–403. ISSN: 0960-1481. DOI: 10.1016/j.renene.2019.04.141.

Pan, Wei, Stephan C. Kramer, and Matthew D. Piggott (2019). "Multi-layer non-hydrostatic free surface modelling using the discontinuous Galerkin method". In: *Ocean Modelling* 134, pp. 68–83. DOI: 10.1016/j.ocemod.2019.01.003.

Vouriot, Carolanne V. M., Athanasios Angeloudis, Stephan C. Kramer, and Matthew D. Piggot (2019). "Fate of large-scale vortices in idealized tidal lagoons". In: *Environmental Fluid Mechanics* 19.2, pp. 329–348. DOI: 10.1007/s10652-018-9626-4.

Angeloudis, Athanasios, Stephan C. Kramer, Noah Hawkins, and Matthew D. Piggott (2020). "On the potential of linked-basin tidal power plants: An operational and coastal modelling assessment". In: *Renewable Energy* 155, pp. 876–888. DOI: 10.1016/j.renene.2020.03.167.

Pan, Wei, Stephan C. Kramer, Tuomas Kärnä, and Matthew D. Piggott (2020). "Comparing non-hydrostatic extensions to a discontinuous finite element coastal ocean model". In: *Ocean Modelling* 151, p. 101634. DOI: 10.1016/j.ocemod.2020.101634.

Wallwork, Joseph G., Nicolas Barral, Stephan C. Kramer, David A. Ham, and Matthew D. Piggott (2020). "Goal-oriented error estimation and mesh adaptation for shallow water modelling". In: *SN Applied Sciences* 2, pp. 1–11. DOI: 10.1007/s42452-020-2745-9.

Goss, Z. L., D. S. Coles, S. C. Kramer, and M. D. Piggott (2021). "Efficient economic optimisation of large-scale tidal stream arrays". In: *Applied Energy* 295, p. 116975. DOI: 10.1016/j.apenergy.2021.116975.

Mackie, Lucas, Stephan C. Kramer, Matthew D. Piggott, and Athanasios Angeloudis (2021). "Assessing impacts of tidal power lagoons of a consistent design". In: *Ocean Engineering* 240, p. 109879. DOI: 10.1016/j.oceaneng.2021.109879.

Pan, Wei, Stephan C. Kramer, and Matthew D. Piggott (2021). "A σ-coordinate non-hydrostatic discontinuous finite element coastal ocean model". In: *Ocean Modelling* 157, p. 101732. DOI: 10.1016/j.ocemod.2020.101732.

Clare, Mariana C. A., Stephan C. Kramer, Colin J. Cotter, and Matthew D. Piggott (2022a). "Calibration, inversion and sensitivity analysis for hydro-morphodynamic models through the application of adjoint methods". In: *Computers & Geosciences* 163, p. 105104. DOI: 10.1016/j.cageo.2022.105104.

Clare, Mariana C. A., Joseph G. Wallwork, Stephan C. Kramer, Hilary Weller, Colin J. Cotter, and Matthew D. Piggott (2022b). "Multi-scale hydro-morphodynamic modelling using mesh movement methods". In: *GEM-International Journal on Geomathematics* 13.1, pp. 1–39. DOI: 10.1007/s13137-021-00191-1.

Halilovic, Smajil, Fabian Böttcher, Stephan C. Kramer, Matthew D. Piggott, Kai Zosseder, and Thomas Hamacher (2022). "Well layout optimization for groundwater heat pump systems using the adjoint approach". In: *Energy Conversion and Management* 268, p. 116033. DOI: 10.1016/j.enconman.2022.116033.

Pan, Wei, Stephan C. Kramer, Matthew D. Piggott, and Xiping Yu (2022). "Modeling landslide generated waves using the discontinuous finite element method". In: *International Journal for Numerical Methods in Fluids*. DOI: 10.1002/fld.5090.

Piggott, Matthew D., Stephan C. Kramer, Simon W. Funke, David M. Culley, and Athanasios Angeloudis (2022). "Optimization of marine renewable energy systems". In: *Comprehensive Renewable Energy (Second Edition)*. Ed. by Trevor M. Letcher. Second Edition. Elsevier, pp. 176–220. DOI: 10.1016/B978-0-12-819727-1.00179-5.

Zhang, Jisheng, Can Zhang, Athanasios Angeloudis, Stephan C. Kramer, Rui He, and Matthew D. Piggott (2022). "Interactions between tidal stream turbine arrays and their hydrodynamic impact around Zhoushan Island, China". In: *Ocean Engineering* 246, p. 110431. DOI: 10.1016/j.oceaneng.2021.110431.